SANDIA REPORT
SAND2022-13455
Printed September 2022

Sandia National Laboratories

Improving Predictive Capability in REHEDS Simulations with Fast, Accurate, and Consistent Non-Equilibrium Material Properties

S.B. Hansen, A.D. Baczewski, T. Gomez, T.W. Hentschel, C.A. Jennings, A. Kononov, T. Nagayama, K. Adler, A. Cangi, K. Cochrane, B. Robinson, and A. Schleife

Prepared by
Sandia National Laboratories
Albuquerque, New Mexico 87185
Livermore, California 94550

Issued by Sandia National Laboratories, operated for the United States Department of Energy by National Technology & Engineering Solutions of Sandia, LLC.

Available to DOE and DOE contractors from

U.S. Department of Energy
Office of Scientific and Technical Information
P.O. Box 62
Oak Ridge, TN 37831

Telephone: (865) 576-8401
Facsimile: (865) 576-5728
E-Mail: reports@osti.gov
Online ordering: http://www.osti.gov/scitech

Available to the public from

U.S. Department of Commerce
National Technical Information Service
5301 Shawnee Road
Alexandria, VA 22312

Telephone: (800) 553-6847
Facsimile: (703) 605-6900
E-Mail: orders@ntis.gov
Online order: https://classic.ntis.gov/help/order-methods

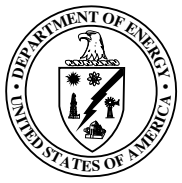

ABSTRACT

Predictive design of REHEDS experiments with radiation-hydrodynamic simulations requires knowledge of material properties (e.g. equations of state (EOS), transport coefficients, and radiation physics). Interpreting experimental results requires accurate models of diagnostic observables (e.g. detailed emission, absorption, and scattering spectra). In conditions of Local Thermodynamic Equilibrium (LTE), these material properties and observables can be pre-computed with relatively high accuracy and subsequently tabulated on simple temperature-density grids for fast look-up by simulations. When radiation and electron temperatures fall out of equilibrium, however, non-LTE effects can profoundly change material properties and diagnostic signatures. Accurately and efficiently incorporating these non-LTE effects has been a longstanding challenge for simulations.

At present, most simulations include non-LTE effects by invoking highly simplified inline models. These inline non-LTE models are both much slower than table look-up and significantly less accurate than the detailed models used to populate LTE tables and diagnose experimental data through post-processing or inversion. Because inline non-LTE models are slow, designers avoid them whenever possible, which leads to known inaccuracies from using tabular LTE. Because inline models are simple, they are inconsistent with tabular data from detailed models, leading to ill-known inaccuracies, and they cannot generate detailed synthetic diagnostics suitable for direct comparisons with experimental data.

This project addresses the challenge of generating and utilizing efficient, accurate, and consistent non-equilibrium material data along three complementary but relatively independent research lines. First, we have developed a relatively fast and accurate non-LTE average-atom model based on density functional theory (DFT) that provides a complete set of EOS, transport, and radiative data, and have rigorously tested it against more sophisticated first-principles multi-atom DFT models, including time-dependent DFT. Next, we have developed a tabular scheme and interpolation methods that compactly capture non-LTE effects for use in simulations and have implemented these tables in the GORGON magneto-hydrodynamic (MHD) code. Finally, we have developed post-processing tools that use detailed tabulated non-LTE data to directly predict experimental observables from simulation output.

ACKNOWLEDGEMENTS

We are grateful for countless hours of useful conversations with our colleagues, many of which preceded this project, including Charles Starrett, Nathaniel Shaffer, Howard Scott, Raymond Clay, Brian Wilson, Carlos Iglesias, Walter Johnson, Kristian Beckwith, James Bailey, Nicki Bennett, Greg Rochau, Roger Vesey, Yechiel Frank, Thomas Mattsson, Didier Saumon, Chandre Dharma-Wardana, Nichelle Bennett, John Carpenter, Andy Porwiztky, Charles Seyler, Michael Desjarlais, Richard More, and many others.

We are grateful for discussions on X-ray diagnostics with Marc-Andre Schaeuble, Jeff Fein, Guillaume Loisel, Ming Wu, Eric Harding, Patrick Knapp, Timothy Webb, Jens Schwarz, and Roger Vesey and on Python programming and Bayesian analysis methods with Patrick Knapp, William Lewis, and Michael Glinsky.

Much of this work builds on foundational developments supported by the U.S. Department of Energy, Office of Science Early Career Research Program, Office of Fusion Energy Sciences under FWP-14-017426.

CONTENTS

LIST OF FIGURES

TERMS AND DEFINITIONS

Abbreviation	Definition
AA	Average atom
CR	Collisional-radiative
DFT	Density functional theory
DoS	Density of states
DSF	Dynamic structure factor
EOS	Equation of state
FAC	Flexible atomic code
HED	High energy density
ICF	Inertial confinement fusion
KG	Kubo-Greenwood
LMD	Lee-More-Desjarlais
LRM	Linear response matrix
LTE	Local thermodynamic equilibrium
MagLIF	Magnetized liner inertial fusion
MC	Multi-configuration
MD	Molecular dynamics
OCP	One-Component Plasma
PIMC	Path-integral Monte Carlo
RDF	Radial distribution function
RES	Radiation effects sciences
[R-] MHD	[Radiation-] Magneto-hydrodynamics
RPA	Random phase approximation
SCRAM	Spectroscopic collisional-radiative atomic model
TDDFT	Time-dependent density functional theory
VASP	Vienna ab-initio simulation package
WDM	Warm dense matter
XC	Exchange-correlation
XRTS	X-ray Thomson Scattering

1. INTRODUCTION

The fields of high energy density science (HEDS), radiation effects science (RES), and inertial confinement fusion (ICF) are characterized by experiments that heat material from everyday, ambient conditions to extremes of pressure, density, and ionization. These experiments are conducted on facilities that compress energy in space and time. For example, Sandia's Z machine stores 20 megajoules of electrical energy in capacitor banks and delivers that energy in the form of > 20 mega-ampere currents to centimeter-scale targets over a few hundred nanoseconds. RES targets such as wire arrays undergo vaporization, implosion, and rapid ionization and heating, producing terawatts of X-rays over a few nanoseconds from stagnation plasmas with temperatures around 3 keV and densities above 1 mg/cm^3. ICF experiments such as Magnetized Liner Inertial Fusion (MagLIF) reach stagnation conditions with similar temperatures and near-solid densities, producing kilojoules of fusion products which, at larger scales, could lead to self-heating fusion plasmas with significant energy gain. HEDS experiments that test the fundamental physics of materials at extreme conditions reach conditions similar to those found in the centers of giant planets, the solar photosphere, and the surfaces of white dwarf stars.

Sophisticated magneto-radiation-hydrodynamic (R-MHD or rad-hydro) simulation codes are used to design and interpret data from these experiments. These codes simulate the evolution of targets under the driving forces of intense radiation or high electrical currents and predict measurable quantities like X-ray and neutron spectra and output yields. Reliable predictions of target evolution and performance enable efficient use of the limited number of experiments that can be conducted on large-scale facilities like Z, shortening design cycles and maximizing impact. Accurate material properties are a key factor in the reliability of rad-hydro codes: changing material equations of state (EOS), transport coefficients, or radiative properties can have profound effects on simulation predictions including implosion velocities, instability development, stagnation conditions, and outputs.

Material properties are incorporated into rad-hydro codes either through read-in of tabular data or by inline calculations. High-accuracy tabular data can be pre-computed using first-principles atomic-scale models such as density functional theory-molecular dynamics (DFT-MD) for EOS and some transport coefficients, or multiconfiguration Dirac-Fock models for radiative properties. Importantly, however, many of the most sophisticated atomic-scale models generate only a subset of material properties. Thus, rad-hydro codes will often use tables of EOS, transport coefficients, and radiative properties that come from independent models. This ensures that the best available data is used for each property, but introduces potential inconsistencies. For example, an EOS table might predict melting at different conditions than a conductivity table. These inconsistencies can lead to instabilities in rad-hydro models and contribute to uncertainty in design predictions. By contrast, inline calculation of material properties ensures a complete set of consistent data, but because these models must be invoked many times, they must be fast and highly simplified, and are thus much less accurate than the sophisticated atomic-scale models used to generate tabular data.

These considerations inspire the first research line of our LDRD, which is to generate a complete and internally consistent set of material property data from a single, relatively accurate model. We choose a DFT-based average-atom model (DFT-AA) as our foundation, since it has deep

theoretical connections to both the DFT-MD models used for EOS and the multiconfiguration Dirac-Fock models used for radiative properties and can generate a complete set of data for a single temperature-density point in ~minutes, rather than the ~hours or days that more sophisticated codes might take. Chapter 2 describes the DFT-AA model and our model choices for its generation of EOS, transport, radiative, and observable properties, as well as its extension to non-equilibrium plasma conditions. These choices were critically informed by detailed comparisons to state-of-the-art DFT-MD, time-dependent density functional theory (TDDFT), collisional-radiative (CR), and line broadening models, whose capabilities were advanced during the LDRD to provide extensive and accurate touchstone reference data to guide the DFT-AA model development. Energy-resolved data such as dynamic structure factors, dynamic collision frequencies, stopping powers, and line shapes have proven especially valuable, since those quantities help us assess collisional properties that have direct impact on transport coefficients, which are particularly ill-constrained in DFT-AA models. We have also begun to investigate many-body calculations of electron-phonon and electron-electron scattering processes, described in Appendix A, that will improve our understanding of transport coefficients.

With a generalized model such as our DFT-AA, data tabulation is straightforward for material in local thermodynamic equilibrium (LTE), where material properties depend only on temperature and density. LTE is a highly restrictive steady-state condition where the electron, ion, and radiation distributions are all perfectly thermal with equal temperatures ($T_e = T_i = T_r$). While LTE is nearly ubiquitous at everyday temperatures, it becomes extremely difficult to maintain at high temperatures, lower densities, and for high-Z elements. Non-LTE effects are especially important for RES targets and diagnostic tracers in ICF experiments, which rely on high-Z radiators like copper (Z = 29) and krypton (Z = 36) to produce multi-keV X-rays from sub-solid-density plasmas with high electron temperatures. In these plasmas, where the radiation temperature cannot keep pace with the electron temperature, LTE calculations overestimate radiative cooling rates by orders of magnitude and predict overionized emission spectra that are dramatically different from experimental measurements. Simplified inline models can roughly capture these dramatic non-LTE effects, but they are much less accurate than more detailed models and are not suitable for direct comparisons with measured data. And even highly simplified inline models add significant computational expense to design simulations, often dominating runtimes.

The importance of non-LTE effects and the relative inaccuracy and computational expense of existing inline models lead to the second research line of our LDRD, which is to design and implement a tabular scheme for non-LTE material properties. This is challenging because non-LTE material properties depend on infinitely variable radiation fields and electron-energy distribution functions and density rather than on equilibrated temperatures and densities. Chapter 3 describes our approach towards tabular non-LTE, which uses a physics-informed tabular structure that captures a wide range of non-equilibrium behavior in tables that are only about ten times larger than LTE tables. For each electron temperature and density, the tables sample radiation fields typical of optically thick, fluorescing, and photoionized plasmas, explicitly including an LTE point. Because many of the details of the radiation are folded into the table generation, we find that we can use a very coarse radiation bin structure that keeps table sizes moderate for use in rad-hydro codes. This chapter also describes interpolation strategies and the implementation of the coarse-binned NLTE tables in the MHD design code GORGON. While the tabular scheme was developed using an existing non-LTE collisional-radiative code that has

reliable radiation physics but rough EOS and transport models, the addition of non-LTE effects to the DFT-AA model described in chapter 2 allows us to combine the research advances in tabular non-LTE and internally consistent modeling for unprecedented accuracy, consistency, and speed in generalized HED target design.

The third and final research line of our LDRD aims to increase the usefulness of these new capabilities by developing post-processors that can predict detailed observables suitable for direct comparison with experiments. Chapter 4 describes our approach. First, we supplement the coarse-binned non-LTE tables described in chapter 3 with separate tables of highly resolved emission and absorption spectra. Next, we have built a simplified plasma model with cylindrical symmetry that reads in plasma conditions and our coarse-group non-LTE tables, performs iterative radiation transport to find a self-consistent radiation field, and produces detailed emission spectra from the tables as output. Finally, we have developed a rigorous model of specific instruments fielded on Z, including diodes, imagers, and spectrometers, that can take detailed multidimensional output from our GORGON MHD simulation and predict spatially, temporally, and spectrally resolved diagnostic data suitable for direct comparison with experimental data.

This LDRD has made significant advances along all three of its research lines, reaching early implementation stages for new capabilities in internally consistent non-LTE DFT-AA models, tabular non-LTE data generation and its use in rad-hydro codes, and post-processing for direct comparisons with experiments. Its support of advances in state-of the art line broadening and TDDFT models has led to tens of presentations at national and international conferences and workshops; four published papers papers directly related to the development work done in the LDRD: Gomez et al. [8, 9, 10], Callow et al. [11] (including two PRLs); two submitted papers: Baczewski et al. [12], Nagayama et al. [13]; three papers near completion: Kononov et al. [14], Hentschel et al. [15], Kononov and Baczewski [16]; and one planned paper: Adler et al. [17]. Additionally, the capabilities developed during the LDRD contributed to eight papers with external collaborators: Kraus et al. [18], Strehlow et al. [19], Hu et al. [20], Beier et al. [21], Jiang et al. [22], Kononov et al. [23], Ramakrishna et al. [24, 25] (including two published PRLs and two submitted Nature Communications articles). The work enabled by this LDRD has led to ongoing dynamic collaborations with students at Cornell and UNM, a late-start Academic Alliance project with UIUC on first-principles modeling of electron-electron interactions (described in Appendix A), and has engaged scientists from LLNL, LANL, and LLE on topics of tabular non-LTE, DFT-AA, and line broadening.

2. INTERNALLY CONSISTENT ATOMIC-SCALE MODELING

Atomic-scale modeling of high energy density plasma (HEDP) is an extraordinarily rich field. Adequate models must incorporate information about both electronic and ionic structure, including physical effects such as partitioning between free and bound electrons (ionization Z^*), the structure and occupations of specific electronic configurations and free-electron densities of states, the spatial distribution of quantum electrons (screening), and the spatial distribution of ions (e.g. lattice structure). Together, these properties can be used to determine the equation of state (EOS) of a material. Some models can also predict the dynamic (energy-dependent) responses of

the whole electron+ion system to perturbations such as external electric fields, temperature gradients, photons, and fast charged particles. These response functions can be used to derive transport properties such as electrical and thermal conductivities, opacities, and stopping powers. The most powerful models can also generate predictions for detailed observables, such as emission, absorption, and scattering spectra.

Within the wide range of temperatures and densities relevant to high energy density science, many approaches to atomic-scale modeling have been developed that take advantage of simplifying assumptions. In the classical plasma limit of very high temperatures and very low densities, atoms are often assumed to be fully ionized and the electron and ion energy distributions are often taken to be simple thermal Maxwellians. The kinetic models that operate in this regime use statistical methods to describe the properties of the plasma. The most sophisticated kinetic models can incorporate ionization and dynamic screening effects via, e.g. quantum statistical potentials; some can accommodate non-Maxwellian distribution functions; and the non-equilibrium atomic-kinetic models described in Section 3 can describe the occupations of detailed electronic configurations. But kinetic models are fundamentally classical: they often struggle to incorporate quantum effects such as electronic degeneracy and almost invariably treat ions as an ideal gas. In the condensed matter limit of high density and low temperature, models from solid-state physics treat the ion-ion and electron-ion interactions exactly, with approximations only made to the electron-electron interaction to prevent the cost of treating the electrons quantum mechanically from growing exponentially. The most sophisticated of these models, such as Quantum Molecular Dynamics (QMD) or density functional theory - molecular dynamics (DFT-MD) are multi-center (many-ion) models that account for electron-electron interactions through a density-dependent exchange-correlation potential in a self-consistently evolving electron-ion system. They can be used to generate equations of state, predict phase boundaries, and model electron-ion coupling rates that inform conductivities and (for TD-DFT) dynamic response functions. But these models rely on the same fictitious electronic orbitals that all DFT models do, struggle with non-equilibrium, and tend to be computationally expensive, especially for high temperatures and many-electron systems. Path-integral Monte Carlo (PIMC) methods offer an alternative to DFT that can be more accurate in certain circumstances, but they frequently have a computational cost or restrictions on temperature that prohibit their use in quite as wide a range of applications.

While many atomic-scale models operate in only limited regimes, REHEDS experiments and simulations access material conditions from cold solids to hot plasmas and thus must have information about material properties over a wide range of regimes. This requires combining regime-specific models to provide a continuous set of tabulated material properties, which is a significant challenge. Further, since few models provide data for all material properties, simulations often draw on tables for EOS, transport coefficients, and opacities calculated with different models. For example, melting and metal-insulator transitions may occur at different conditions in a given EOS table than they do in a conductivity table derived from a different atomic-scale model [26, 27]. Such inconsistencies can lead to instabilities and unphysical behavior in simulations. These considerations motivate the first line of research in this LDRD: to develop a single atomic-scale model that can span a wide range of material conditions and provide a complete set of material properties. While such a model may not be locally as accurate as more specialized models, its predictions will be at least internally consistent and its behavior across regimes will be driven directly by its underlying physics.

In this section, we describe our efforts to develop and extend a relatively fast and flexible DFT-based average-atom model (DFT-AA) to serve as a basis for a complete set of internally consistent material properties data, incorporating features from both kinetic and multi-center DFT models. The DFT-AA model is a single-center, fully quantum, all-electron model that can capture the statistically averaged properties of both electrons and ions over a very wide range of temperatures and densities, with each run taking only a few minutes on a desktop. It can be extended to make a wide range of predictions for material, transport, and radiative properties. Since many of these extensions invoke theories with significant degrees of freedom, we rely on the guidance of more expensive and sophisticated regime-specific models to constrain its predictions. In the following sections, we describe the fundamental structure of the DFT-AA model and its predictions of EOS, transport, and radiative properties.

2.1. Introduction to the Average-Atom Model

Average-atom models distill the complexities of multiple electronic and ionic configurations into a single, averaged ion with a self-consistent electronic potential and electron density. They have deep ties to modern density functional theory (DFT) [28–30], which asserts that all of the properties of a quantum mechanical system can be determined as functionals of the spatially dependent electron density. DFT-AA models have a long history of application to high energy density science, beginning with Thomas-Fermi models developed in the 1920s [31, 32], and are still widely used today due to their compactness, completeness, and computational efficiency.

Early average-atom models used a fluid description of the spatially dependent electron density in a given potential, derived a new (screened) potential from that density, and iterated until the screened potential and the electron-fluid response to that same potential converged. Modern-day AA models are fully quantum mechanical [33, 34]: they use the Schrödinger or Dirac equations to obtain both bound and continuum electronic orbitals in a given potential, populate those orbitals according to Fermi-Dirac statistics to obtain an electron density, and iterate until the potential and electronic density are convergent (self-consistent). Neutral pseudo-atom (NPA) models [35–37] extend AA model predictions to include ionic structure by constructing a dynamically screened inter-ionic potential that can be used to determine the average spatial distribution of the ions in strongly coupled (fluid) and weakly coupled (plasma) systems. For crystalline solids and molecular systems, these single-center models will fail to give complete and reliable predictions – although approximations that extend the applicability of AA-based transport models to solids exist and are discussed in section 2.3 below.

The DFT-AA model used in this work was originally developed as a semi-relativistic version of the Purgatorio code [34] that is used to generate equation of state and conductivity data for LLNL's LEOS databases. Before this LDRD began, the code had been substantially extended following Starrett and Saumon [37] and Johnson [38] to extend its predictions to include ionic structure, Compton scattering, and optical properties. Here, we provide a brief summary of its structure, discuss the fundamental model sensitivities to things like boundary conditions, definitions of ionization, and exchange-correlation potentials, and compare some basic predictions of the model to the much more sophisticated (and expensive) multi-ion-center

DFT-MD code VASP [39–41]. Atomic units ($\hbar = m_e = e = a_0 = 1$) [1] are used throughout unless otherwise noted.

The inputs to the DFT-AA model are simple: a nuclear charge Z_{nuc}, a temperature T, and a mass density ρ. The density and nuclear charge are used to define an ion density $n_i = N_A \rho / aw\, a_0^3$ (with N_A Avogadro's number and aw the atomic weight) and the Wigner-Seitz radius $R_{WS} = (3/(4\pi n_i))^{1/3}$ that defines space-filling ion spheres. The model uses a muffin-tin ion distribution that is zero for $r < R_{WS}$ and unity beyond, and makes an initial guess at a potential $V(r)$ that interpolates from $-Z_{nuc}/r$ at small r to zero at $r = R_{WS}$. The model solves a semirelativistic version of the Schrödinger equation in the given potential, determining the radial dependence of bound ($P_{n\ell}$) and continuum ($P_{\varepsilon\ell}$) electronic orbitals, which are populated according to their statistical weights $g_a = 2(2\ell_a + 1)$ and the Fermi distribution $f(\varepsilon_a;\mu) = (1 + e^{(\varepsilon_a - \mu)/\tau})^{-1}$, with $\tau = k_B T$ (in this chapter, τ indicates temperatures in atomic energy units). The chemical potential μ is variationally constrained to enforce neutrality within each sphere. The total electron charge density,

$$4\pi r^2 n_e(r) = \sum_a f(\varepsilon_a;\mu) g_a P_a^2(r), \tag{1}$$

is in turn used to determine a new potential,

$$V(r) = -\frac{Z_{nuc}}{r} + \int_0^{R_{WS}} \frac{n_e(r')d\mathbf{r}'}{|\mathbf{r} - \mathbf{r}'|} + V_{xc}(r), \tag{2}$$

with the first term accounting for the nuclear charge, the second term accounting for self-consistent screening, and the last term an exchange-correlation potential, which we take to be $V_{xc}(r) = -[3n_e(r)/\pi]^{1/3} + V_c(r)$ using exchange in the local density approximation (LDA) and a Hedin-Lundquist correlation potential [42]. This procedure is iterated until $n_e(r)$ and $V(r)$ converge, yielding a complete set of bound-state orbital binding energies $\varepsilon_{n\ell}$, radial wavefunctions $P_{n\ell}(r)$, and average occupations $o_{n\ell} = g_\ell f(\varepsilon_{n\ell};\mu) \int_0^{R_{WS}} P_{n\ell}^2(r)dr$ along with continuum wavefunctions $P_{\varepsilon\ell}(r)$, a continuum density of states (DOS) $X(\varepsilon) = \sum_\ell X_\ell(\varepsilon)$, with $X_\ell(\varepsilon) = 4\pi g_\ell \int_0^{R_{WS}} P_{\varepsilon\ell}^2(r)dr$, and phase shifts η_ℓ for each of the distorted continuum waves. The model also provides several plausible definitions for the average ionization Z^* [43], a self-consistent chemical potential μ, and a self-consistent electron density distribution $n_e(r)$. The model runs in a few minutes on a desktop for any element, temperature, and density.

To obtain the ion distribution function, we solve an additional set of self-consistent equations similar to the above, but excluding the central charge. This provides an external electron density $n_e^{ext}(r)$ that is used to define the screening density $n_e^{scr}(r) = n_e(r) - n_e^{ext}(r) - n_e^{ion}(r)$ that informs the inter-ionic potential and ionic distribution. There are several plausible choices for the definition of $n_e^{ion}(r)$ [36], which are related to the choice of Z^* and are discussed further below.

[1] Some useful relations are:
energy: 1 au = 1 Ha = 27.2 eV
length: 1 au = 0.529 Å = 0.529×10^{-8} cm
time: 1 au = 24.2×10^{-18} s
pressure: 1 au = 294 Mbar
temperature: 1 eV = 11605 K

With this additional step we supplement the complete and self-consistent set of average electronic structure information with a self-consistent picture of the average ionic structure. [2]

This DFT-AA model is rigorously self-consistent but not fully self-constrained. Its predictions will vary with choices for a) the exchange-correlation potential (as is true for all DFT models), b) the boundary conditions ($V(R_{WS})$ and/or $P_{n\ell}(R_{WS})$ – see [11]), and c) the definition of the screening potential (alternatively, the choice of Z^* and $n_e^{ion}(r)$). To help constrain these choices, we turn to multi-center DFT-MD models, which provide first-principles predictions of electronic and ionic structure that are sensitive primarily to the exchange-correlation potential. By fixing the exchange potential to be the LDA in both the DFT-AA and DFT-MD models, we can use model comparisons to constrain our remaining choices for DFT-AA. These rigorous comparisons for both the static properties discussed here and the dynamic properties discussed in later sections were a key part of the success of the LDRD.

Here, we use solid-density iron as an exemplar ($Z_{nuc} = 26, \rho = 7.9$ g/cc, $T = 1$ eV). This many-electron system has a highly structured continuum density of states that leads to a profound difference in two plausible definitions of Z^*, and so provides a good test of our model choices. The top panel of fig. 2-1 shows the energy-dependent density of states for the valence bound ($\varepsilon < 0$) and continuum ($\varepsilon > 0$) electrons. The states have been broadened in the DFT-AA model for comparison with the multi-center DFT-MD code VASP and shifted by 1.4 eV to align the chemical potentials of the two models (10.4 eV for DFT-AA and 11.8 eV for DFT-MD). Overall, the agreement is quite good, indicating that the DFT-AA model captures the average quantum electronic structure of even this complicated material rather well. This (along with other comparisons not shown) supports our choice of boundary conditions that force $V(R_{WS}) = 0$ and place no constraints on $P(r)$ or $dP(r)/dr$. Note that while the $3s$ and $3p$ states in both codes are clearly bound, the "scar" of the $3d$ state (pressure-ionized from a bound state at lower densities) is solidly in the continuum with $\varepsilon > 0$. The unstructured ideal density of states, $X^i = (2\varepsilon)^{1/2}/(n_i\pi^2)$, which represents the allowed states for plane-wave ("free") electrons, is given by the dashed line. Here, X^i is much lower than the quantum DOS. The chemical potential of around 11 eV is, in this degeneracy-dominated system, approximately equal to the Fermi energy $\varepsilon_F \approx 1.7(n_e[\text{e/cm}^3]/10^{22})^{2/3}$ eV, indicating an ionization Z^* of about 2 electrons per ion.

In the DFT-AA model, there are several plausible options for defining the average ion charge Z^* [43]. One intuitive option is to count the number of positive-energy continuum electrons: $Z_c = Z_{nuc} - Z_{bound} = \int_0^\infty X(\varepsilon) f(\varepsilon;\mu) d\varepsilon$. In our iron example, Z_c integrates over the $3d$ resonance and predicts that there are 8 continuum electrons per ion: this corresponds to the light gray $n_e^c(r)$ curve shown in fig. 2-1b. Another option is to count only the free electrons in the ideal density of states, $Z_f = \int_0^\infty X^i(\varepsilon) f(\varepsilon;\mu) d\varepsilon$ – predicting only 1.8 free electrons per ion: this corresponds to the dashed $n_e^f(r)$ curve in fig. 2-1b. These choices directly affect the definition of the bound electron density belonging to the ion, $n_e^{ion}(r)$, and therefore profoundly affect the screening electron density $n_e^{scr}(r)$ defined above. In more concrete terms: the ion-ion coupling parameter $\Gamma_{ii} = (Z^*)^2/R_{WS}\tau$ is 33 using $Z^* = Z_f$ (indicating a strongly coupled liquid), while for $Z^* = Z_c$,

[2] One can go farther with self-consistency by replacing the muffin-tin/Heaviside ion distribution function that was used to calculate the initial electronic structure with the self-consistent $g(r)$, but Starrett and Saumon have shown that the resultant changes to the electronic structure (and therefore subsequent $g(r)$) are small [37]; thus we stop at this step.

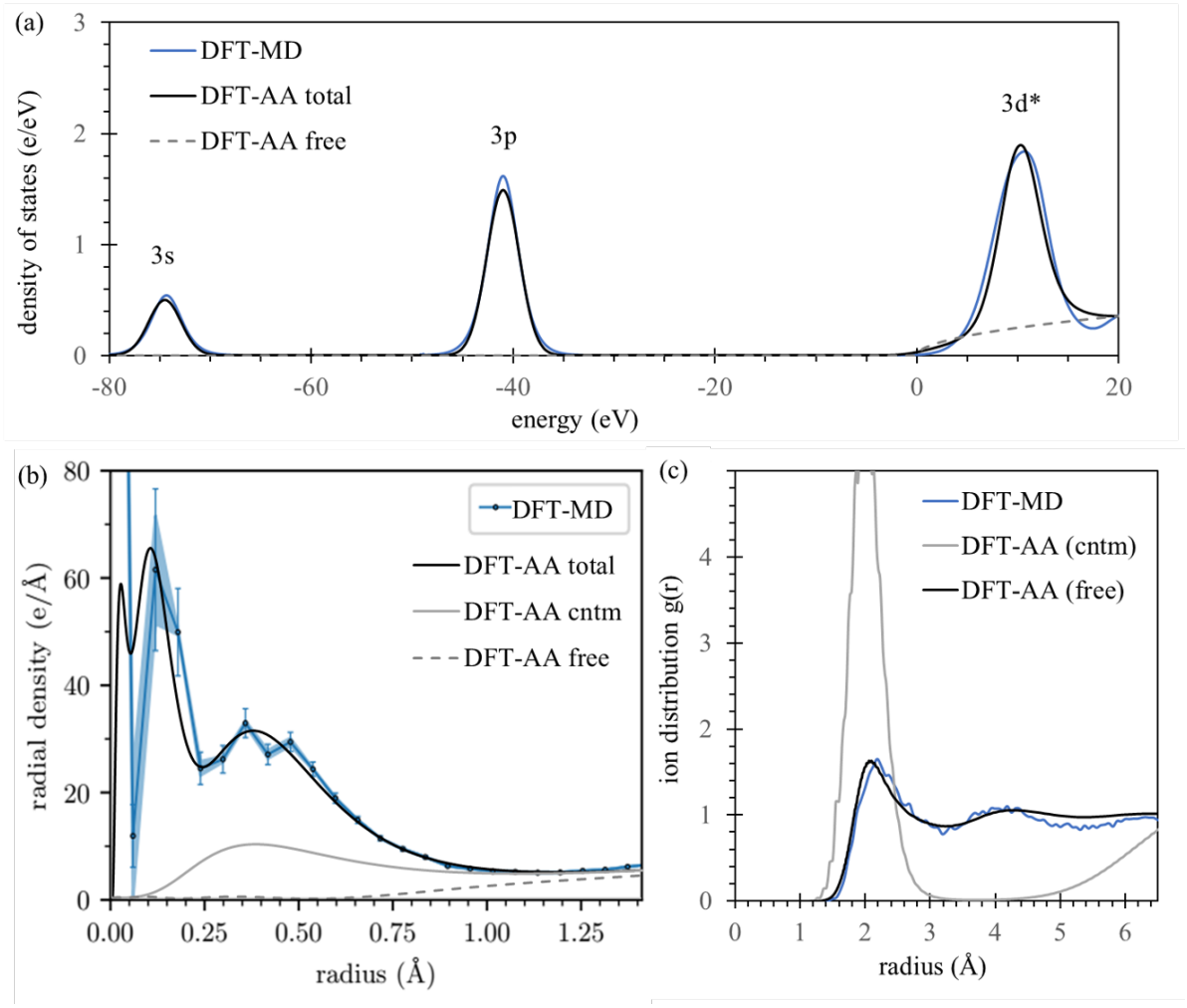

Figure 2-1 A comparison of multi-center DFT and DFT-MD data and our DFT-AA model for iron at $\rho = 7.9$ g/cc and $T = 1$ eV: (a) valence-shell electronic densities of state, (b) radial electron densities with error bars representing averages over ions for DFT-MD and two plausible definitions of ionized electrons in DFT-AA, and (c), radial ion distributions for the two definitions of ionization.

$\Gamma_{ii} = 653$ – well above the $\Gamma_{ii} \approx 172$ melt boundary of the simple one-component plasma (OCP) model – that is, well into the solid regime. A comparison of the resultant radial ion distribution functions $g(r)$ with the first-principles DFT-MD result is shown in fig. 2-1c: using Z_f as the number of screening electrons gives excellent agreement between DFT-AA and DFT-MD, while using Z_c leads to striking disagreement. [3] This result definitively constrains our choices of Z^*: whenever we consider phenomena that rely on the free response of electrons that can spread throughout space, we will use Z_f, plane waves $P^i_{\varepsilon\ell}(r)$, and the ideal density of states $X^i(\varepsilon)$; excluding the spatially localized component of the continuum electrons. By contrast, whenever we consider phenomena that must satisfy sum rules or that require matrix elements based on the actual quantum distorted-wave states, we will use Z_c, $P_{\varepsilon\ell}(r)$, and $X(\varepsilon)$.

The necessity of separating "free" electronic states from continuum electronic states requires a formal treatment that goes beyond the two relatively simple definitions of Z^* defined above, which were based on the energy-dependent densities of states: we must also be able to define the radial dependence of both free and continuum states in order to calculate the ion density $n_e^{ion}(r)$ used in the definition of the screening density $n_e^{scr}(r)$. So far, our DFT-AA model provides only the full distorted-wave orbitals $P_{\varepsilon\ell}$ and thus $n_e^c(r)$ – but not $n_e^f(r)$ or $P_{n\ell^*}$ for the features in the continuum density of states that are the "scars" of bound $P_{n\ell}$ states. These resonances retain some bound-state character (with high probability to be near the nucleus, as illustrated by the substantial $3d$ continuum feature evident below 0.6 Å in fig. 2-1b), but also acquire long-range oscillations that resemble phase-shifted free-wave states with radial wavefunctions $P^i_{\varepsilon\ell} = (2/\pi p)^{1/2} pr j_\ell(pr)$, with $p = (2\varepsilon)^{1/2}$ and j_ℓ the spherical Bessel functions. As we step through the energies associated with each resonant feature, the phase shifts of the long-range $P_{\varepsilon\ell}$ functions change over 2π [34], so that an integral over the resonances yields a "quasibound" $P_{n\ell^*}$ state with finite extent. We thus define quasibound radial wavefunctions as $P_{n\ell^*} = \int_{res} [P_{\varepsilon\ell} X_\ell - P^i_{\varepsilon\ell} X^i_\ell] d\varepsilon$, where the integral is over the resonance peak, and normalize the resonance orbitals by setting $\int_0^{R_{WS}} P^2_{n\ell^*} dr$ to $f_s = \int_{res} [X_\ell - X^i_\ell] d\varepsilon / \int_{res} X_\ell d\varepsilon$. This gradually reduces effective statistical weights as resonances merge into the continuum, a reduction analogous to – and continuous with – the reduction factors of $\int_0^{R_{WS}} P^2_{n\ell} dr$ imposed for bound orbitals that extend beyond the ion sphere. In the remainder of this report, we use these quasibound states only to define the screening density defined above (through their inclusion in $n_e^{ion}(r)$) and to compute Slater coefficients for the multiconfiguration expansion of the model (described in section 2.6). [4]

[3] The Quantum Ornstein-Zernike equations that are used to calculate $g(r)$ in the DFT-AA model are unstable for high values of Γ, so the continuum-based $g(r)$ shown in the figure is unconverged – and in any case, the $g(r)$ of a crystalline solid would have distinct, narrow peaks corresponding to its lattice structure rather than the spherically averaged representation of an AA model. Nonetheless, the figure is a reasonable representation of the dramatic differences in ionic structure between liquids (where the kinetic energy of ions has the same order of magnitude as the potential energy between them) and solids (where the ion kinetic energy is dwarfed by the interionic potential).

[4] In our early calculations of scattering spectra [12], we proposed to use these quasibound states identically to bound states in calculations of bound-bound and bound-free scattering features; however in the last year of this LDRD we derived the more consistent treatment now presented in section 2.4.

2.2. Equations of State

The equation of state (EOS) is an essential closure term for hydrodynamic simulations: it determines how materials respond to external forces. The EOS provides a relationship among thermodynamic variables such as pressure, density (or volume), and temperature that satisfy Maxwell's thermodynamic relations. For example:

$$\partial U = \tau \partial S - P \partial V \tag{3}$$

with U the internal energy, S the entropy, P the pressure, and $V = 1/n_i$ the volume. A very simple equation of state is the ideal gas equation: $PV = nRT$, from which we can derive a simple estimate for the pressure knowing only the ionization Z^*: $P[\text{Mbar}] \approx (\rho/aw)T[\text{eV}](1+Z^*)$, with ρ the mass density and aw the atomic weight. The ideal-gas pressure includes both ion and electron pressures in the factor $(1+Z^*)$, and so the electron-pressure term is sensitive to our choice of Z^*. The left panel of fig. 2-2 shows the temperature dependence of Z_f (dashed) and Z_c (light dashed) from the DFT-AA model along three isochors about solid density for aluminum (top) and copper (bottom), and compares these to Z^* from the SESAME tables (93721 for aluminum and 3325 and 29325 for copper). [5] The Z_c have generally worse agreement with the reference ionization values, especially at low temperatures, and for copper Z_c exhibits sharp discontinuities as increasing temperatures allow re-binding of the pressure-ionized $3d^*$ resonances illustrated in the previous section (see also [43]). We thus take the electron pressure to be a phenomena that depends on the "truly free" electrons Z_f rather than on the positive-energy electrons Z_c. The light dashed lines on the right panels show that the total (ion + electron) ideal-gas pressures using $Z^* = Z_f$ are in good agreement with the SESAME tables at high temperatures, but do not capture degeneracy effects important at high density and low temperature.

To account for degeneracy effects, we use a modification of the ideal-gas expression for the electron pressure: $P_e = (2\tau)^{5/2} I_{3/2}(\mu/\tau)/(6\pi^2)$, derived from the quantum mechanical expression for the stress tensor [44], where $I_{3/2}$ is the Fermi integral assuming an ideal density of states. The heavier dashed lines on the pressure plot in fig. 2-2 show the results from this expression for the electrons (keeping the ideal-gas approximation for the ions). This simple expression agrees with the tables down to much lower temperatures than the ideal-gas P_e and is the preferred option for our DFT-AA (and non-LTE-model) tables, since it is always positive and is not particularly sensitive to numerical precision.

We also routinely calculate two other estimates of the electron pressure from our DFT-AA models: 1) $P_e^{Vir} = (n_i/3)(2U - U_p)$, an expression derived from the Virial theorem [45] with U the total internal energy and U_p the internal potential energy (see below), and 2) a variational $P_e^{var} = -(\partial F/\partial V)|_\tau$, with $F = U - \tau S$ the Helmholtz free energy and S the entropy. We find that the Virial and variational pressures demand extreme numerical precision [34], and while the three expressions for pressure (modified ideal, Virial, and variational) agree to within 5% at high temperatures, P_e^{Vir} tends to asymptote to a too-large constant positive value at low temperatures and P_e^{var} tends to asymptote to a constant negative value; neither of these pressures are shown in fig. 2-2.

[5] From John Carpenter and Kyle Cochrane

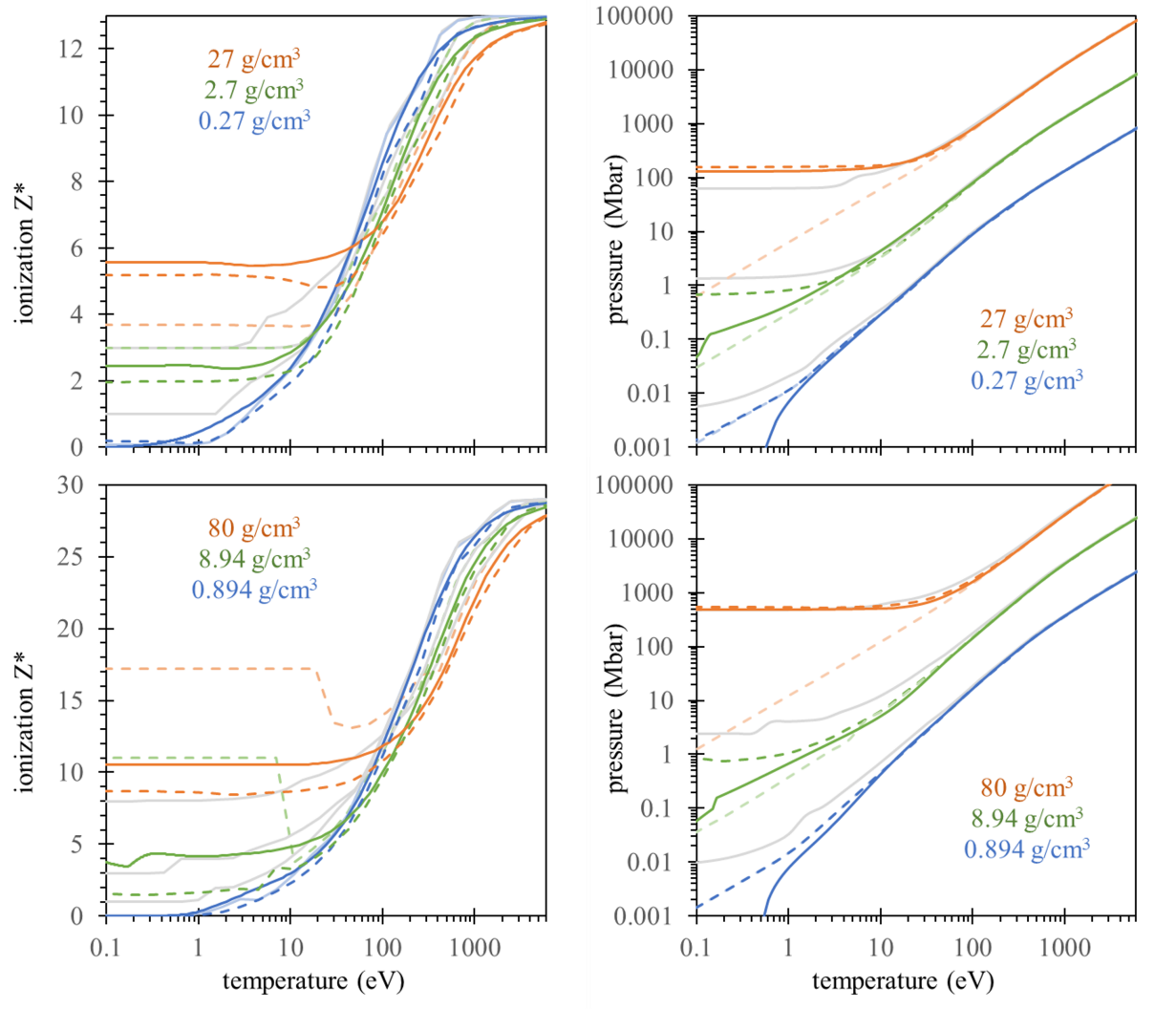

Figure 2-2 A comparison of average ionization (left) and total (ion + electron) pressure (right) for aluminum (top) and copper (bottom) isochors about solid density. Colors correspond to the densities as labeled. The solid lines are from SESAME tables. For ionization, the dashed lines are DFT-AA Z_f and Z_c (light). For pressures, the dashed lines are DFT-AA degenerate and non-degenerate (light) ideal electron pressures. The light gray lines are LTE results from our screened-hydrogenic CR model ([1]; see section 3) to illustrate the relative accuracy of inline non-LTE models.

To enable the variational pressure calculation – as well as calculations of other variational quantities such as heat capacities ($C_V = (\partial U/\partial T)|_V$) and compressibilities ($\kappa_T = -(1/V)(\partial V/\partial P)|_T = S_{ii}(0)/(n_i\tau)$) – at single temperature-density points and on coarse tables, we have built in additional convergence loops in the DFT-AA model that recompute the self-consistent electronic structure under small changes in density and temperature. For variations in density, we compresses the radial grid from $r \to r/f_r$ (with $f_r \approx 1.02$) and leave the effective potential unchanged as an initial guess; this provides a starting point for convergence that is generally good to within a few percent and offers a significant speedup over starting from scratch. While these additional convergence loops increase the computational time, they extend the capabilities of the model and enable rigorous checks on thermodynamic consistency (that is, simultaneous satisfaction of Maxwell's thermodynamic relations) on coarse temperature-density grids.

Other thermodynamic quantities of interest include the electron internal energy U and entropy S, which enable generation of Hugoniot curves that minimize the quantity $(U-U^0)+\frac{1}{2}(V-V^0)(P+P^0)$ for some reference density ρ^0. In our atomic-kinetic non-LTE models, the internal energy is taken to be just a weighted sum over the energies of bound configurations (referenced to the isolated neutral ion) plus an ideal-gas representation of the kinetic energy in the free electrons and ions: $3/2\tau(1+Z^*)$. In the DFT-AA model, we compute the kinetic U_k and potential U_p contributions to the free energy $U = U_k + U_p$ and the entropy directly from the self-consistent quantum mechanical electron densities and densities of states, removing any dependence on the choice of Z^*:

$$U_k = \int_0^\infty X(\varepsilon) f(\varepsilon) d\varepsilon + \int_0^{R_{WS}} n_e V(r) dr \tag{4}$$

$$U_p = \int_0^{R_{WS}} n_e \left[\varepsilon_{xc}(r) - \frac{Z_{nuc}}{r} \right] dr + \frac{1}{2} \int_0^{R_{WS}} \frac{n_e(r') d\mathbf{r}'}{|\mathbf{r}-\mathbf{r}'|} \tag{5}$$

$$S = -\int_0^\infty X(\varepsilon) \left[f(\varepsilon) \ln[f(\varepsilon)] + [1-f(\varepsilon)] \ln[1-f(\varepsilon)] \right] d\varepsilon \tag{6}$$

where $X(\varepsilon)$ are the densities of states ($X(\varepsilon_{n\ell}) = g_\ell \int_0^{R_{WS}} P_{n\ell}^2 dr \delta(\varepsilon - \varepsilon_{n\ell})$ for bound states), $f(\varepsilon)$ is the Fermi-Dirac occupation factor, and $\varepsilon_{xc}(r)$ is the exchange-correlation energy. Strict convergence and high numerical precision are particularly important for the calculation of U, since it includes several large positive and large negative terms. Examples of Hugoniot curves calculated using an earlier version of our DFT-AA code were included in a fairly recent compilation of data from an EOS code comparison workshop [46].

Future work in this area will focus on understanding the requirements of rad-hydro simulations for stringent thermodynamic consistency and testing that consistency in the DFT-AA code. We will also develop a more sophisticated treatment of the thermodynamic properties of the ions [47, 48], including cold curves and approximate molecular bonding. These efforts should improve the agreement of our DFT-AA model with existing EOS tables at low temperatures. While we do not ever expect perfect agreement with existing tables, which are often bespoke and carefully

modified to match existing data, improving the low-temperature agreement would make our tables easier to adjust to trusted values and will increase confidence in non-LTE calculations that cannot be checked against existing high-accuracy tables.

2.3. Static Transport Coefficients

Transport properties such as electrical and thermal conductivities, viscosities, and sound speeds ($c_s = (\gamma/\kappa_T\rho)^{1/2}$) [49] play critical roles in the energy balance and instability development of HED systems. Electrical conductivity is particularly important for REHEDS on the Z machine, which uses electrical current to drive experiments. Presently, Sandia's approach to tabulating electrical conductivities uses targeted DFT-MD calculations (discussed below) to correct the high-density and low-temperature behavior of Z^*-parameterized analytical calculations such as the Lee-More-Desjarlais (LMD) [50] model, which modifies the original Lee-More [51] model to improve agreement with (sparse) experimental data and targeted DFT-MD calculations. At LLNL, self-consistent data from the DFT-AA code Purgatorio is used to generate conductivities following the Ziman approach for liquid metals [52, 53]. In this LDRD, we significantly improved the internal consistency of the Ziman approach used in our DFT-AA model, modified the Lee-More calculations used in our atomic-kinetic models, studied first-principles approaches to transport calculations with multi-atom models [24, 25], and began a collaboration with UIUC under Sandia's SAA program to study first-principles modeling of electron-electron collisions (see Appendix A).

The Ziman-Evans approach to electron-ion conductivity is a linear-response formulation developed for liquid metals that has been extended to plasmas and is widely used with DFT-AA models [53–55]. In this approach, the static (DC) electrical conductivity is related to the frequency of electron-ion collisions that halt the acceleration of transport electrons: $\sigma_{ei}^{el} = Z_0^* n_i/\nu_{ei}^Z$, with Z_0^* the number of transport electrons per ion and

$$\nu_{ei}^Z = \frac{1}{3\pi Z_\nu^*}\int_0^\infty d\varepsilon\left(-\frac{\partial f(\varepsilon)}{\partial\varepsilon}\right)\int_0^{2p} q^3\frac{\partial\sigma^{tr}(\varepsilon,\theta)}{\partial\theta}S_{ii}(q)dq. \tag{7}$$

To account for strong collisions, we use a T-matrix differential momentum-transport cross section:

$$\frac{\partial\sigma^{tr}(\varepsilon,\theta)}{\partial\theta} = \frac{1}{p^2}\left|\sum_{\ell=0}^{\infty}(2\ell+1)\sin\eta_\ell\, e^{i\eta_\ell}P_\ell(\cos\theta)\right|^2, \tag{8}$$

with $q^2 = 2p^2(1-\cos\theta)$, P_ℓ the Legendre polynomials, and η_ℓ the phase shifts. Here, Z_ν^* is a normalization factor that must be consistent with the energy integral, which is a finite-temperature generalization of Fermi surface properties related to the density of states. For the ideal density of states implied by the expression for ν_{ei}^Z above, this requires that $Z_\nu^* = Z_f$ [56]. However, the ideal density of states is not consistent with the differential cross section, which represents collisions with all of the continuum electrons, or with the self-consistent quantum density of states in the

material. To count all of the continuum electrons, it has been proposed to define a new chemical potential μ_c that satisfies $\int_0^\infty X^i(\varepsilon) f(\varepsilon;\mu_c) d\varepsilon = Z_c$ [54]; but this, too, is inconsistent with the quantum density of states. One of the major changes we have made to the standard Ziman approach is to perform the energy integral for ν_{ei}^Z with the factor $X(\varepsilon)/X^i(\varepsilon)$, so that ν_{ei}^Z captures interactions with all of the continuum electrons in the self-consistent quantum density of states without invoking a modified chemical potential (see Starrett et al. [4]). This change requires that $Z_\nu^* = Z_c$, tends to increase ν_{ei}^Z over calculations that assume $X^i(\varepsilon)$, and improves the continuity of ν_{ei}^Z under pressure ionization.

The number of charge carriers that directly informs the electrical conductivity through $\sigma_{ei}^{el} = Z_0^* n_i/\nu_{ei}^Z$ does not have the same variational constraint as Z_ν^*, so we appeal to comparisons with multi-atom models to guide our choice for Z_0^*. We first note that the ion-ion structure factor $S_{ii}(q)$ that appears in the expression for ν_{ei}^Z is the Fourier transform of the radial distribution function $g(r)$ discussed in section 2.1. For a transition metal with large differences between Z_f and Z_c, we have shown that the self-consistent DFT-AA $g(r)$ is in very good agreement with a DFT-MD $g(r)$ when we use Z_f for the screening electrons and in very poor agreement when we use Z_c. Here, we assign Z_f to be both the number of screening electrons per ion (used to calculate $S_{ii}(q)$ and $g(r)$) and the number of charge carriers per ion, Z_0^*, used directly in the electrical conductivity. These free electrons represent the delocalized portion of the continuum electrons that respond to electric fields – whether those fields are imposed by other ions for $S_{ii}(q)$ or externally for σ_{ei}^{el}.

For high-temperature and low-density plasmas with ion-ion coupling parameters $\Gamma_{ii} = Z_f^2/\tau R_{WS} < 10$, the above prescriptions are reasonable. However, for ions with more than one valence electron, the ν_{ei}^Z integral will always capture the first peak of the structure factor and as a result, the conductivity on any isochor will asymptote to a constant value at low temperatures (high Γ_{ii}). This does not match the observed behavior of simple solid metals, whose conductivity monotonically decreases with temperature up to T^{melt}. We thus propose a modification to the self-consistent $S_{ii}(q)$ roughly following Sterne et al. [53] and Wetta and Pain [55]: First, we define the melt temperature to occur at some Γ_{ii}^{melt} (about 172 for the one-component plasma). Above that value of Γ_{ii} (where the material is in a solid state), we use the Baiko et al. [57] prescription for a structure factor that neglects collisions on lattice vectors since these processes simply translate an electron from one lattice site to another and thus do not contribute to the ν_{ei}^Z scattering. This provides a direct T^{-1} dependence of the conductivity below the melting point. At higher temperatures, for $\Gamma_{ii} < \Gamma_{ii}^{melt}$, we use $S_{ii}(q) \to \min[1, S_{ii}(q)]$ to roughly remove the incipient lattice structure (Bragg peaks) in the liquid, resulting in a discontinuity at melt and providing good agreement with the liquid aluminum results of Wetta and Pain [55]. [6] We also incorporate these general effects into our implementation of the Lee-More model by imposing a factor $(1+\Gamma_{ii}/3)$ on all Lee-More conductivities.

Figure 2-3 shows a comparison of various static electric conductivities for aluminum and copper along the same isochors as the EOS data given in section 2.2. The solid lines are from recent

[6] Note that Wetta and Pain [55] use the full liquid structure factor (do not truncate peaks) but they also use Z_c as their number of charge carriers. The good agreement is due to the cancellation of the two effects, since using the full structure factor modestly decreases the conductivities by increasing the collision integral, while including all continuum electrons as charge carriers modestly increases it.

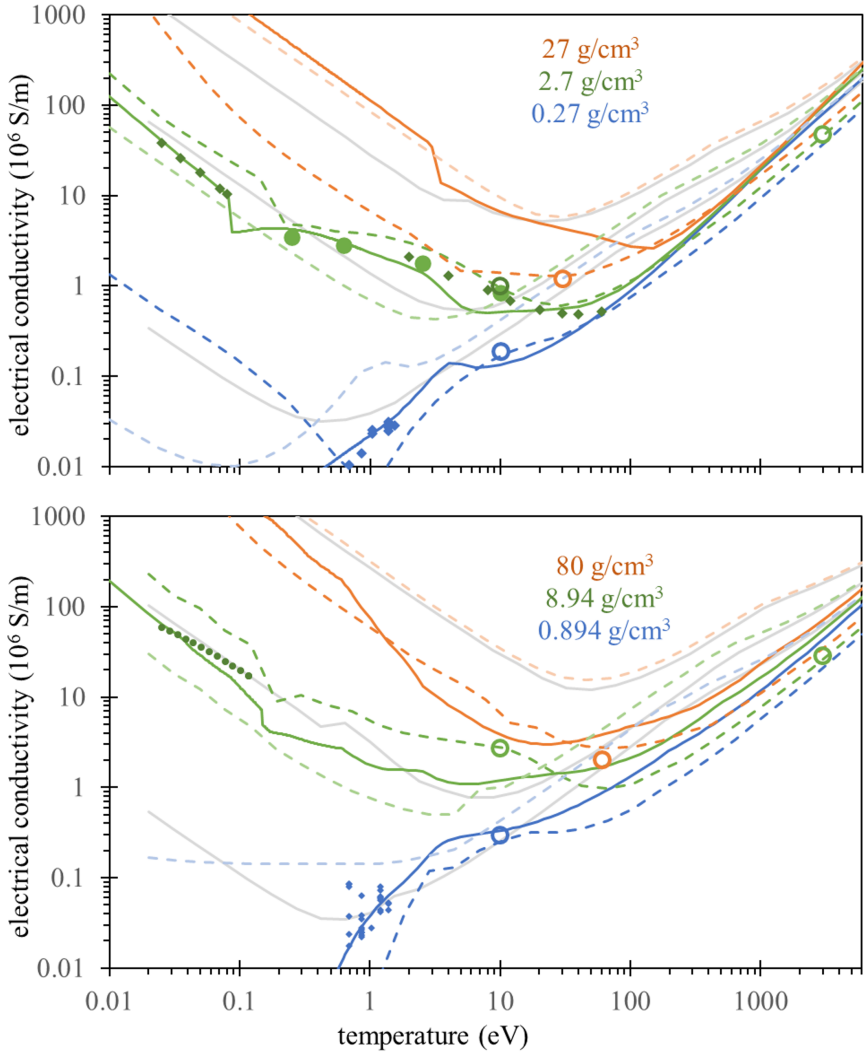

Figure 2-3 A comparison of DC electrical conductivities for aluminum (top) and copper (bottom) isochors about solid density. Colors correspond to the densities as labeled. The solid lines are from SESAME tables, based on LMD (Al) or LMD modified with select DFT-MD calculations (Cu). The light lines are our implementation of the original Lee-More model parameterized by Z_f from DFT-AA (light dashed) and from the Z^* of our atomic kinetics model (light gray). The dashed lines are from our self-consistent Ziman implementation in the DFT-AA model. Experimental data, where available, are given by small filled points [2, 3], selected Kubo-Greenwood conductivities (see sec. 2.4) are given by open circles from DFT-AA and closed circles from DFT-MD [4].

SESAME tables: for aluminum, they are simply the LMD values informed by the reference-table Z^* from fig. 2-2. For copper, the LMD values have been adjusted to match DFT-MD calculations at select points with temperatures below about 3 eV and densities with a factor of 3 of solid. The small solid points indicate data from exploding wires [3], laser experiments [2], and solid-state reference data. Dashed lines are the DFT-AA calculations described above [7] and the light lines are our implementation of Lee-More parameterized by the DFT-AA Z_f (light dashed) or our screened-hydrogenic CR model Z^* (light gray). Although our Lee-More implementation eventually reaches LMD at very high temperatures, it has significant differences from LMD at most temperatures that are not solely attributable to differences in Z^* or the structure-factor corrections: we intend to implement LMD to reconcile these differences.

Of more interest to this LDRD are the differences between the low-temperature reference data, the reference SESAME table conductivities, and our internally consistent Ziman model, which are significant. While our Ziman conductivities follow the general trends of the LMD (Al) and adjusted-LMD (Cu) curves, they differ by factors of two or more in magnitude and exhibit notable features in three different regimes.

First, at high temperatures (where the both Al and Cu reference tables use LMD), the DFT-AA conductivities are systematically smaller than LMD values. In this regime, there is no sensitivity to the structure factor and the Z^* from the different codes agree fairly well, so this difference is primarily attributable to collision frequencies and cross sections. Here, the DFT-AA model is much more sophisticated than LMD (which uses impact parameters to estimate collisions) and thus may be preferred – however, there are no experiments or DFT-MD calculations in this regime to verify that preference. We have plotted conductivities extracted from the zero-frequency limits of Kubo-Greenwood calculations that use DFT-AA orbital data but an entirely different formalism than the Ziman calculations (see sec. 2.4) at selected points (open circles), which mostly agree rather well with the DFT-AA Ziman values. For Al, we have also plotted Kubo-Greenwood calculations from DFT-MD [4] (filled circles), which support LMD values below $T \approx 3$ eV and DFT-AA values at 10 eV.

A second region of interest is at solid density around the melting discontinuity. Here, the Γ_{ii}-parameterized DFT-AA model only roughly captures the melt temperatures (reference values of T^{melt} are 0.08 eV for Al and 0.12 eV for Cu). It also gives conductivities that are systematically larger than the reference curves, which are here informed by reference data and DFT-MD. These are significant and real errors likely driven by the simplifications of the spherically symmetric DFT-AA model, especially in the ion structure, and would need to be adjusted before use in simulation codes.

Finally, we note the wide variation in model predictions in the low-density and low-temperature region. These disagreements are driven primarily by differences in Z^* and are consistent with large discrepancies observed in focused code comparisons of other materials [59].

Since precious little benchmark-quality data exists for transport coefficients, the multi-center DFT codes offer crucial constraints. DFT-MD and TDDFT can both be used to compute the optical

[7] For this figure, we have used a fit to the OCP approximation for the structure factors from [58], since the full self-consistent structure factor calculations are relatively expensive and the resulting conductivities generally differ from the OCP approximation by less than 10%.

conductivity of materials from first principles. Multi-atom approaches include those based upon the Kubo-Greenwood formula, linear-response (LR) TDDFT, and real-time (RT) TDDFT. LR-TDDFT is formulated in terms of a Dyson equation for the response function, typically rendered in terms of a non-interacting set of Kohn-Sham orbitals, and corrections due to an electronic Hartree and exchange-correlation kernel [60, 61]. In fact, the Kubo-Greenwood formalism as typically implemented in the HEDS community [62] is equivalent to LR-TDDFT in the limit in which the exchange-correlation kernel is zero, i.e., the Kubo-Greenwood conductivity is consistent with the zeroth-order solution to the LR-TDDFT Dyson equation. RT-TDDFT is formulated in terms of time-dependent Kohn-Sham equations and the conductivity can be extracted by contriving a scenario in which the time dependence of the underlying Hamiltonian is due to an electric field that drives a current through a supercell, to which Ohm's law can be applied [25, 63, 64]. Furthermore, LR-TDDFT and RT-TDDFT should give identical results in the limit that the perturbing vector potential that drives the current is sufficiently weak that nonlinear corrections to the response are negligible. Nevertheless, differences between the two formalisms have been documented and require further study [24].

The three multi-atom approaches to computing conductivities can be cast as existing within a consistent methodological hierarchy, and it is worth remarking on improvements that could be made to all three of them. As with many DFT methods, the key deficiency is due to the choice of an exchange-correlation potential or kernel, i.e., roughly the first and second derivatives of the exchange-correlation functional. The KG formalism completely neglects these effects, whereas LR- and RT-TDDFT are typically limited to energy-independent (or adiabatic) approximations used in conventional methods. While we know that the exact exchange-correlation kernel for TDDFT is far more complicated than the adiabatic approximation allows, developing approximations that capture many of these behaviors has been a long-standing challenge. Among the features of the exact kernel that have been successfully modeled are the long-range nature of the Hartree term. It has previously been demonstrated that deficiencies in capturing electron-electron scattering processes in the KG formalism result in predictions that are inconsistent with known limits of plasma kinetic theories [65]. While it is unclear whether even local adiabatic approximations would suffice to restore this limit, e.g., computing the same properties using an adiabatic local density approximation, this remains an important area for future study that we hope will be addressed by some of the more direct inquiries into electron-electron scattering processes being considered in Appendix A.

We note that the ν_{ei} produced by the DFT-AA model for electrical conductivities can also be used to estimate thermal conductivities and viscosities, providing a relatively complete set of internally consistent transport coefficients over a wide parameter range. Accurate electron-electron collisions [66–68] are expected to be especially important for thermal conductivities [65, 67] and will be included in our future work. We will also consider whether inelastic processes (which change the energy of impact electrons rather than just their direction) might influence the static properties as they do the dynamic properties discussed below. We will implement the Lee-More-Desjarlais [50] improvements to our current Lee-More implementation for our CR models, look for refinements of the simple modifications of $S_{ii}(q)$ described above that could improve the accuracy of our Ziman model at low temperatures and high densities, and seek to validate our predictions at high temperatures against independent approaches (e.g. [67]).

Additionally, we will explore how the self-consistent ion structure factors may inform ion transport properties such as diffusivity and viscosity [69].

2.4. Dynamic Response Functions

The static transport properties described above provide important information about the response of materials to zero-frequency external gradients (of electric potentials and temperatures). However, these static properties are exceedingly difficult to measure in HED experiments, since benchmark measurements require 1) creation of a uniform sample of matter at extreme conditions, 2) independent characterization of those conditions, and 3) independent diagnostics of the transport properties. None of these requirements are easy to meet, but diagnosing static properties is particularly challenging since most active experimental probes (lasers, x-rays) and many direct observables (emission, absorption, and scattering spectra) are frequency-dependent. This motivates us to go beyond calculations of static properties to dynamic (frequency-dependent) properties.

The Kubo-Greenwood (KG) approach to dynamic conductivities offers a baseline for our investigations into frequency-dependent responses. As noted above, KG is a critical tool for extracting even static conductivities from multi-atom DFT-MD models. For the DFT-AA model, Johnson et al. [70] have derived a relatively straightforward expression for the optical conductivity based on the dipole cross sections between every pair of quantum electronic states. The KG dynamic conductivity includes bound-bound, bound-continuum, and continuum-continuum contributions, as illustrated in the top panel of fig. 2-4, and is given by:

$$\sigma_r(\omega) = \frac{2\pi n_i}{\omega} \int d\varepsilon [f(\varepsilon_a) - f(\varepsilon_{a'})] \int d^3 q_a \int d^3 q_{a'} |\langle P_a | \mathbf{v} | P_{a'} \rangle|^2 \delta(\varepsilon_a - \varepsilon_{a'} - \omega) \tag{9}$$

The KG dynamic conductivity, which gives a complete picture of the dipole transitions among all excited states, is extremely powerful. We can generate the imaginary part of the dynamic conductivity (or any other dynamic quantity) using the Kramers-Kronig dispersion relation: $\sigma_i(\omega) = -\frac{2}{\pi} \mathrm{P} \int d\omega' \sigma_r(\omega') \omega / (\omega'^2 - \omega^2)$, where P is the principal value (avoiding the poles), and then generate a wide range of dynamic material properties including the dielectric function $\varepsilon(\omega)$, the index of refraction $n(\omega)$, and the absorption opacity $\kappa(\omega)$ [71]:

$$\varepsilon_r(\omega) = 1 - \frac{4\pi}{\omega} \sigma_i(\omega) \tag{10}$$

$$\varepsilon_i(\omega) = \frac{4\pi}{\omega} \sigma_r(\omega) \tag{11}$$

$$n(\omega) = \frac{1}{2^{1/2}} [|\varepsilon(\omega)| + \varepsilon_r(\omega)]^{1/2} \tag{12}$$

$$\kappa(\omega) = \frac{4\pi}{n(\omega)c}\sigma(\omega). \tag{13}$$

The KG expression given in Eq. (9) diverges as $1/\omega^2$ in the low-frequency limit due to the continuum electron contribution. To regularize the divergence, we can impose a Lorentzian broadening/ Drude form on the low-frequency conductivity: $\sigma^{ff}(\omega) = \sigma^{ff}(0)/[1+(\omega/\nu^{KG})^2]$. For plane-wave free electrons, this is the entire free-free contribution to the dynamic conductivity and, by construction, perfectly satisfies the conductivity sum rule $\int_0^\infty \sigma^{ff}(\omega)d\omega = (\pi/2)Z_f n_i$ for *any* value of ν^{KG}, so we typically impose the Ziman value, setting $\nu^{KG} = \nu^Z$. Additionally, the DC limit of the dynamic collision frequency in the Drude model $\nu^{ff}(0) = n_i Z_f/\sigma^{ff}(0)$ is identical to the regularizing frequency ν^{KG}, and inversion of the complex transform suggested by [72], $\sigma^{ff}(\omega) = Z_f n_i/[\nu^{ff}(\omega) - i\omega]$, returns a constant $\mathrm{Re}\{\nu^{ff}(\omega)\}$ that is also identical to ν^{KG}.

Using the distorted wave continuum electrons from the DFT-AA model in the Kubo-Greenwood expression complicates this picture. The quantum $\sigma^{cc}(\omega)$ modifies the simple $1/\omega^2$ behavior, typically adding an additional feature at finite frequency that corresponds roughly to inelastic (absorbing) transitions among the continuum electrons, as illustrated in the top panel of fig. 2-4. To regularize the quantum $\sigma^{cc}(\omega)$, we multiply it by a factor $1/[1+(\nu^{KG}/\omega)^2]$ and search for the collision frequency ν^{KG} that will satisfy the sum rule $\int_0^\infty \sigma^{cc}(\omega)d\omega = (\pi/2)Z_c n_i$ [73]. This generally returns a value of ν^{KG} that is close to the Ziman ν^Z for cases where ν^Z is not sensitive to S_{ii} (the ion structure is nowhere included in our present KG calculations, but see Starrett [74]). The complex transform of this $\sigma^{cc}(\omega)$ returns a structured $\mathrm{Re}\{\nu^{cc}(\omega)\}$ that goes to ν^{KG} at small frequencies and then increases at higher frequencies. [8] Unlike in the Drude case, the zero-frequency limit of the transformed $\sigma^{cc}(\omega)$ is *not* identical to the collision frequency implied by the DC limit of $\sigma^{cc}(\omega)$, $\nu^{cc}(0) = n_i Z_f/\sigma^{cc}(0)$, although it is often quite close. Thus there is some ambiguity as to which frequency we should assign to the conductivity for our KG calculations; the KG conductivities shown in fig. 2-3 of the previous section use ν^{KG}.

A general understanding of the dynamic electronic responses of materials to an external perturbation – particularly $\nu(\omega)$ and $\varepsilon(q,\omega)$ – is important for the interpretation of experimental scattering spectra. In the high energy density physics (HEDP) and warm dense matter (WDM) communities, x-ray based scattering methods, like x-ray Thomson scattering (XRTS) [75–78] or resonant inelastic x-ray scattering (RIXS) [79], have become essential tools for benchmarking theories of WDM and furthering our understanding of this complex regime. In our work on modeling dynamic electronic response, we have thus focused our attention on applications to XRTS.

For atomic-scale models that discriminate between the bound and free electrons, like the DFT-AA model, the Chihara decomposition has been a widely used theory for analyzing scattering spectra [80]. The decomposition states that the dynamic structure factor (DSF), which is proportional to both $\mathrm{Im}\{1/\varepsilon(\omega,q)\}$ and to the intensity of observable scattering spectra, can be split into disjoint

[8] We have noticed some discrepancies in the series transforms: while the $\nu(\omega)$ from the inversion $\nu(\omega) = Z^* n_i/\sigma(\omega) + i\omega$ is always well behaved, it does not identically return the original $\sigma(\omega)$ when used in the transform $\sigma(\omega) = Z^* n_i/[\nu(\omega) - i\omega]$. This may be related to regularizing the pole at $\omega = 0$ and/or to our choices of Z^*, and warrants further investigation.

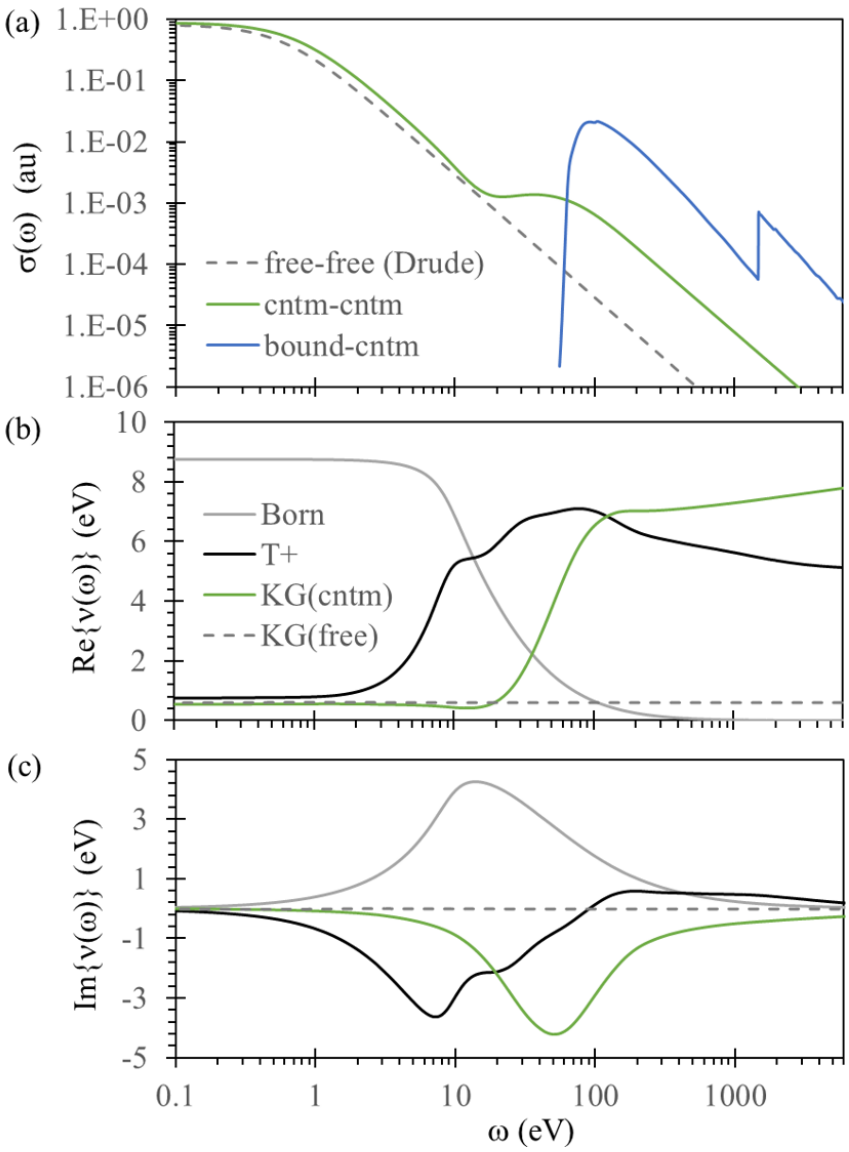

Figure 2-4 (a) Kubo-Greenwood dynamic conductivity of aluminum at $T = 1$ eV and solid density (2.7 g/cc) from the DFT-AA model, split into bound-continuum, continuum-continuum (both quantum), and free-free components (Drude-like). (b) and (c) are the real and imaginary parts of the dynamic collision frequencies $\nu(\omega)$ from various independent calculations: dashed gray lines are from a transform of the Drude-like $\sigma^{ff}(\omega)$ shown in (a); green lines are from a transform of the quantum $\sigma^{cc}(\omega)$ shown in (a); solid gray lines use simple approximations for the dynamic collision frequencies (*c.f.* [5]); and the solid black lines show the alternative form for a complete $\nu(\omega)$, including inelastic collisions, as discussed in the text.

contributions from the various scattering processes that can occur. Typically, three contributions are considered: elastic scattering from the tightly bound electrons that closely follow the ion motion, bound-free scattering that comes from scattering from bound electrons that are photoionized in the process, and free-free scattering that describes scattering from the free electrons [81, 82].

At higher temperatures comparable to electronic binding energies, thermal excitations can open additional channels for inelastic processes. Then it becomes necessary to include contributions to the scattering spectra from bound-bound transitions, a term that is mentioned in passing in [83] but which has generally been neglected in XRTS calculations. The existence of bound-bound transitions in scattering signals has been confirmed by real-time time-dependent density functional theory (TDDFT) (described below) using an approach that does not depend on the Chihara decomposition. Since bound-bound transitions depend strongly on thermal excitations, they are also a promising complement to current plasmon-based thermometry measurements. We described an early version of these results that used the quasibound states described in section 2.1 in Baczewski et al. [12], and have since improved our treatment of the continuum response to allow a more coherent picture of the free-free (continuum-continuum) scattering spectra, which we describe briefly here. Key to this new description is the inclusion of a factor $X(\varepsilon)/X^i(\varepsilon)$ in the expression of the dieletric function and a complete and consistent treatmeant of the dynamic collision frequencies $\nu(\omega)$. The self-consistent treatment of the elastic, bound-free, and bound-bound terms are well described in Baczewski et al. [12], along with a description of some intriguing results on a sharp collective scattering feature observed in TDDFT.

The elastic, bound-bound, and bound-free contributions are all computed self-consistently within the AA framework. For the free-free contribution, we write the DSF in terms of the dielectric function $\varepsilon(q,\omega)$ of the free electrons. As a first step for computing the dielectric function, the free electrons are assumed to act as a uniform electron gas and the interactions are handled within the random phase approximation (RPA), which we implement following Johnson et al. [38]. This RPA approach is a common baseline model of the collective plasmon response in XRTS experiments of warm, dense samples [38, 76, 77, 82, 83].

We can go beyond the RPA-based DSF by using an alternate form for the dielectric function based on the Mermin ansatz [84], which builds upon the RPA dielectric function by including an energy-dependent electron-ion collision frequency $\nu(\omega)$:

$$\varepsilon^{\mathrm{M}}(q,\omega) = 1 + \frac{(\omega + i\nu)[\varepsilon^0(q,\omega+i\nu) - 1]}{\omega + i\nu[\varepsilon^0(q,\omega+i\nu) - 1]/[\varepsilon^0(q,0) - 1]}, \tag{14}$$

where ε^0 is the RPA dielectric function and $\nu = \nu(\omega)$.

The accuracy of the predictions of the free-free portion of XRTS spectra using the Mermin DSF model depends on the choice of the collision frequency model. In work that we are currently writing up for publication in Hentschel et al. [15], we enumerate the various choices that can be made when evaluating the collision frequency. This ranges from the simplest version of dynamic collision frequencies – Born theory for $\nu(\omega)$ using Born scattering cross-sections obtained from a Yukawa-type interaction potential with an ideal density of states (DOS) [5] – to a more complete

and self-consistent picture (denoted as T+) that uses a Lenard-Balescu treatment for $\nu(\omega)$ [73] , T-matrix cross-sections to account for strong collisions in the DFT-AA interaction potential, a fully quantum DOS, and includes inelastic scattering processes based on the total cross section derived from the phase shifts of the DFT-AA model's distorted waves. These advances build on results from the investigations of the static structure processes described in section 2.3. Like those advances, they can be compared with both the independent KG calculations and state-of-the-art calculations from multi-atom codes such as TDDFT (see fig. 2-5 below).

Real-time TDDFT can be used to calculate the dynamic structure factor in a multi-atom framework that goes beyond many of the approximations made in AA. Our particular implementation of real-time TDDFT in a fork of the *Vienna Ab-initio Simulation Package* (VASP) [39–41] was first described in Refs. [81, 85]. In short, the approach calculates the DSF from the electron density's real-time response to a perturbing potential in the linear response regime.

In the course of computing benchmark data with TDDFT, we uncovered an unexpected non-LTE effect related to the geometry of the atoms in the sample. The DSF of isochorically heated aluminum, where electrons are at an elevated temperature while ions remain cold, contains additional features which are absent from the DSF of melted aluminum, where electrons and ions are in thermal equilibrium (see Figure 2-5a). Further investigation revealed that these features arise from the band structure of crystalline aluminum: gaps among high-energy conduction bands lead to a nonideal density of states (see Figure 2-5b), and modulations in the density of states correspond directly to modulations in the DSF. These types of band structure effects could potentially help diagnose ion and electron temperatures simultaneously in XRTS experiments on non-LTE samples. They also suggest future directions for AA development, since AA methods struggle to capture band structure in degenerate matter. We are currently preparing these findings for publication in Kononov and Baczewski [16].

In addition to illustrating the differences in observable signatures between crystalline and liquid aluminum (and highlighting the inability of the spherically symmetric DFT-AA model to capture lattice effects), fig. 2-5 shows the impact of including the dynamic collision frequencies detailed in fig. 2-4 on the observable DSF. In general, the real part of $\nu(\omega)$ will broaden the plasmon peak of the DSF from its RPA expression and the imaginary part will shift it. The significant shift from the RPA in the peak of the DSF evident in fig. 2-5a is a strong indication that neither the transform of the Drude-like $\sigma^{ff}(\omega)$ nor any simple Born approximation for $\nu(\omega)$ can adequately capture the dynamic response of warm dense aluminum. A similar shift in the plasmon was observed experimentally by Sperling et al. [77]. By contrast, both the transform of the KG $\sigma^{cc}(\omega)$ and the T+ inelastic $\nu(\omega)$ give shifts in the plasmon peak that match the TDDFT predictions, with the T+ inelastic $\nu(\omega)$ additionally having more broadening and better agreement with TDDFT. In other cases we have examined, the two approaches to calculating $\nu(\omega)$ are in better agreement.

Future work with the DFT-AA model in this area includes reconciling the various approaches to generating $\nu(\omega)$, clarifying the role of inelastic collisions and lattice effects (both of which could help bring the static conductivities discussed in the previous section into better agreement with reference data at low temperatures) and additional comparisons with both TDDFT and experimental data. We are also exploring the use of Bayesian inference methods for extracting uncertainty bounds for $\nu(\omega)$ from TDDFT DSF data. Inversion of the Mermin DSF to obtain the collision frequency is prone to instabilities, in that multiple $\nu(\omega)$ can yield roughly the same DSF

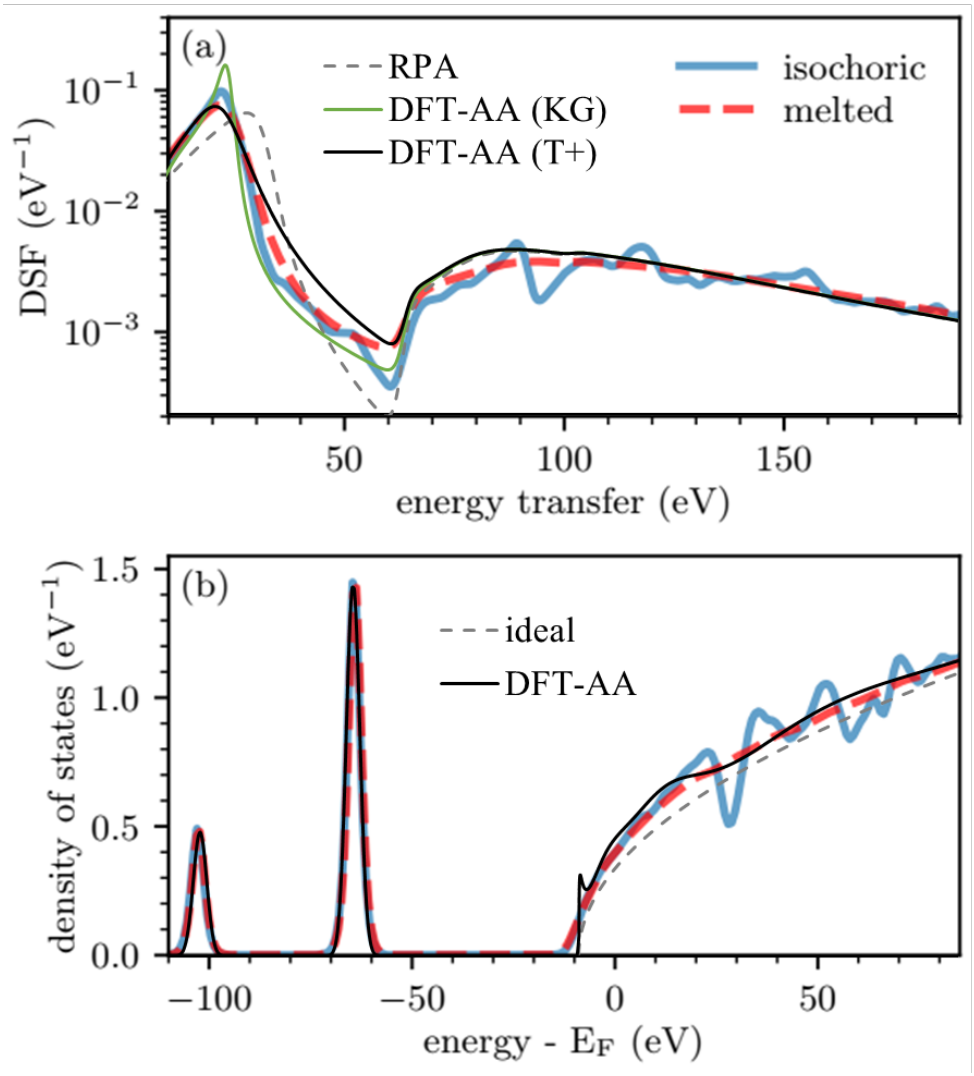

Figure 2-5 (a) Dynamic structure factors at a scattering q of 1.55 Å^{-1} and (b) densities of state for aluminum at solid density and a temperature of 1 eV. The TDDFT curves show crystalline aluminum isochorically heated to an electronic temperature of 1 eV (blue) and melted aluminum in thermal equilibrium at the same temperature (red). The DFT-AA curves in (b) illustrate the good agreement of the fully quantum density of states from the DFT-AA model with the melted multi-atom calculation and highlight both the inability of the DFT-AA model to capture lattice effects and the persistent difference between the quantum and ideal densities of states. In (a), the RPA and DFT-AA curves illustrate the effects of various dynamic collision frequencies (detailed in fig. 2-4) on the Mermin DSFs.

signal. Our technique relies on optimization methods and Markov chain Monte Carlo for finding the distribution of $\nu(\omega)$ for a given set of DSF data, without making restricting assumptions on its form. The resulting $\nu(\omega)$ and uncertainties from this approach can be used to directly validate our collision rate theories and inform the validity of inferences like [77]. Overall, this line of research has been one of the most productive of the LDRD, leading to multiple papers in preparation.

2.5. Stopping Powers

Stopping powers describe how charged particles lose energy as they travel through a plasma environment. They are important for fusion simulations as the primary mechanism by which energy from initial fusion reactions is returned to the fuel. That is, they control the self-heating that can lead to fusion ignition and burn. To calculate stopping, we again turn to the dielectric functions, calculating an energy loss function $\mathrm{Im}\{-1/\varepsilon(q,\omega)\}$ (closely related to the DSF) to describe the retarding force that the target electrons have on the ion projectile. Using the random phase approximation (RPA) for the dielectric function, the stopping power can be analytically approximated for the low and high projectile-velocity limits. This allows for efficient computation of stopping powers, and can be combined with a local density approximation scheme to include density effects determined from the DFT-AA model's $n_e(r)$ [86, 87].

We can also use the Mermin dielectric function to compute stopping powers, incorporating the significant improvements to $\varepsilon(q,\omega)$ described above. However, now there is no analytic form for the stopping numbers, and thus it is not computationally practical to incorporate density effects as above. However, we have found that when only considering the stopping from the free electrons in the target, the Mermin stopping model with accurate collision frequencies has better predictive capabilities than the RPA stopping when validated against TDDFT stopping powers. Figure 2-6 illustrates how the inclusion of accurate collision frequencies (both T+ and KG) gives significant improvements over stopping powers computed with the RPA and more approximate collision-frequency theories, especially below the Bragg peak. We are currently preparing our findings on the effect of electron-ion collisions on dynamic structure factors and stopping powers for publication in Hentschel et al. [15].

We can also use Ehrenfest-TDDFT to calculate stopping powers in a multi-atom framework that goes beyond many of the approximations made in the DFT-AA model. Our particular implementation of Ehrenfest-TDDFT in a fork of the *Vienna Ab-initio Simulation Package* (VASP) [39–41] was first described in Refs. [85, 88]. Stopping powers can be computed from Ehrenfest-TDDFT by analyzing the force induced on a proton projectile by the electrons of a material as it traverses that material with a given velocity. However, the results of this method can depend on the specific path the proton takes through the material [89, 90]. Typically, TDDFT stopping power studies avoid costly averaging over many trajectories by using a random trajectory assumed to be representative of this average.

In the course of generating reliable benchmark stopping data, we developed a more rigorous approach for selecting suitable projectile trajectories, which we are preparing for publication in Kononov et al. [14]. Our method is based on the principle that the projectile should experience a representative distribution of nearest-neighbor distances along its path in order to correctly

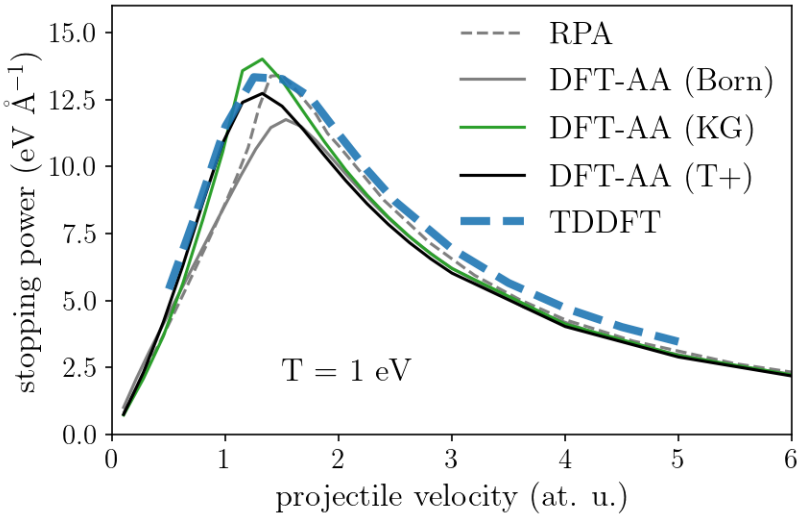

Figure 2-6 Electronic stopping power for aluminum with a density of 2.7 g cm^{-3} and a temperature of 1 eV. The DFT-AA curves illustrate how the inclusion of different kinds of collisions in the Mermin dielectric model can influence the stopping power. In particular, the use of sophisticated collisions with T-matrix collision cross-sections, quantum DOS, and inelastic collisions (black line), or the KG-based collisions (green line) dramatically shifts the Bragg peak from the RPA predictions to yield better agreement with TDDFT for lower projectile velocities. TDDFT calculations use a 3-electron pseudopotential to determine the stopping from the valence electrons.

sample core-electron excitations occurring during close collisions with the host material's ions. Computing a statistical distance between the ideal nearest-neighbor distribution and the nearest-neighbor distribution achieved along a particular trajectory provides a quantitative metric of trajectory quality which can then be optimized to enable more accurate and systematic calculations of average stopping powers with TDDFT.

Future work in this area will explore contributions to the stopping power from bound as well as continuum states. In particular, we will test whether integration of the full DSFs from the DFT-AA model (see Baczewski et al. [12]) capture the high-velocity limit and retain agreement with all-electron TDFFT calculations. We will also continue to investigate the relationship of inelastic collisions (which significantly improved the DFT-AA DSFs and low-velocity stopping powers) to electron-ion equilibration times (see Scullard et al. [91], Dharma-wardana and Perrot [92], Faussurier [93], section 3.2, and Appendix A).

2.6. Radiative Properties

One of the overarching goals of this LDRD was to develop a single model that can provide EOS, transport, and opacity data based on a common set of self-consistent atomic data. This has not been done previously because reaching high accuracy in each material property has been emphasized over ensuring consistency among different material properties. Opacities are a very good example of why accuracy is emphasized: if we use Kubo-Greenwood (Eq. (9)) to generate absorption coefficients or opacities directly from the DFT-AA electronic orbitals, we obtain the dashed lines shown in fig. 2-7. While the bound-free contributions that dominate the spectrum at low and high energies are in reasonable agreement with the detailed-structure SCRAM model [6], described in section 3-1, (which is itself in reasonable agreement with high-resolution experimental data), the bound-bound contributions from DFT-AA-KG are far too averaged. The DFT-AA-KG results would be particularly misleading for calculations of Rosseland mean opacities, which are inverse averages used in radiation transport calculations that emphasize the "windows" between lines.

The hybrid-structure SCRAM model achieves its combined accuracy and relative efficiency by drawing on pre-computed tables of detailed atomic structure and rates for isolated atoms and ions. For each charge state of each element of interest, these databases are generated once (last updated around 2008) using the independent multiconfiguration Dirac-Fock atomic structure code FAC [94]. Detailed structure calculations move beyond the DFT-AA model's single transitions between fictitious one-electron orbitals ($n\ell \rightarrow n'\ell'$) to many transitions among multiple integer-occupied electronic configurations, each of which can have a slightly different energy depending on the configurations of spectator electrons. Because of its detailed structure and resultant spectroscopic accuracy, SCRAM is widely used to help diagnose experimental plasma spectra (e.g. [21]). But at high densities, it must invoke *ad-hoc* modifications to account for plasma density effects such as continuum lowering and pressure ionization – and these modifications do not necessarily capture the complexities of plasma-ion interactions with the same fidelity as the fully self-consistent DFT-AA model.

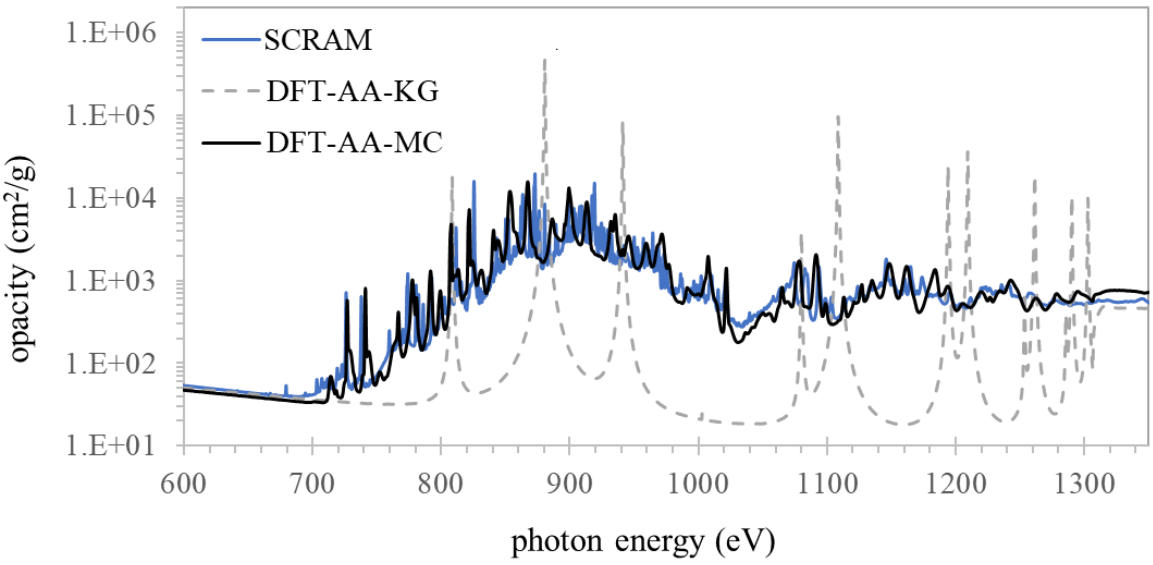

Figure 2-7 Monochromatic LTE opacity of L-shell iron at 0.17 g/cc and $T = 180$ eV from various models. The blue line is from the detailed-structure SCRAM code [6], the dashed gray lines show a straightforward application of Kubo-Greenwood to DFT-AA orbitals, and the black line shows the results of efficiently splitting the DFT-AA electronic structure into multiple electronic configurations using Taylor expansions of Slater coefficients and applying spin-orbit splitting to the calculated spectra.

Extending the DFT-AA model to generate the detailed multiconfiguration (MC) electronic structure necessary for consistent and accurate radiative properties is thus a major challenge. Doing so efficiently – given the consistency requirement that the structure be recomputed from scratch for every temperature and density condition – compounds the challenge.

We move systematically from the highly averaged DFT-AA-KG spectrum to the highly detailed DFT-AA-MC spectrum shown in fig. 2-7 in several steps, each of which accounts for an important effect. First, we enumerate real integer-occupied configurations about the average configuration. Starting with the integer-occupied ground configuration of an ion with a charge close to Z^*, we excite one electron from each occupied bound orbital into all orbitals with vacancies (including the quasibound orbitals described in section 2.1). This gives us a set of singly excited configurations, including (if desired) ones with inner-shell excitations. From each of these new configurations, we repeat the systematic excitation of electrons from occupied states into states with vacancies, avoiding duplicate configurations, to obtain a set of doubly excited states. This process can be iterated as often as desired, although the combinatorics can quickly lead to an intractable number of configurations (see [95]) and so we usually stop at triply excited states and often exclude deep inner-shell transitions.

We then calculate the energies of each of those configurations using stored quantities calculated from the DFT-AA orbitals $P_{n\ell}(r)$. Following Cowan [96], Faussurier and Blancard [97], we set

the configuration-average binding energy of each $i = n\ell$ electron in each $[(n\ell)^N ...]$ configuration to be $E^i = E^i_k + E^i_{nuc} + \sum_{j\neq i} E^{ij}$, the sum of its kinetic energy, its nuclear interaction energy, and its interaction energies with all other electrons in its configuration. The kinetic energies are:

$$E^i_k = \frac{1}{2}\int_0^{R_{WS}} P_i^* \left[-\frac{d^2}{dr} + \frac{\ell_i(\ell_i+1)}{r^2} \right] P_i \, dr, \tag{15}$$

the electron-nuclear potential energies are:

$$E^i_{nuc} = \int_0^{R_{WS}} (-Z_{nuc}/r)|P_i|^2 \, dr, \tag{16}$$

and the interaction potential energies E^{ij} are given in terms of Slater integrals $F^k(ij) = R^k(ij,ij)$ and $G^k(ij) = R^k(ij,ji)$, with the radial integrals

$$R^k(ij,ba) = \int_0^{R_{WS}} \left\{ \frac{1}{r_2^{k+1}} \int_0^{r_2} r_1^k P_i^* P_b dr_1 + r_2^k \int_{r_2}^{R_{WS}} \frac{1}{r_1^{k+1}} P_i^* P_b dr_1 \right\} P_j^* P_a dr_2 \tag{17}$$

$$E^{ij} = F^0(ij) - \frac{1}{2}\sum_k \begin{pmatrix} \ell_i & k & \ell_j \\ 0 & 0 & 0 \end{pmatrix}^2 G^k(ij) \tag{18}$$

The configuration-average total binding energy of each N-electron configuration is $E_c = \sum_i (E^i_k + E^i_{nuc} + \frac{1}{2}\sum_{j\neq i} E^{ij})$. Note that since we restrict the intergrals to the ion sphere, we capture the effects of pressure ionization as states dissolve into the continuum. And since we include the quasibound states in our accounting, we do not risk missing orbitals that may be bound in one ion or configuration and unbound in another. Finally, each configuration is assigned an occupation fraction according to Fermi-Dirac statistics [98, 99], returning an LTE Z^* that is typically falls between Z_f and Z_c from the DFT-AA model. To calculate emission and absorption spectra, we calculate the dipole matrix elements among just the DFT-AA orbitals to obtain oscillator strengths for each $n\ell \rightarrow n'\ell'$ transition. We then assign radiative decay rates with occupation and vacancy factors as we would for a simple screened hydrogenic model [1], but using transition energies and oscillator strengths derived from a fully self-consistent model.

Splitting the DFT-AA model into multiple configurations leads to a profound improvement over the DFT-AA-KG opacities, giving tens to thousands of transitions for each single $n\ell \rightarrow n'\ell'$ transition in the DFT-AA model. While the resulting spectra might be marginally suitable for calculating mean opacities and overall emission envelopes, they remain inadequate for direct comparisons to experiment since they neglect several significant effects including orbital relaxation, relativistic effects, and plasma effects. We systematically address each of these here, with each change to the configuration energies resulting in slight modifications to occupations and significant modifications to the detailed spectra.

A significant deficiency of the simple multiconfiguration model is that it does does not account for how the orbital wavefunctions (and therefore Slater integrals, E^i_k, E^i_{nuc}, E^{ij}, E^i, and E_c)

self-consistently change in response to changes in the electronic configurations. This effect is called orbital relaxation, and the most straightforward way to account for it is to re-optimize the self-consistent orbitals to each configuration, recomputing the energies and Slater integrals for each. But this is computationally daunting, especially for complex ions with many active electrons that may have many thousands of configurations. Instead, we have developed a new approach: after self-convergence is achieved for the DFT-AA model, we systematically move $\Delta N \approx 0.2$ electrons from each highly occupied ($N_k = o(n_k \ell_k) > 1$) bound and quasibound orbital k into the continuum, re-converge the self-consistent field equations on that new configuration, recompute new Slater integrals and energies $a_i = E^i_k + E^i_{nuc}$ and $b_{ij} = E^{ij}$, and define coefficients for a Taylor expansion of the energies under changes Δo_k in each orbital:

$$a'(ik) = \frac{(a_i^{AA} - a_i^{AA-\Delta o_k})}{\Delta o_k} \tag{19}$$

$$b'(ijk) = \frac{(b_{ij}^{AA} - b_{ij}^{AA-\Delta o_k})}{\Delta o_k} \tag{20}$$

This requires only a handful of re-optimizations that do not require particularly stringent convergence and allows us to generate reasonably accurate E_c for any configuration using $a_i = a_i^{AA} + \frac{1}{2}\sum_k a'(ik)\Delta N_k$ and $b_{ij} = b_{ij}^{AA} + \frac{1}{2}\sum_{j,k} b'(ijk)\Delta N_k$. We have tested the accuracy of this approach by verifying that the predicted E_c for a given configuration remains stable even when it is several ionization stages or excitations removed from the reference DFT-AA configuration ($\Delta N > 2$). Including orbital relaxation in this way is extremely efficient and significantly improves the accuracy of the transition energies.

The next improvement in the atomic structure is the inclusion of relativistic effects.Since our DFT-AA model is only semi-relativistic (that is, it includes gross relativistic effects in a Pauli approximation but solves the Schrödinger equation for $n\ell$ orbitals rather than the Dirac equation) it does not produce the major and minor components required for an $n\ell j$ representation. We return to the reference DFT-AA orbitals and compute the spin-orbit interaction:

$$E^i_{so} = \frac{\alpha^2}{2}\int_0^{R_{WS}} \frac{\partial V(r)}{\partial r}|P_i|^2 dr \tag{21}$$

for states with $\ell > 0$, which leads to splitting of the transitions into $j = \ell - \frac{1}{2}$ and $j = \ell + \frac{1}{2}$ components. Before computing the detailed spectra, we statistically weight the occupations and oscillator strengths of each of these components to preserve the total strength of the non-relativistic transitions. Here we also include correlation effects following Cowan [96]. Together, the orbital relaxation, spin-orbit, and correlation modifications to the base multiconfiguration DFT-AA model result in the DFT-AA-MC spectrum shown in fig. 2-7. This spectrum is in quite good agreement with the detailed-structure SCRAM code, despite not including the full configuration interaction effects that SCRAM uses for some of its levels.

Finally, we consider the influence of the plasma potential. Notably, we find that the transition energies predicted by the above calculations are fairly insensitive to the plasma density, even

though $P_{n\ell}(r)$ and the first-order estimates of transition energies as $\delta\varepsilon = \varepsilon_{n\ell} - \varepsilon_{n'\ell'}$ can change significantly at high densities [100]. Faussurier and others propose including an additional term in the configuration energies to account for the plasma potential, $E_p = \sum_i E_p^i$, with

$$E_p^i = \int_0^{R_WS} V_p(r)|P_i|^2 dr \tag{22}$$

with $V_p(r)$ the plasma potential. We have explored both the Massacrier and Dubau [101] approximation for the plasma potential used by Faussurier and Blancard [97] and variations of the external potential described in section 2.1. These can both lead to the plasma polarization shifts [102] that have been observed in dense plasmas [100, 103, 104] by estimating the density-dependent shifts in transition energies obtained as simple differences in orbital binding energies [100, 103]. We have also developed a self-consistent variational approach to describing these shifts (described in section 2.8 below), which adds yet another re-convergence loop to calculate self-consistent binding energies in the absence of the free electrons, providing the zero-density limit of DFT-AA transition energies in their reference configuration.

However, in comparisons with state-of-the-art line shape calculations, it appears that line shifts may be primarily due to the dynamic response of electron-electron collisions (reminiscent of the plasmon red shifts described in section 2.4, while the plasma potential is primarily responsible only for ion-Stark broadening (see section 2.8. This remains an area of active study. Additional future work will explore whether the configuration-interaction (CI) effects that are essential for spectroscopic accuracy in closed-shell ions (He-like, Ne-like...) and adequate treatments of metastable states can be approximated at the level of the average atom. If so, we will also explore whether CI effects with the continuum can be reasonably included, addressing a longstanding problem for atoms in plasmas. We will also explore lumping high-n orbitals together to form superconfigurations [105], partially resolved transition arrays [106], and the application of a convergence criterion that will signal when additional excitations are negligible.

2.7. Non-Equilibrium Average Atom

So far, all of our reported results have assumed local thermodynamic equilibrium (LTE), where detailed balance among collisional and radiative upward and downward rates enforces Fermi-Dirac statistics for level populations. With few exceptions (Lokke and Grasberger [107], Faussurier et al. [108]), LTE is a standard assumption for AA and DFT-based models. A key goal of this LDRD was to develop not only an internally consistent DFT-AA model suitable for tabulation of a complete set of relatively accurate material properties, but to extend that model to non-LTE plasma conditions, where downward spontaneous radiative rates dwarf photoexcitation and photoioniztion in weak radiation fields (see Chapter 3).

Given the set of configurations, photionization cross sections, and oscillator strengths described in section 2.6, it is relatively straightforward (though not computationally trivial) to generate and solve a collisional-radiative (CR) rate matrix to obtain non-LTE configuration occupations. However, the LTE Z^* can be very far (tens of charge states) from the non-LTE Z^* for low densities, high temperatures, and high Z_{nuc}. And since configuration energies, cross sections, and

oscillator strengths (and thus the CR rate matrix) depend on the initial DFT-AA ionization stage and $P_{n\ell}$ orbitals, we need at least a rough approximation to the full non-LTE solution to provide a reasonable estimate for the initial non-LTE electronic states. This first estimate of the non-LTE DFT-AA model does not have to be particularly accurate, since the Taylor expansion of configuration energies for the DFT-AA-MC model is fairly robust to variations of a few charge states, but it has to be cheap, since the DFT-AA-MC calculations are relatively expensive and we do not wish to do them more than once.

Comparing the Saha-Boltzmann statistics used to establish LTE in chemical models to the Fermi-Dirac statistics used to populate the LTE configurations of the DFT-AA model [98, 99], we note that detailed balance of ionization and recombination rates $R^{ion}_{Z^*\rightarrow Z^*+1}$ and $R^{rec}_{Z^*+1\rightarrow Z^*}$ enforce LTE ratios between the populations X^{Z^*} and X^{Z^*+1} of the ground configurations of adjacent charge states:

$$\frac{X^{Z^*+1}}{X^{Z^*}} = \frac{R^{ion}_{Z^*\rightarrow Z^*+1}}{R^{rec}_{Z^*+1\rightarrow Z^*}} = \mathrm{e}^{(\Delta\varepsilon-\mu)/\tau} \tag{23}$$

with $\Delta\varepsilon = \varepsilon_{Z^*} - \varepsilon_{Z^*+1}$, or, for ionization of a particular bound $n\ell$ electron, $\Delta\varepsilon = \varepsilon_{n\ell}$, and where we have assumed that X^{Z^*} and X^{Z^*+1} have equal statistical weights. We thus propose replacing the Fermi-Dirac occupation factor used to populate the $n\ell$ orbitals of the DFT-AA model as follows:

$$f^{\text{LTE}}(\varepsilon_{n\ell}) = \frac{1}{1+\mathrm{e}^{(\varepsilon_{n\ell}-\mu)/\tau}} \rightarrow f^{\text{non-LTE}}(\varepsilon_{n\ell}) = \frac{1}{1+R^{ion}_{n\ell}/R^{rec}_{n\ell}} \tag{24}$$

with $R^{ion}_{n\ell}$ and $R^{rec}_{n\ell}$ calculated using (for now) very simple hydrogenic approximations for the collisional and radiative ionization and recombination rates to and from a given shell. Dielectronic recombination (d.r) and excitation autoionization (a.i) are much more difficult to estimate in the one-electron-orbital picture of the DFT-AA model (see [108]), and we have not yet found a simple way to estimate their impact on the proposed non-LTE occupation factor. Figure 2-8 shows that this simple substitution gives very good agreement with the screened hydrogenic [1] collisional-radiative (CR) model when d.r. and a.i. processes are excluded and reasonable agreement even with the full CR model. And it is no more expensive to run than the LTE DFT-AA model. It thus provides a good-enough starting point for full collisional-radiative non-LTE calculations based on the configurations and rates from the DFT-AA-MC extension. Once the full CR occupations are computed, the equivalent AA shell occupations $o_{n\ell}$ can be enforced in a final calculations of self-consistent electron orbitals and potentials for the DFT-AA model, and every EOS and transport property described above can be generated for a non-LTE plasma with the same accuracy and internal consistency that we have achieved for the standard LTE DFT-AA model.

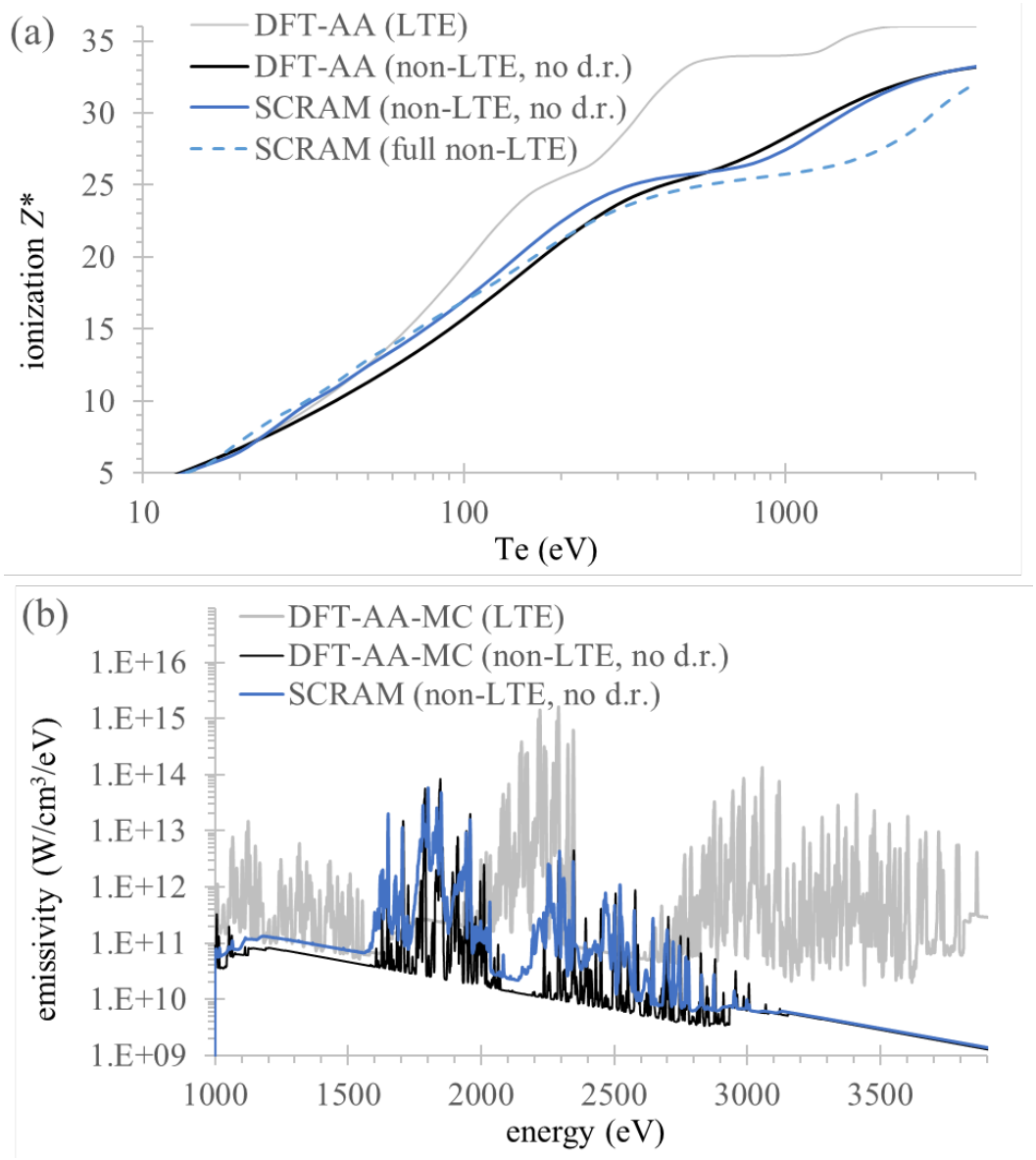

Figure 2-8 (a) Average ionization Z^* of krypton at $\rho = 0.01$ g/cc from various models. The LTE values are given in light gray (and are nearly identical for the collisional-radiative model SCRAM and the DFT-AA model. Modifying the Fermi-Dirac occupation factor as described in the text brings the DFT-AA model into good agreement with SCRAM without dielectronic recombination (d.r.). SCRAM with d.r. has lower ionization. (b) the L-shell emissivity of Kr at $\rho = 0.01$ g/cc and $T_e = 500$ eV from various models. The LTE emission differs profoundly from the two non-LTE models, which are in reasonable agreement with each other.

2.8. Line shapes

Emission and absorption spectra are key observables in high energy density experiments and critical data for radiation-hydrodynamic simulations. Calculations of these spectra require not only the energy-level structure and occupations of electronic configurations (as discussed above) but also line shapes – that is, an understanding of how the photons from each transition are distributed in energy about their central transition energy E^0. In isolated atoms, emission lines are broadened by the uncertainty principle: since energy and time are conjugate variables, $\delta E \delta t \geq h/4\pi$ and long-lived excited states with high uncertainty in their lifetimes can have very narrow emission profiles, while the line shapes of transitions from excited states with fast decay rates are much broader to compensate for low uncertainty in their lifetimes. In HEDP, the plasma environment can introduce additional broadening. Very roughly, this broadening originates from a few key sources:

1. Doppler effects from the thermal motion of the ions leads to Gaussian broadening of lines with $fwhm \approx 5 \times 10^{-5} E^0 (T_i/Z_{nuc})^{1/2}$ eV (with T_i and E^0 in eV). With photon energy $E = h\nu$ and line-center frequency ν_0, Doppler-broadened line profiles are: $\phi_D(\nu) = \frac{1}{\nu_D\sqrt{\pi}} e^{-[(\nu-\nu_0)/\nu_D]^2}$, with $fwhm = \nu_D\sqrt{\ln(2)}$.

2. Fast electron-ion collisions decrease excited-state lifetimes, increasing the uncertainty in the transition energy and broadening line shapes: $fwhm \approx 15/(T_e)^{1/2}(n_e/10^{22})$ eV (with T_e in eV and n_e in e/cm^3; very approximate). Lorentzian line profiles are: $\phi_L(\nu) = \frac{\nu_L}{\pi}[(\nu-\nu_0)^2 + \nu_L^2]^{-1}$, with $fwhm = 2\nu_L$ and $\nu_L = \sum \text{rates}/4\pi$.

3. Static electric microfields caused by neighboring ions can induce shifts in the electronic structure that lead to shifts in transition energies; the resulting broadening for transitions with even Δn is $fwhm \approx 4.3 n^2/Z_{nuc}(n_e/10^{22})^{0.58}$ eV (with n_e in e/cm^3). Ion-Stark line profiles are sometimes approximated as Voigt convolutions with a Holztmark distribution of Gaussian and Lorentzian widths, but accurate models predict splitting that cannot be captured with simple line profiles.

These sensitivities of line shapes to the plasma environment make them a key diagnostic in experimental plasma spectroscopy: line shapes encode a wealth of information about the local conditions of the plasmas that produce them, including electron densities, electron and ion temperatures, turbulent and bulk motion, and electric and magnetic fields. Line shapes are also significant for radiation transport, since broader lines close the low-opacity "windows" in the absorption spectrum that largely determine the Rosseland mean opacity.

This LDRD supported significant research in the development of spectral line shape theory along two lines. First, we made significant improvements to a standard line-shape code to include more fundamental physics, resulting in four publications (including three PRLs): Gomez et al. [8, 9, 10], Kraus et al. [18]. Next, we developed a new approach for ion-Stark broadening that uses the output of the DFT-AA model to predict both electronic structure shifts and electric microfields, ensuring internal consistency. These advances are described in the sections below.

2.8.1. Balrog: an improved standard model

At their core, spectral line shape calculations compute the perturbation of a plasma environment on the electronic structure of atoms and ions and then average over that perturbation. Unperturbed (isolated) atoms have sharp, narrow lines at their fundamental transition energy, E^0, that are broadened according to the uncertainty principle into line shapes with Lorentzian profiles. Embedded in plasmas, additional perturbations broaden these lines and they take a non-trivial shape that can no longer be approximated by the usual Lorentzian prescription.

Standard line shape calculations use multiple – and often untested – approximations. These approximations are necessary because of the complexity and breadth of the physical processes involved. To perform accurate line-shape calculations, one needs to understand atomic structure and spectra, atomic collisions, plasma physics, electric and magnetic field perturbations, and statistical mechanics. Thus, no line-shape model captures all of the physics exactly. However, we can probe the importance of some bits of physics to evaluate their importance. For example, Gomez et al. [109] evaluated how important the plasma statistical nature is to the line shape; Gomez et al. [8] reviewed many of the approximations used by line shapes and their validity; and Kraus et al. [18] has shown that removing these approximations has significant impact on our ability to determine plasma properties.

One of the most common approximations in the the field of spectral line shapes is that the perturbing plasma particles can be treated as classical quasi-particles. This approximation is extremely common and allows researchers to test different types of physics that can't be tested otherwise, e.g. plasma screening [110]. It had been the conventional thinking that a classical treatment and a quantum treatment of the plasma particles resulted in the same line shapes [111].

In the conventional method of calculating line shapes, radiationless recombination channels such as dielectronic recombination have generally been neglected as unimportant [112, 113]. But, when we examined them, we found that they are important for a long-standing discrepancy in the measured and modeled widths of isolated lines. Including these recombination channels in the calculation reduced the theory-experiment discrepancy in the line shape; this work was published by Gomez et al. [9].

While the work of Gomez et al. [9] was significant in establishing the importance of a quantum treatment of the plasma electrons, a significant deficiency remained: the second-order approximation. The second-order approximation uses an expansion method to describe the time evolution of the atomic system. Accurate evaluation of the time evolution is important, and it having the property of unitarity (conservation of probability) is also important, but the second-order approximation does *not* preserve the unitarity property. Therefore, to have full confidence in quantum line shapes, we needed to address the unitarity problem. With the help of some external collaborators from Los Alamos National Laboratory, we were able to adopt the method of Bray and Stelbovics [114] to fix the non-unitarity problem in the line shape. We published our results in Gomez et al. [10].

This fundamental research into spectral line broadening has also sparked ongoing research into fundamental questions about the integrated opacity of a total system (ion + plasma). Sum rules

state that the total integrated opacity of a system of electrons is equal to the number of electrons in that system. In isolated atomic systems, the integrated opacity should be equal to the number of bound electrons in that atom. However, in a plasma, these atomic systems are *not* isolated, and we must therefore include the effects of complex configuration interaction with the free (plasma) electrons that go beyond the perturbations so far considered. These interactions may alter the expected sum rule, especially for highly charged ions like the transition metals ionized to L-shell ions in the opacity experiments on Z machine [115]. A preprint of this work [116] is available for review.

2.8.2. Test Shape: a new approach to ion-Stark broadening

As noted above, standard line shape theory for has many challenges. Among them are 1) the computational expense of perturbation theory and complete all-order quantum collisions when applied to many-electron systems and 2) the difficulty of consistently combining atomic and plasma models. In the spirit of this LDRD, which emphasises computational efficiency and internal consistency and relies on guidance from the most sophisticated existing models, we have developed a new approach to calculating ion-Stark broadening using quantities derived from the self-consistent DFT-AA model.

Ion-Stark broadening is among the most challenging aspect of line shape theory: First, it requires calculating perturbed electronic structure for many values of external electric fields, which becomes prohibitively expensive for ions with three or more active electrons. It is also among the least consistent aspect of line shape calculations, since it requires a separate calculation of the ion microfield distribution; these are usually provided by models that use approximate screening based on input plasma density and perturber and radiator ion charges. Once both the atomic-physics and plasma-field effects are calculated, the field-dependent shifts of each component of each transition are foled with the electric field distribution and summed to provide a line profile.

As opposed to the traditional method of folding the electric field probability distribution from an external source like APEX [117] with field-dependent transition energies from perturbation theory, our new method posits that we can instead directly fold a nearest-neighbor radial probability distribution $P_{NN}(r)$ with radially dependent line shifts, using transition energies, energy shifts, and radial density distributions from a single model, DFT-AA, which has the same computational efficiency for ions of any complexity.

The atomic data needed for line-shape calculations is generated by the DFT-AA model in the following way. First, the standard self-consistent loop is performed, ensuring consistency between the screened electronic potential and the electron density of the statistically occupied quantum mechanical orbitals it supports. This produces a set of orbitals (1s, 2s, 2p... $n\ell$) with binding energies $\varepsilon^{p}_{n\ell}$ that change under changes in the plasma conditions. Next, we perform a second self-consistent loop, holding the bound-state occupations fixed at their plasma values but removing the screening due to the continuum (plasma) electrons. This provides a second set of binding energies, $\varepsilon^{0}_{n\ell}$ that represent the average-ion structure of an isolated system with the same ion charge and internal electronic distribution. For any $n\ell \rightarrow n'\ell'$ transition, we set the

isolated-atom transition energy to be $E^0_{n\ell\to n'\ell'} = \varepsilon^0_{n\ell} - \varepsilon^0_{n'\ell'}$ and the plasma-perturbed transition energy to be $E^p_{n\ell\to n'\ell'} = \varepsilon^p_{n\ell} - \varepsilon^p_{n'\ell'}$. Removing subscripts for simplicity, the plasma-induced shift of any line is thus $\Delta E = E^p - E^0$. Early investigations showed that, to a fair approximation, these shifts follow a simple functional form: $\Delta E = C/r^2$, with $C = (E^p - E^0)R^2_{WS}$ a transition-dependent coefficient calculated at the plasma density (characterized by R_{WS}) and r the distance of the nucleus to the nearest-neighbor ion (in the muffin-tin approximation of the DFT-AA model, where the ion distribution is a step function, $r = R_{WS}$). While C varies by a few percent depending on the density (or R_{WS}) at which it is calculated, determining C at the density of interest for each case ensures that the shift will be locally accurate. [9]

Note that the above procedure is quite different from the standard approach of applying perturbation theory to an isolated atom in the presence of an external electric field. However, we can relate the strength of the field at the center of the radiating ion in the DFT-AA model to the equivalent electric field strength used in the perturbation-theory approach. For unscreened ions with charge $Z^* = Z_b$, the Coulombic electric field is $\mathrm{E}^C(r) = Z^*/r^2$. For ions screened with a Debye parameter $k_D = \omega_p/(\tau^2 + \varepsilon_F^2)^{1/2}$, the screened Yukawa electric field is $\mathrm{E}^Y(r) = Z^*(1+kr)e^{-kr}/r^2$. We can thus define new coefficients $C^C_{\mathrm{E}} = C/Z^*$ and $C^Y_{\mathrm{E}} = C/[Z^*(1+kR_{WS})e^{-kR_{WS}}]$ that imply locally linear transition energy shifts in terms of the electric field: $\Delta E = C_{\mathrm{E}}\mathrm{E}$; these can be directly compared to the predictions of the standard perturbation theory models.

Figure 2-9 shows calculations of the energy shifts in the K-shell transitions of H-like (red) and He-like (blue) aluminum as a function of the electric microfield. The standard perturbation theory results are given by thin solid lines, showing that detailed atomic models for these ions predict splitting into multiple components that is roughly linear with the electric field strength above about 1 au for the α lines, 0.3 au for β, and 0.1 au for γ. In the linear regime, the red-shifted and blue-shifted components are symmetric to a few % in both H-like and He-like ions. The fractional oscillator strengths of each component, listed on the figure, allow us to find a weighted average of linear-fit coefficients C^{PT}_{E} from the standard perturbation-theory method. These linearized and averaged fits, given by heavy blue and red solid lines in the figure, agree to within a few % for H- and He-like ions and can be directly compared to the C^Y_{E} linear-fit predictions of the DFT-AA model (heavy black solid lines). Given the significant differences in the physical underpinnings and code implementations of the two approaches, the agreement is quite good: our C^Y_{E} matches $\langle C^{PT}_{\mathrm{E}} \rangle$ within the expected variations of the C^Y_{E} coefficients under different temperature and density conditions and much smaller than the variations among C^{PT}_{E} components in the standard model. While the DFT-AA model predicts only red shifts, here it has been reflected to provide a blue-shifted component as well. The worst agreement is seen for the He-like $2p-1s$ (He_α) transition, where configuration interaction effects dominate over the external field effects at small field strengths. However, the α lines are not typically used for diagnostics and we accept this as a known error.

[9] Initially, we examined just the transition energies from DFT-AA calculations performed at different densities. We found that the transition energies were best described by a power-law fit with transition-dependent coefficients and offsets. We identified the offsets as the zero-density (aka: zero E-field) transition energies and that the power law suggested an inverse square relationship between the energy shift and the density-dependent Wigner-Seitz radius. The coefficients were unique to each transition within each charge state and varied up to 20% with variations in the density.

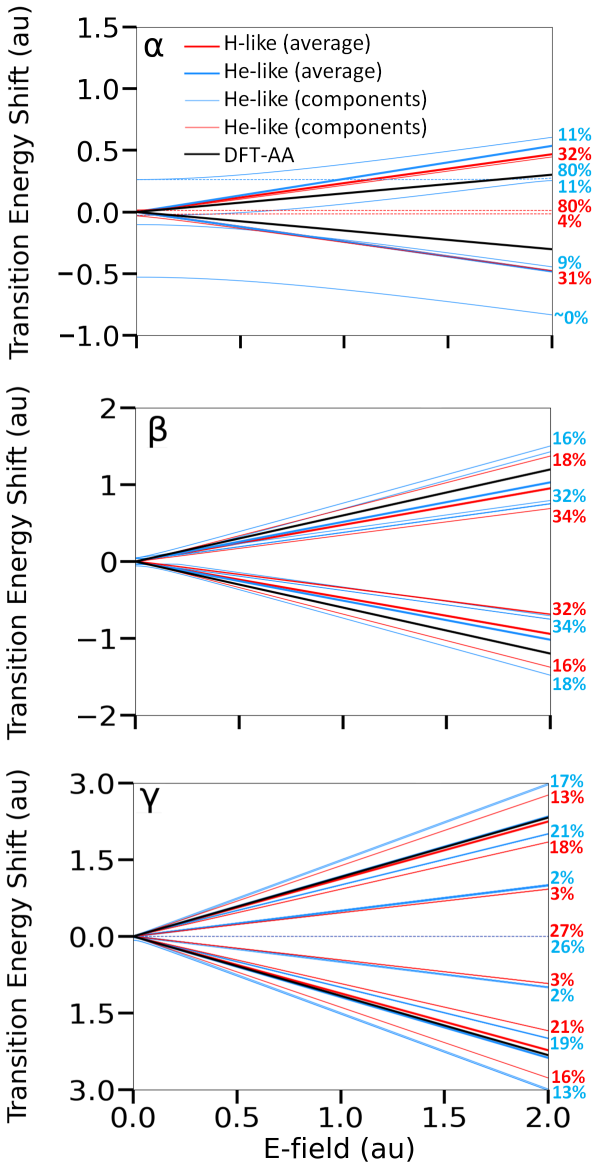

Figure 2-9 Line shifts (in au) from perturbation-theory calculations of H-like (red) and He-like (blue) aluminum in strong electric fields. The $2p-1s$ (α) transitions are at the top, $3p-1s$(β) in the center, and $4p-1s$(γ) at the bottom. Fractional oscillator strengths are listed for each component type (light lines) and the linearized, oscillator-strength-weighted average shifts shown (bold lines). The DFT-AA model prediction for the nearest-neighbor shifts translated to a Yukawa electric field are given by black lines.

With these encouraging results for the atomic-physics part of the line shape problem in hand, we turn to the plasma-physics component: the determination of the electric field distribution. Here, we use the self-consistent radial distribution function $g(r)$ derived from the DFT-AA code and described above in section 2.1 to generate a nearest-neighbor probability distribution function, $P_{NN}(r) = 4\pi n_i r^2 g(r) \exp[\int_0^{r'} 4\pi n_i r'^2 g(r') dr']$. These are illustrated in fig. 2-10(a) for aluminum at T_e=250eV and mass density 0.1 g/cm^3 ($n_e = 2.4 \times 10^{22} e/cm^3$), which has $k = 0.072$(au). Again, we can use the Yukawa relationship between the nearest-neighbor distance r and the electric field E to translate $P_{NN}(r)$ to an electric field probability distribution $P^Y(\mathrm{E}) = P_{NN}(r)(d\mathrm{E}/dr)$ vs. $\mathrm{E}^Y(r)$. A comparison of this electric field distribution against the $P(\mathrm{E})$ calculated by APEX [117] for the same electron density and temperature is shown in fig. 2-10(b). Here, we fixed the charge of both the perturbing and radiating ions to be 11 for He-like Al, while the background ion charge Z_b from the average-atom model at these conditions was 10.64 and the continuum charge Z_C was 11.25. The agreement is quite reasonable; on par with the few-percent agreement we found in the atomic-physics part of the calculation, with the most pronounced disagreements occurring at small fields.

Figure 2-10(c) shows the He-like $3p-1s$ (He_β) lineshapes that result from averaging various field-dependent shifts over electric field distributions, as well as our new approach of folding the radially dependent shifts with the nearest-neighbor distribution $PNN(r)$ (black line). The blue line shows the full calculation of the (unlinearized and unaveraged) perturbation-theory components with the standard (APEX) electric field distribution. [10] The simplified field-dependent line profiles (given by dashed lines) are $\phi(\Delta E) = P(\mathrm{E})(d\mathrm{E}/d\Delta E)$: the dashed blues line shows the average perturbation-theory He-like coefficient folded with the APEX $P(\mathrm{E})$, and the dashed black line shows the DFT-AA coefficient folded with the DFT-AA $P(\mathrm{E})$ (both of which translate the radial nearest-neighbor dependencies into electric field dependencies using the Yukawa potential).

At the relatively low electric fields (less than about 0.2 au) present in this plasma, the He_β-line components retain some individual character and are not fully linear, leading to the asymmetry and red-side structure evident in the full calculation. Retaining the APEX electric field distribution, but linearizing and using the weighted average perturbation-theory coefficients, recovers the blue-shifted component of the line reasonably well but washes out the red-side structure. Replacing the linearized and averaged coefficients and the field distribution from the standard theory with quantities derived *solely* from the DFT-AA model leads to a very small change in the line shape: modestly transferring strength away from line center due to the low-field differences in $P(\mathrm{E})$ low-field/shift regions. This indicates that our DFT-AA approach does a rather good job of capturing both the averaged atomic and the plasma effects that contribute to ion-Stark broadening in the standard theory: that is, the agreement of TestShape with standard models is no accident. Finally, removing the intermediate step of translating the radially dependent DFT-AA quantities into field-dependent quantities also has a relatively small effect –

[10] The standard perturbation-theory + APEX ion-Stark calculations were done specifically for this test of the ion-Stark broadening effects by minimizing the contributions of electron-ion collisions. A full calculation including electron collisions has additional broadening and, notably, a significant redshift. We are actively investigating whether complete and self-consistent dynamic collisions, as described for the continuum-continuum processes in section 2.4, can account for this redshift or if it is more accurate to invoke a plasma potential as described at the end of section 2.6

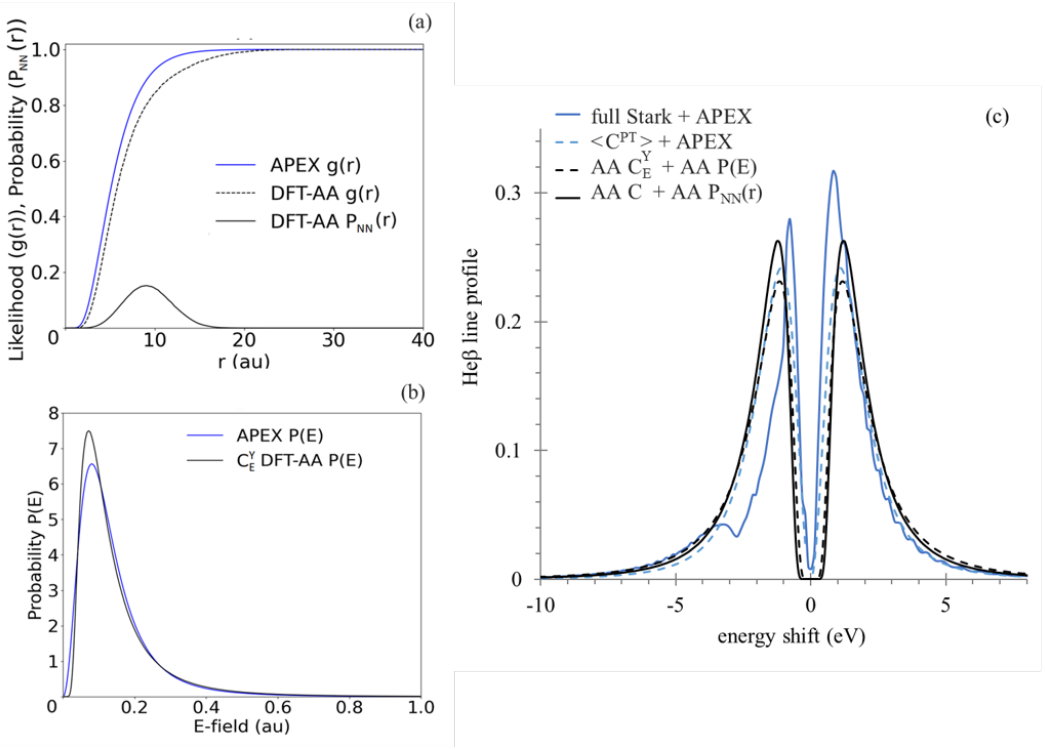

Figure 2-10 (a) Radial ion distribution functions from DFT-AA and the line-shape-standard model APEX for aluminum at $T_e = 250$ eV and $\rho = 0.1$ g/cc, along with the derived nearest-neighbor probability $P(r)$ from the DFT-AA curve. (b) Electric field distributions for the same plasma from DFT-AA and APEX. (c) Al He$_\beta$ line profiles using: component-resolved perturbation theory and APEX $P(\mathbf{E})$ (solid blue); the linearized and weighted-average coefficient from perturbation theory with the APEX $P(\mathbf{E})$ (dashed blue); DFT-AA coefficient $C_{\mathbf{E}}^Y$ and the $P(\mathbf{E})$ derived from DFT-AA (dashed black); and, finally, the DFT-AA radial shift coefficients folded with the DFT-AA $P_{NN}(r)$ (solid black).

and removes any dependence on the assumed functional form of the electric field and screening, returning the model to full internal consistency.

While the averaging of either the standard theory or the DFT-AA approach leads to some significant disagreement in the red-shifted component of the Al He_β line at the given conditions, it offers a real improvement over many other approximate methods. For example, the collisional-radiative models described in section 3.1 use the *fwhm* approximation for ion-Stark broadening given above, folding that width into a Voigt line profile that does not recover central splitting. Here, that approximation gives a Stark *fwhm* $\approx$ 5 eV, which is fairly close to the 4.5 eV *fwhm* of TestShape. And while the statistical approximation will be even worse for the α lines, we expect it to be quite good for the high-*n* lines often used for plasma diagnostics. We also expect it to be more reliable at higher densities, where electric fields are higher and the non-linear low-field behavior of the shifts is less important. Finally, some of the details of the disagreement will be washed out by electron-collisional broadening, which here will convolve the ion-Stark line shapes with a Lorentzian characterized with a *fwhm* of about 2 eV.

Finally, we emphasize that 1) our new approach removes some of the potential inconsistencies between the atomic and plasma physics components of the standard approach to ion-Stark broadening and 2) will be dramatically faster for complex ions with multiple active electrons. It may be able to give reasonable approximations for L- and M-shell transitions that have largely been beyond the reach of standard theory. We plan to write up these results for publication in Adler et al. [17].

The known errors in this approach include the statistical average over detailed components, the lack of discrimination between ions in the coefficients *C*, and the use of averaged ions to determine the nearest neighbor distributions. Future work will explore whether we can impose a second-order broadening to account for the components and will include more extensive comparisons of our model against Balrog and other codes for other elements, plasma conditions, and transition types – including the L-shell transitions that are critical for describing the opacity experiments underway on Z and NIF. We are also interested in rigorously exploring the connections between the dynamic collision frequencies described above in section 2.4 and the standard approaches to line broadening –and line shifts – from fast electron-ion collisions.

3. NON-LTE TABLES AND R-MHD IMPLEMENTATION

In this Section, we give a brief overview of non-LTE modeling and the specific models used in this work, describe the challenges of tabulating non-LTE data and our physics-informed approach to tabulation and interpolation, and describe our initial implementation of non-LTE tables in the radiation-magnetohydrodynamics code GORGON.

3.1. Non-LTE Atomic Models

Occupations (or populations) of electronic configurations (or states) are fundamental quantities in the atomic models used to describe material properties. EOS quantities such as internal energies and pressures are derived from the distribution of population among bound-electron configurations and the number of ionized free electrons, Z^*. Transport quantities depend on the number of free-electron charge carriers and the bound-electron screening that determines momentum-scattering cross sections. Radiative properties are directly dependent on the populations of initial states from which, for example, radiative decay or photoionization processes lead to emission or absorption of photons.

In local thermodynamic equilibrium (LTE), the populations of electronic states follow relatively simple statistical relationships that are established by detailed balance among direct and reverse rates. These statistical relationships depend only on the electronic structure of the ions under consideration and the temperature and density of the plasma. For LTE to hold, the electron, ion, and radiation temperatures should all be equal ($T_e = T_{ion} = T_r$) and their energy distributions should be in thermal equilibrium (Fermi-Dirac, Maxwellian, or Planckian). LTE can also be established at high densities where collisional rates dominate over radiative rates: roughly $n_e \gg 10^{18} T_e^{1/2} Z^6$ cm^{-3} for K-shell transitions in ions with nuclear charge Z and temperature T_e (in eV). For high-Z elements at temperatures large enough to support K-shell radiation, strong spontaneous radiative decay rates enforce LTE only at prohibitively high densities or radiation fields. Most of the high-Z plasmas encountered on Sandia's Z Machine for RES sources and for ICF diagnostics have electron densities below 10^{23} cm^{-3} and $T_r \ll T_e$ – that is, the vast majority of high-Z REHEDS plasmas are highly non-LTE.

When the simple statistical relationships of LTE cannot be used to determine the populations X_i of electronic states i, one has to explicitly calculate and solve a set of coupled collisional-radiative (CR) rate equations: $dX_i/dt = X_i \sum_j R_{i\to j} + \sum_j X_j R_{j\to i}$, where $R_{i\to j}$ represents all possible rates from state i to state j. These rates can be spontaneous, like radiative decay A^r, collisional, like electron-impact excitation and ionization, or driven by photons. The CR rates depend on both the electronic structure of the ions under consideration, which determines the cross sections σ_{ij} of various processes, and the plasma conditions ($T_e, n_e, T_r ...$), or more generally the energy distribution functions F_x of electrons and photons: $R = n_x \langle \sigma_{ij} F_x \rangle$. Different CR models make a variety of choices for the sets of states and the calculations of rates, which can lead to significant variations in their predictions of material properties (see Hansen et al. [118] and references therein).

In this work, we consider three distinct CR models: The reference model is SCRAM [6], an established model suitable for direct comparison with experimental spectra that uses hybrid electronic structure encompassing fine-structure levels, configuration-averaged states, and superconfigurations. A related model is SCFS, a screened-hydrogenic superconfiguration model that closely resembles the DCA inline model [1] used for non-LTE calculations in the radiation-hydrodynamic codes LASNEX and HYDRA. These models use isolated-ion atomic data for electronic states and cross sections, *ad-hoc* density effects, and can incorporate a wide variety of electron and photon distributions. The final model we consider is the DFT-AA model described in Section 2.7, which uses self-consistent atomic data that natively incorporates density effects but

which, for now, is restricted to thermal electron and photon distributions and uses a modification of the Fermi occupation factors to approximate non-LTE effects rather than a full CR matrix.

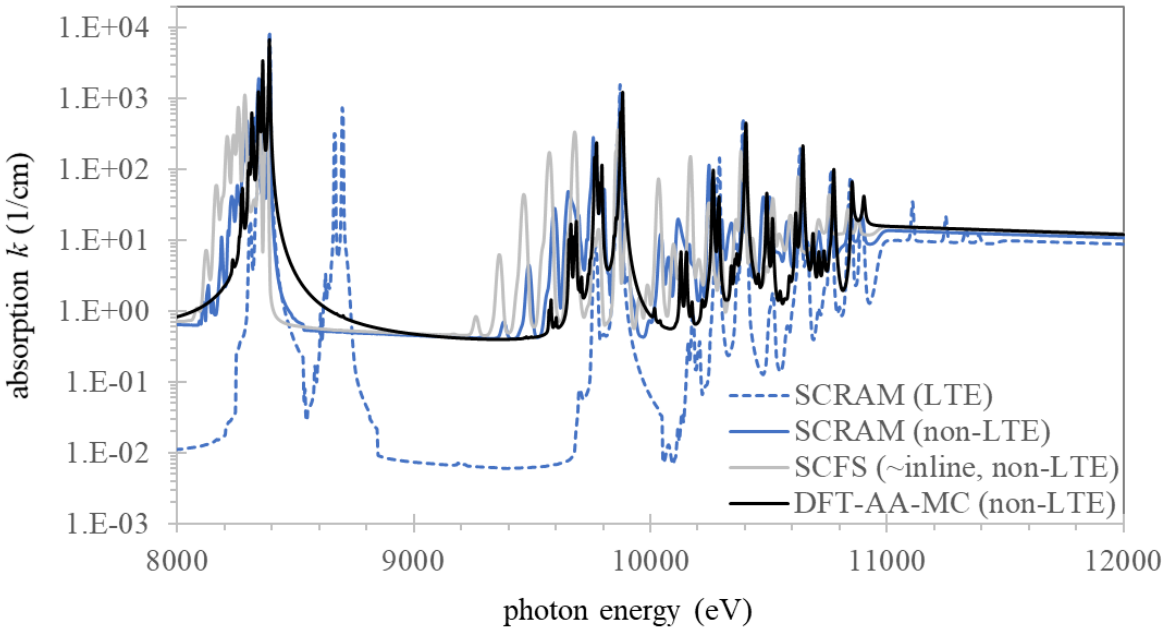

Figure 3-1 Monochromatic absorption spectra from LTE (dashed) and non-LTE (solid) calculations from various models for Cu at T_e = 1 keV and 0.1 g/cm^3. While the three independent non-LTE models have significant variation in charge states and detailed absorption features, those variations are dwarfed by differences between LTE and non-LTE.

Figure 3-1 shows a comparison of detailed K-shell absorption spectra from our three non-LTE models for copper (Z = 29) at T_e = 1 keV and a mass density of 0.1 g/cm^3 (n_e $2.5 \times 10^{22} e/\text{cm}^{-3}$). The profound difference between the LTE curve (dashed) and the non-LTE curves (solid) underscores the order-of-magnitude effect of non-LTE modeling. Here, the non-LTE calculations retain significant population in L-shell charge states (Li-like, Be-like, etc.) that contribute to a robust continuum support for the K-shell lines. In LTE, most of that population shifts to the He- and H-like K-shell ions, dropping the continuum dramatically and generating a strong new H-like absorption feature around 8.7 keV. In LTE, the Rosseland mean (weighted inverse) opacity is 30 times smaller than in non-LTE, and the total LTE emissivity (not shown here, but see fig. 2-8) is about five times larger than that of non-LTE (and more than 100 times larger above the K-edge). By contrast, the differences here among non-LTE calculations are only on the order of 10% for the bulk radiative properties (even though d.r. is excluded in the DFT-AA-MC model and included in the two other models). Note that DFT-AA-MC is significantly closer to our reference model (SCRAM) than is the simple screened hydrogenic model SCSF, which is representative of the model quality available for inline non-LTE calculations. For more complex ions, the differences

among non-LTE models can be significantly larger (factors of 2 - 10) – but the differences between LTE and non-LTE calculations also become more profound. This guides our tabular non-LTE development: if non-LTE tables can reproduce the bulk radiative properties of our best non-LTE models to about a factor of two, they will have similar accuracy to inline non-LTE – but will be much faster – and will offer an enormous increase in accuracy over LTE tables.

3.2. Non-LTE Tables

In LTE, the populations of electronic states and the ionization Z^* depend only on the local temperature and density. Thus tabulation of material properties is straightforward: typical LTE tables have about ten points per decade in temperature and density, spanning temperature ranges from 0.02 eV (approximately room temperature) to 20 keV (fusion ignition temperature) and density ranges from 10^{19} cm^{-3} (atmospheric density) through 10^{23} cm^{-3} (solid density) to 10^{26} cm^{-3} (inertial fusion density) with about $60 \times 70 = 4200$ points. Fore each of these temperature-density points, EOS and transport tables report a handful of properties, while monochromatic (detailed) opacity tables report absorption coefficients $k(\nu)$ on about 10^4 photon energies ($h\nu$) to enable resolution of details like photionization thresholds and bound-bound transitions. In LTE, the emissivity j and absorption coefficients k are simply related to each other through Kirchoff's law: $j(\nu)/k(\nu) = B(\nu)$, with B a Planckian blackbody spectrum (this is essentially a restatement of detailed balance), so emissivities do not need to be reported separately. Most rad-hydro codes perform significant averaging over photon energies before starting radiation transport calculations, reducing the 10^4 photon-energy gridpoints to 10^2 or fewer photon energy bins.

In steady state ($dX/dt = 0$) [11] and for the special case of $T_r = 0$, non-LTE properties can be tabulated and used in a similarly straightforward and efficient way to the LTE case. While Kirchoff's law no longer holds for $T_r = 0$, so that emissivities must be tabulated along with absorption coefficients, the resultant non-LTE tables remain tractable. However, the completely general non-LTE case must consider variations in each of 10^4 photon energy bins that must span orders of magnitude in intensity, from an ill-defined effective zero to the largest likely radiation field present at a given frequency in a given plasma. This enormous dimensionality prohibits straightforward non-LTE tabulation.

Several approaches have been taken to tabulate non-LTE properties, all of which are aimed at specific plasma conditions that constrain the radiation fields in some way. For RES plasmas, local radiation fields are produced by bound-bound line emission from hot plasma regions and the incident radiation spectrum at any point in the plasma varies from effectively zero to an optically thick spectrum whose intensity depends on the global plasma's optical depth. Researchers from the Naval Research Laboratory developed a tabular collisional-radiative model (TCRE) [119] that parameterizes radiation fields according to the optical depth of strong K-shell lines. A similar model was developed by one of us and used in the analysis of wire-array emission spectra from the Z Machine [120]. For ICF plasmas at the National Ignition Facility, where the radiation field

[11] Time dependence can be captured by inline non-LTE models but is extremely challenging to tabulate. Our approach to incorporating time-dependent effects in non-LTE radiation-hydrodynamics is described in Section 3.4

is provided by the near-Plackian emission from a high-Z hohlraum, a different approach must be used: Scott et al. [121] have developed a linear response matrix (LRM) approach that records the emission and absorption values – and a matrix of their gradients – of 10^2 photon energy bins under small variations from a reference spectrum. Here, the reference spectrum is selected to resemble the $T_r \approx 300$ eV + M-shell gold emission of a NIF hohlraum. Related work has explored coarsening the photon energy bin structure to capture only a handful of bands [122].

While the TCRE and LRM approaches have been very successful in their intended domains, this LDRD attempted to develop a tabular non-LTE scheme that would be more general, aiming to capture non-LTE effects for not only optically thick and hohlraum plasmas but also fluorescence emission and general photoionized plasmas. Fluorescence emission occurs when high-energy photons (or hot, non-thermal electrons) ionize an inner-shell electron in a cold material and the resultant hole is filled by the radiative decay of another electron. Fluorescence spectra obtained from ICF plasmas on both Z and NIF, where x-rays from the hot fusion core drive photoionization in transition-metal dopants in relatively cold external shells, have been used to help diagnose temperatures and areal densities critical to understanding confinement [100, 123]. Fluorescence emission is also important to RES source development on Z, since hot electrons accelerated in voltage gaps may provide substantial warm X-ray emission [124]. Our interest in general photoionized plasmas is related in part to the Z Astrophysical Properties Program (ZAPP) [125], which uses the X-ray flux from wire array implosions to drive ionization in nearby samples [126] Our tabulation strategy is illustrated by the sample table shown in Fig. 3-2. For each electron temperature-density point, we first assign a number of radiation bins n_{bin} and a number of radiation field points for a) optically thick cases (n_{tau}) b) fluorescence emission (n_{fluor}) and c) general photoionization ($n_{pi} = n_{Pr} - n_{tau} - n_{fluor}$). In the sample table, the optically thick points are outlined in blue, the fluorescence points are outlined in magenta, and LTE cases are outlined in red. The user can specify n_{bin}, n_{tau}, n_{fluor}, and the total number of radiation fields n_{Pr}. A complete description of the input and output quantities is given in Table 3-1. [12]

For each temperature and density, we begin by computing an optically thin spectrum with $T_r = 0$ and find the peak line-center absorption coefficient k (units of 1/cm). We assign the effective-zero input radiation field j_{in} to be the self-emission from a plasma whose size x (in cm) ensures a peak optical depth $\tau = kx \ll 1$, and then perform $(n_{tau} - 1)$ calculations that systematically increase the peak optical depth up to values sufficient to impact the ionization ($\tau \gg 100$). Each of these optically thick calculations uses the escape-factor approximation to calculate the detailed effects of self-photopumping in a uniform plasma of the given size. This ensures that the driving radiation in these cases corresponds to a highly resolved input spectrum regardless of the coarseness of the radiation bin structure. Since the output kP values are averaged over coarse radiation bins, we also track and record the deviation of the detailed absorption k_ν from the averaged absorption $\langle k_P \rangle$ in each bin. This gives us a factor $f_k = \langle (\langle k_P \rangle - k_\nu)^2 \rangle / \langle k_P \rangle$ that helps capture line-dominated radiation transport even with coarse radiation bins. Typically, we use $n_{tau} = 3 - 4$ and vary the peak line-center optical depth from about 0.1 to 1000; a plasma with an

[12] We note that the tabulated electron-ion equilibration times (which are derived from the inelastic collisional rates in the CR model) tend to be factors of m_i/m_e longer than the electron-ion collision times (derived from the simple Lee-More approximation for momentum scattering). This is roughly consistent with the small zero-frequency-limit contributions of inelastic scattering to the dynamic collision frequencies described in sec 2.4 and the relatively long electron-ion equilibration times described in Appendix A.

```
SCRAM version 8.0
hybrid structure + SC with flag        2000
   Cu  element
   29  nuclear charge
63.55  atomic weight
    3  electron temperature points (eV)
  3.333E+02   1.000E+03   3.000E+03
    1  electron density points (e/cc)
  1.000E+19
   12  radiation field points (J/cc)
 3  1  ntau, nfluor
    3  radiation groups; boundaries in eV
  2.000E+02   8.432E+02   3.556E+03   1.500E+04
```

Ne(e/cc)	Te(eV)	J/cc	J/cc	J/cc	Tr(eV)	fTr	tauR	mdet	zbar
1.000E+19	3.333E+02	5.107E-02	1.780E-02	6.342E-08	3.333E+02	0.000E+00	1.000E-01	-1	1.813E+01
1.000E+19	3.333E+02	2.847E+00	9.623E-01	6.589E-06	3.333E+02	0.000E+00	1.000E+01	-1	1.826E+01
1.000E+19	3.333E+02	6.144E+01	4.266E+01	5.640E-04	3.333E+02	0.000E+00	1.000E+03	-1	1.871E+01
1.000E+19	3.333E+02	4.642E-05	3.135E-03	1.463E-01	1.000E+04	1.150E-11	0.000E+00	1.421E-03	1.813E+01
1.000E+19	3.333E+02	1.621E+03	9.939E+01	1.085E-07	1.101E+02	1.000E+00	0.000E+00	-1	1.936E+01
1.000E+19	3.333E+02	5.406E+03	1.291E+03	1.026E-03	1.513E+02	1.000E+00	0.000E+00	-1	2.270E+01
1.000E+19	3.333E+02	8.508E+03	3.271E+03	2.368E-02	1.734E+02	1.000E+00	0.000E+00	1	2.458E+01
1.000E+19	3.333E+02	1.292E+04	7.669E+03	3.751E-01	1.986E+02	1.000E+00	0.000E+00	1	2.622E+01
1.000E+19	3.333E+02	1.897E+04	1.686E+04	4.284E+00	2.275E+02	1.000E+00	0.000E+00	1	2.682E+01
1.000E+19	3.333E+02	2.700E+04	3.514E+04	3.679E+01	2.606E+02	1.000E+00	0.000E+00	1	2.696E+01
1.000E+19	3.333E+02	4.772E+04	1.192E+05	9.881E+02	3.333E+02	1.000E+00	0.000E+00	1	2.700E+01
1.000E+19	3.333E+02	8.340E+04	9.929E+05	2.776E+05	6.667E+02	5.000E-01	0.000E+00	1	2.722E+01
1.000E+19	1.000E+03	6.340E-03	1.052E-01	8.180E-05	1.000E+03	0.000E+00	1.000E-01	-1	2.003E+01
1.000E+19	1.000E+03	5.806E-01	6.075E+00	8.173E-03	1.000E+03	0.000E+00	1.000E+01	-1	2.004E+01
1.000E+19	1.000E+03	1.466E+01	3.770E+02	6.862E-01	1.000E+03	0.000E+00	1.000E+03	-1	2.082E+01
1.000E+19	1.000E+03	4.642E-05	3.135E-03	1.463E-01	1.000E+04	1.150E-11	0.000E+00	1.413E-03	2.003E+01
1.000E+19	1.000E+03	3.675E+03	5.790E+02	6.267E-05	1.359E+02	1.000E+00	0.000E+00	-1	2.219E+01
1.000E+19	1.000E+03	5.175E+03	1.180E+03	7.529E-04	1.495E+02	1.000E+00	0.000E+00	-1	2.320E+01
1.000E+19	1.000E+03	7.158E+03	2.298E+03	7.294E-03	1.644E+02	1.000E+00	0.000E+00	1	2.453E+01
1.000E+19	1.000E+03	9.727E+03	4.297E+03	5.814E-02	1.808E+02	1.000E+00	0.000E+00	1	2.581E+01
1.000E+19	1.000E+03	1.299E+04	7.752E+03	3.881E-01	1.989E+02	1.000E+00	0.000E+00	1	2.658E+01
1.000E+19	1.000E+03	1.706E+04	1.355E+04	2.206E+00	2.188E+02	1.000E+00	0.000E+00	1	2.687E+01
1.000E+19	1.000E+03	4.885E+04	1.255E+05	1.125E+03	3.370E+02	1.000E+00	0.000E+00	1	2.700E+01
1.000E+19	1.000E+03	1.696E+05	2.060E+06	5.988E+05	6.740E+02	1.000E+00	0.000E+00	1	2.787E+01
1.000E+19	3.000E+03	1.094E-03	2.719E-02	6.806E-03	3.000E+03	0.000E+00	1.000E-01	1	2.647E+01
1.000E+19	3.000E+03	1.117E-01	2.619E+00	6.413E-01	3.000E+03	0.000E+00	1.000E+01	1	2.647E+01
1.000E+19	3.000E+03	1.503E+01	1.509E+02	3.815E+01	3.000E+03	0.000E+00	1.000E+03	1	2.653E+01
1.000E+19	3.000E+03	4.642E-05	3.135E-03	1.463E-01	1.000E+04	1.150E-11	0.000E+00	1.365E-03	2.647E+01
1.000E+19	3.000E+03	3.779E+04	7.181E+04	2.638E+02	3.000E+02	1.000E+00	0.000E+00	1	2.702E+01
1.000E+19	3.000E+03	1.748E+05	2.201E+06	6.855E+05	6.874E+02	1.000E+00	0.000E+00	1	2.834E+01
1.000E+19	3.000E+03	5.329E+05	1.913E+07	6.365E+07	1.575E+03	1.000E+00	0.000E+00	1	2.900E+01
1.000E+19	3.000E+03	1.122E+06	5.825E+07	7.790E+08	3.000E+03	1.000E+00	0.000E+00	1	2.900E+01
1.000E+19	3.000E+03	1.185E+06	7.442E+07	2.449E+09	6.000E+03	5.000E-01	0.000E+00	1	2.900E+01
1.000E+19	3.000E+03	2.435E+06	1.674E+08	8.495E+09	1.200E+04	5.000E-01	0.000E+00	1	2.900E+01
1.000E+19	3.000E+03	4.936E+06	3.547E+08	2.202E+10	2.400E+04	5.000E-01	0.000E+00	1	2.900E+01
1.000E+19	3.000E+03	9.937E+06	7.298E+08	4.986E+10	4.800E+04	5.000E-01	0.000E+00	1	2.900E+01

Figure 3-2 Example non-LTE table with blue outlines for optically thick cases, magenta outlines for fluorescence, and dark red outlines for LTE. Here, we have enforced $\Delta Z^* \approx 2$

infinite optical depth will produce its own blackbody radiation field with $T_r = T_e$ and will thus be in LTE.

To capture fluorescence, we assign a very high color temperature to an external Plankian radiation field and apply a significant dilution factor to ensure that a) there are a sufficient number of high-energy photons to produce non-thermal fluorescence emission and b) the diluted radiation field does not substantially affect the ionization. For a color temperature of 10 keV, the dilution factor is about $10^{-30} n_e$. Within the CR calculation, we track and record a factor $f_j = [j_P(n_{fluor}) - j_P(1)]/j_P(n_{fluor})$, which is the fraction of emission that is driven by the non-thermal radiation field in each radiation bin. We also track the ratio of photoionization rates to the rate of collisional ionization that would occur from hot electrons in a Maxwellian distribution with a hot-electron temperature of $T_h = 2 * E_K$, (80% of which will lie above the K-shell ionization threshold E_K) and use this ratio to assign and record an equivalent hot electron fraction f_h. This entry in the table can thus be used to estimate fluorescence line emission from both high-energy photons (where it will scale directly with $f_j j_{in}$) as well as hot electrons (where it will scale directly with f_j and the hot electron density $n_h = f_h * n_e$). The tabulated fluorescence emission includes bound-bound characteristic line emission as well as free-bound radiative recombination, whose slope is characterized by $exp^{-h\nu/T_e}$. Hot-electron-driven fluorescence requires the addition of an analytical free-free component to capture bremsstrahlung from the non-thermal populations: $j_{ff} = 1.2 \times 10^{-23} f_h n_e Z^{*2} exp^{-h\nu/T_h}/T_h^{1/2}$ W/ion. Thus fluorescence driven by both external photons and hot electrons can be reproduced using a table with a *single* fluorescence point. [13] The extension to non-thermal electrons goes beyond the scope of the original proposal and we hope to implement it in hybrid design codes that track the production of non-thermal electrons.

Finally, the tables sample a variety of Planckian radiation fields with color temperatures T_c and dilution factors of 1.0 for $T_c \leq T_e$ and 0.5 for $T_c > T_e$. These dilution factors are chosen to a) provide a touchstone to LTE for $T_c = T_e$ and b) transition to half-sky illumination for general photoionization. The lowest color temperature in this section of the table is calculated using the slope of ionization against the total incident energy in the radiation field derived from the optically thick cases; we aim for the first photoionized case to have $\Delta Z^* \approx 1$ from the thickest case. Generally, this requires T_c with 2 - 10 times more total energy than the driving field of the thickest case, and we restrict T_c to be $\leq T_e$ to ensure that the LTE touchpoint is captured. We then systematically increase T_c, and can aim to either a) reach a fixed peak radiation temperature in fixed number of radiation field points remaining or b) (recommended) take steps that ensure $\Delta Z^* \leq 2$ to avoid large changes in the emission spectra. In either case, we make sure to capture $T_c = T_e$ for LTE if allowed by n_{Pr}. [14] Defining the photoionization cases in this way ensures monotonicity in the tabulated input radiation fields and Z^*, which is helpful for the interpolation.

This physics-based tabulation strategy provides a compact representation of an enormous range of

[13] Early versions of the tables used n_{fluor} = 4 and sampled several non-thermal color temperatures for the radiation field, but we found that the additional complexity confused the interpolation and was not as accurate as a straight scaling of the non-thermal fraction of the emission in each bin to the driving radiation field intensity.

[14] For example, in the sample table of fig. 3-2, we haveixed the number of radiation fields for each temperature-density point to be 12., so the case with $T_e = 1keV$ did not reach the LTE condition

plausible non-LTE radiation fields using only $10-20$ radiation fields for each temperature-density point. The EOS and transport data it produces thus require only about $10\times$ more memory than EOS and transport data from the LTE tables now in use. And since our calculations incorporate the full detail and extent of self-opacity and external Planckian radiation fields, regardless of the bin structure or output energy range, we can specify a very coarse radiation bin structure ($n_{bin} = 3-10$) that compensates for the increase in table size accrued by incorporating the radiation field. Users can select the number of radiation point as well as the number of bins, or even input a pre-specified bin structure.

Since these compact tables can be pre-computed with detailed CR models like SCRAM and DFT-AA, which are far too expensive to run inline in rad-hydro simulations, they offer a significant increase in accuracy over inline models but incur only a minimal increase in computational cost (runtime). The compactness of the present tables does carry some drawbacks, however: First, the various opacity and fluorescence factors may not be trivial to incorporate into radiation-hydrodynamics codes (like any tabular non-LTE method). Perhaps more importantly, coarse binning may not be sufficiently accurate for some radiation transport calculations: convergence studies with inline non-LTE in NIF hohlraums suggest that 10^2 bins are required for reasonable energy balance near LTE. While understanding the interplay of known inaccuracies in binning/transport with known inaccuracies in the highly simplified inline CR models is beyond the scope of this LDRD, we plan to explore these issues in continuing collaborations with the developers of inline and LRM models.

In addition to the compact tables for read-in to the rad-hydro code, we also compute accompanying tables of detailed emission and absorption spectra suitable for use in post-processors (see sec. 4) that can generate synthetic data for direct comparison to experimental measurements. These accompanying tables have 10^{3-4} frequency points for each temperature, density, and radiation field, and accommodate sparse frequency sampling in line-free regions of the spectrum that can significantly reduce the size of tables with high spectral resolution. The detailed spectra also allow bespoke re-binning of the coarse radiation groups when needed.

3.3. Non-LTE table interpolation

The table strategy we have described so far draws on previous work for three components: a) optically thick emission b) fluorescence emission, and c) Planckian radiation fields (photoionization). In this section, we will test focused interpolation schemes for each table component and describe a global interpolation scheme that can be used inline in rad-hydro codes and post-processors. In all cases, we illustrate the interpolation schemes by comparing the detailed emission spectra from the supplementary tables described above, since they provide a stringent test of the interpolation methods and their accuracy should be representative of interpolation on the radiation-binned quantities reported in the compact tables. We also interpolate only on the radiation field, leaving interpolation on temperature and density to standard methods, where interpolated quantities Q_i are given by piece-wise linear interpolation of $\ln(T_e)$ and $\ln(n)$: e.g. $\ln[Q_i(X_i)] = exp[f_{i-1}\ln(Q_{i-1}) + (1-f_{i-1})\ln(Q_{i+1})]$, where Q_{i-1} and Q_{i+1} are the tabulated quantities at the nearest gridpoints above and below the independent variable X_i (temperature or density), and $f_{i-1} = [\ln(X_{i+1}) - \ln(X_i)]/[\ln(X_{i+1}) - \ln(X_{i-1})]$.

input	fields	description
Ne(e/cc)	1	density (electron, ion, or mass density)
Te(eV)	1	electron temperature
rin (J/cc)	n_{bin}	incident radiation field
Tr(eV)	1	radiation temperature
fTr	1	radiation dilution factor
tauR	1	peak line-center optical depth
mdet/fh	1	model type (hydrogenic or detailed) OR hot electron fraction f_h
output	fields	description
zbar	1	average ion charge Z^*
mu(eV)	1	chemical potential
Ee(J/g)	1	internal energy (electron)
Ei(J/g)	1	internal energy (ion)
Pe(bar)	1	pressure (electron)
Pi(bar)	1	pressure (ion)
tee(s)	1	electron-electron collision time
tei(s)	1	electron-ion collision time
tceq(s)	1	collisional equilibration timescale
treq(s)	1	radiative equilibration timescale
econd(S/cm)	1	electrical conductivity
Kt(W/cm/eV)	1	thermal conductivity
Cve(J/eV/g)	1	heat capacity (electron)
Cvi(J/eV/g)	1	heat capacity (ion)
Cs(cm/s)	1	sound speed
kR(cm2)	n_{bin}	Rosseland mean opacity (inverse, weighted by dB/dt)
kP	n_{bin}	Plank mean opacity (direct, unweighted)
jP(W/ion)	n_{bin}	Planck emissivity (sum)
kPfac	n_{bin}	opacity factor f_k OR fluorescence factor f_j

Table 3-1 Tabulated quantities for non-LTE EOS, transport, and radiative properties. SCRAM tables use ideal gas approximations for pressures and sound speed, the Lee-More [51] approach for conductivities and collision times, and internal collisional-radiative-rates for equilibration times. SCRAM gives very reliable ionization and radiative properties for below-solid densities. Tables from our DFT-AA model will have more rigorous EOS and transport properties and slightly rougher approximations for radiative properties, as described in section 2. For either type of model, the EOS, transport, and radiative properties are internally consistent – that is, they are based on the same underlying atomic data.

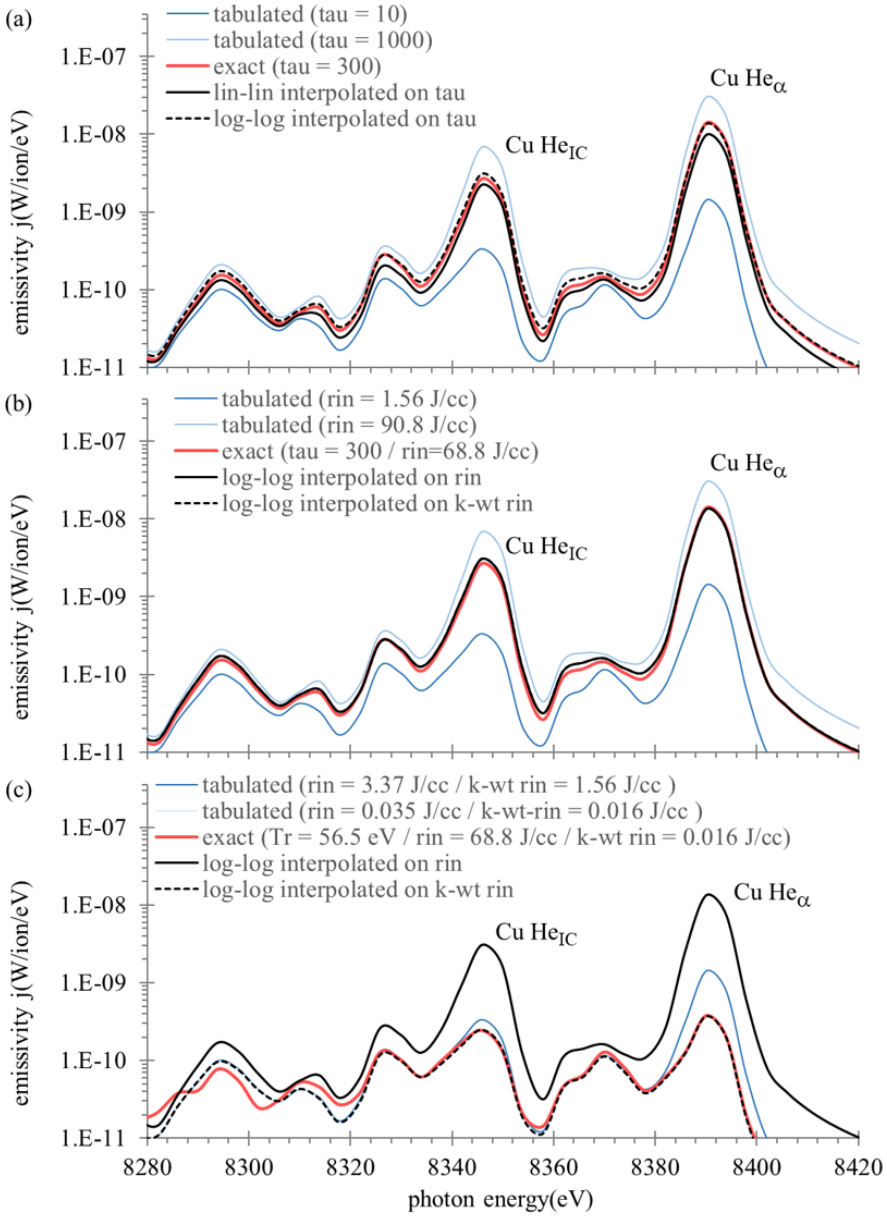

Figure 3-3 Interpolation of the optically thick table entries for copper with $T_e = 3$ keV and $n_e = 1-^{19}$cm^{-3}. (a) Log-log (dashed black) and lin-lin (solid black) interpolation between nearest table entries (light lines) on the peak line-center optical depth τ, compared to the exact calculation with $\tau = 300$ – the log-log interpolation is significantly better. (b) Log-log interpolation for the same case, but on the total radiation field (solid black) and on the k_P-weighted field (dashed black) – the curves are almost identical (c) Log-log interpolation for an incident Planckian radiation field with the same total radiation field as the $\tau = 300$ case, interpolated on the total radiation field (solid black) and on the k_P-weighted field (dashed black) – the k_P-weighted interpolation is an order of magnitude better.

Previous work with tabulated emission and absorption from line-dominated optically thick plasmas demonstrated that a simple interpolation on the peak line-center optical depth τ is generally a good approximation for emissivities and opacities. Figure 3-3a shows a comparison of interpolations (lin-lin and log-log) between nearest-neighbor tabulated cases (given by light lines) for τ=300 from the T_e = 3 keV copper tables illustrated above, which were tabulated on τ=[0.1, 10, 1000] against an exact calculation at τ=300. The labeled Cu He$_\alpha$ line is optically thick, while Cu He$_{IC}$ and the surrounding satellites are relatively thin. Here, the log-log interpolated intensities are within a few % of the exact calculation, while lin-lin interpolation has errors up to 30% at the Cu He$_\alpha$ peak. Importantly, however, rad-hydro codes do not have direct access to the τ of an arbitrary plasma volume embedded in a larger plasma; instead, they track the binned incident radiation fields. Figure 3-3b shows interpolation on the total incident radiation intensity (a simple sum over all bins), along with a modified log-log interpolation on a k_P-weighted radiation field $\sum_{bins} k_P^{bin} / (\sum_{bins} k_P^{bin}) r_{in}^{bin}$ (for reasons that will become evident soon). Since both of these scale very closely with τ, the accuracy of both interpolations is very similar to that of direct interpolation on τ. [15]

While log-log interpolations on the peak optical depth, the total radiation field, and the k_P-weighted radiation field all give very good agreement with exact calculations of emission from plasmas with line-dominated radiation fields, we want our tables to be reliable for general radiation fields as well. In general, Planckian radiation sources and emission from other elements will not have the same resonant photopumping effects as line emission from the same element in similar plasma conditions. To test this part of the table far from its intended regime, we consider the effect of an external Planckian blackbody with the same total radiation field as the case with $\tau = 300$, and note that while the high-τ case has an incident radiation field dominated by radiation in the L- and K-shell energy bins, the Planckian case has 99% of its radiation in the lowest-energy radiation bin. And while the high-τ incident field has a profound effect on the emission intensity due to resonant photopumping of the lines, the Planckian radiation field has negligible impact on the emission. Thus, interpolation on the total energy of the incoming radiation field will lead to order-of-magnitude errors, as illustrated in fig. 3-3c. Weighting the incoming radiation field by the k_P factor described above is a reasonable way to correct for this error, since the Planckian mean opacity is dominated by absorption in the L-and K-shell bins, with the lowest-energy bin having a fraction of only about 3×10^{-5} of the total Planckian mean opacity.

For fluorescence emission, our tables use a single radiation field selected to provide significant fluorescence emission without significantly impacting the thermal ionization. Non-thermal fluorescence occurs following ionization of an inner-shell electron – whether that ionization is from photoionization or collisional ionization. The tables record the results of K-shell photo-fluorescence, which occurs following photoionization from incident photons with energies above the K-shell ionization threshold $E_K \approx 13.6 * (Z - 1.5)^2 eV$. We find that the K-shell fluorescence emission roughly scales directly with the incident radiation field strength in the

[15] This part of the table uses an escape-factor method that implicitly invokes a highly structured self-generated radiation field dominated by strong lines. While this approach is robust to changes in both the bin structure of the compact tables and the spectral resolution of the detailed tables, radiation transport of strong lines is distinct from radiation transport of smooth continuum emission (or of line emission from other materials). Thus, when these table entries are called in rad-hydro calculations, the absorption coefficient for transport in each bin should be multiplied by the factor f_k to accurately estimate the incoming radiation fields (see section 4.1).

K-shell radiation bin. Since photoionization cross sections peak near the threshold energy E_K and fall as $(E_K/h\nu)^3$ above threshold, this bin-specific scaling should hold for most Planckian sources and can even provide reasonable estimates for fluorescence emission driven by x-ray free-electron lasers (XFEL) with beam energies $E_{beam} > E_K$. Our test case here is the copper table with T_e=333 eV, with $E_K = 10.3keV$, for which $f_j^{bin} = [0,0.03\%$, and $99\%]$ for the three photon energy bins (the last represents the K-shell emission, 99% of which arises from non-thermal processes). The output radiation spectrum is estimated by $j_\nu^{out} = j_\nu^{tab}[1 + f_j^{bin}(r_{bin}^{in} - r_{bin}^{tab})/r_{bin}^{tab}]$, using bin-specific input radiation fields r_{bin}^{in} and r_{bin}^{tab}, f_j^{bin}, and j_ν^{tab} values from the fluorescence table entry.

Figure 3-4a shows an example of interpolating fluorescence emission for a radiation field with T_r = 3 keV and dilution factor of 10^{-8}, which has a K-shell radiation energy density of about 8 J/cc (compared to the tabulated value of about 0.14 J/cc). The agreement is within a factor of two for the K_α fluorescence emission. Although the simple scaling overpredicts the continuum emission in the low-energy part of the K-shell bin, that emission is not typically energetically or diagnostically important. If needed, a continuity condition across bins could be imposed. This case represents the behavior one might see when calculating fluorescence from impurities in the cool liner region surrounding the hot fusion core of a MagLIF plasma, with the sky factor reduced from the $\approx 10^{-3}$ value of a real MagLIF plasma by the density factor $10^{19}/10^{24} = 10^{-5}$ to account for the higher sensitivity of low-density plasmas to external radiation.

Figure 3-4b shows interpolation of an XFEL beam centered at $E_b = E_K = 10.3$ keV, with a square profile over a bandwidth of $0.01E_b$ (103 eV) and an intensity of 10^{12} W/cm^2 (again, we have scaled down typical XFEL intensities by about 10^{-5} for this low-density test case). This radiation field has about 32 J/cc in the K-shell radiation bin. Here, too, the scaling of the fluorescence part of the emission matches the exact calculation rather well in the K-shell line region and higher energies. If the XFEL beam were at a photon energy significantly higher then E_K, we might need to consider including an additional factor of $(E_K/E_{beam})^3$ to account for the decaying photoionization cross section.

Since fluorescence emission is a relaxation process that follows inner-shell ionization from any mechanism, we can also use this single point in our table to estimate hot-electron-driven fluorescence. The tabulated f_h factors are based on ratios of collisional ionization from a hot electron distribution with temperature $T_h = 2E_K$ and number density of $f_h * n_e$ to the photoionization rates from the incident radiation field, and can be scaled to general hot electron distributions. Since collisional ionization cross sections have a much gentler scaling with incident energy than photoionization (they scale roughly as $\ln(x)/x$, with $x = \varepsilon_e/E_K$)), fluorescence emission from hot electrons scales roughly with the number of electrons above the threshold energy E_K [127]. Hot Maxwellian distributions with temperatures T_h have electron energy probability distribution functions $F_M(\varepsilon_e) = (4\varepsilon_e/\pi T_h^3)^{1/2} e^{-\varepsilon_e/T_h}$, of which a fraction $f_> \approx \max[1,(2/\sqrt{\pi})e^{-0.72E_K/T_h}]$ (for $T_h > E_K$) have energies greater than E_K: $f_> \approx 0.8$ for $T_h = 2E_K$ and goes to unity for $T_h \gg E_K$. Figure 3-4c shows a comparison of the exact hot-electron fluorescence spectrum from 0.01% hot electrons at T_h = 100 keV to an interpolation of the K-shell emission $j_{\nu(K)}^{out} = j_{\nu(K)}^{tab} f_j^{bin}(f_>^{in} f_h^{in})/(0.8 f_h^{tab})$. This interpolation for hot electrons directly scales the approximate number of hot electrons above the K-shell edge of an input hot electron distribution to the fluorescence intensity tabulated for a known hot electron fraction, temperature, and $f_>$. Like the photo-fluorescence scaling, it accounts for the fraction of emission that is

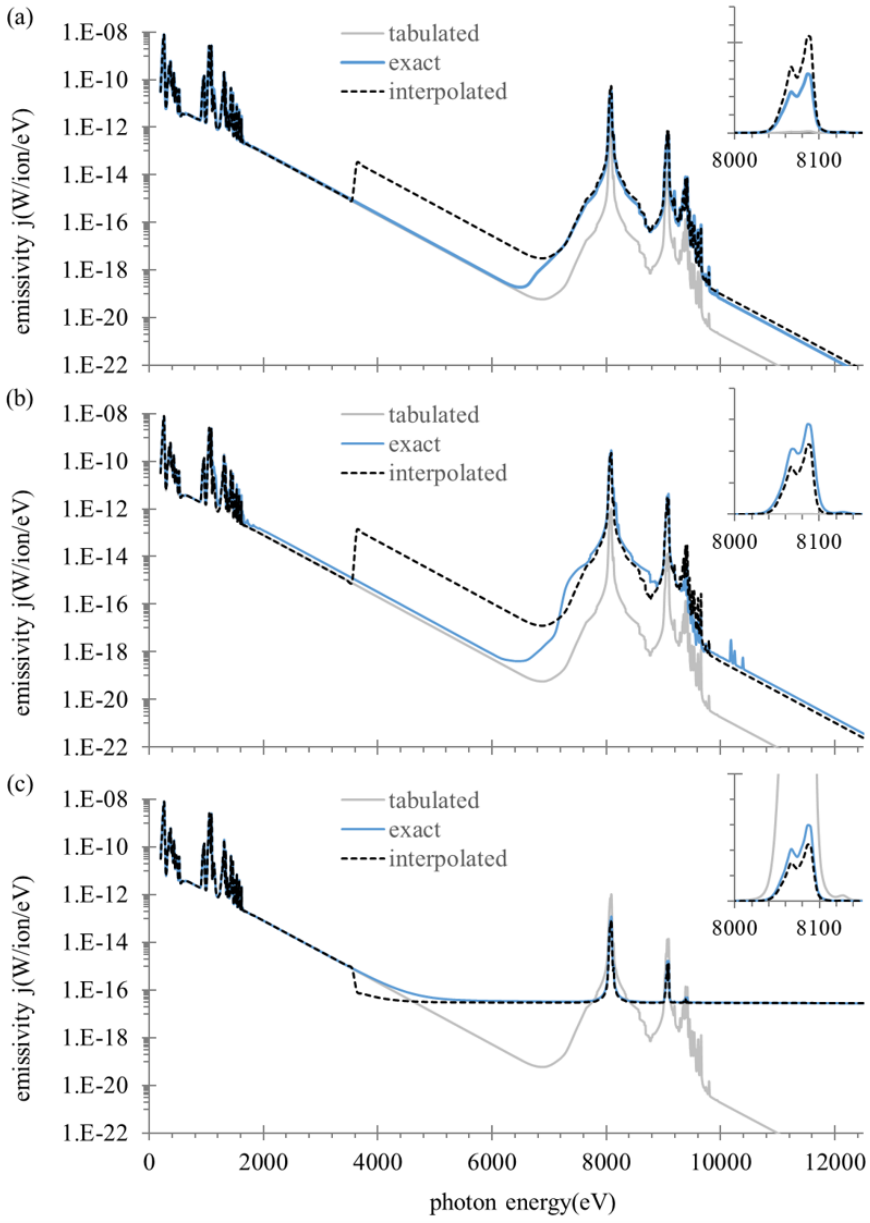

Figure 3-4 Interpolation of non-thermal fluorescence emission from copper with $T_e = 333$ eV and $n_e = 1{-}^{19}\text{cm}^{-3}$. (a) Fluorescence from an external radiation temperature much lower than the tabulated fluorescence case, relevant to inertial fusion diagnostics. (b) Fluorescence from a free-electron laser with bandwidth 0.01 and beam energy $E_b = E_K = 10.3$ keV. (c) Hot-electron fluorescence from $f_h = 10^{-4}$ electrons at $T_h = 100$ keV, scaling to a tabulated equivalent hot electron fraction for $T_h = 2E_K$ keV and adding an analytical contribution for the free-free bremsstrahlung emission. Insets show linear-intensity plots of the fluorescence K_α lines and gray lines are the single tabulated spectrum from which all of the interpolations are made.

non-thermal. Unlike photo-fluorescence scaling, this should only be applied for K-shell fluorescence (the radiation from other bins is taken to be thermal). Since fast electrons can also contribute significantly to bremsstrahlung emission, so we include an approximate additional continuum term: $j_{ff} = 3 \times 10^{-32} f_h n_e Z^{*2} \mathrm{e}^{-h\nu/T_h} / T_h^{1/2}$ W/ion/eV.

In all of the cases shown in fig. 3-4, the tabulated fluorescence spectrum is given by the gray line. Together, the three plots demonstrate that linear scaling of fluorescence emission to 1) the radiation energy density or 2) the number of hot electrons above the K-edge both provide reasonably accurate pictures of fluorescence emission –even when the input fields and intensities are orders of magnitude away from the tabulated values, and even when the input radiation (or non-thermal electron) distribution is quite far from the tabulated case.

A universal interpolation scheme should perform about as well as each of the tailored interpolation schemes described above. So far, we have implemented two approaches for universal interpolation, both of which incorporate the direct opacity factor f_k when invoking table elements with radiation fields driven by self-opacity and f_j when invoking table elements with fluorescence. The first, denoted "k-wt," is described above: it performs an interpolation on the total J/cc radiation field with each radiation bin weighted by the $T_r = 0$ Plackian opacity k_P^0. Here, the interpolation routine finds the two tabulated points with the closest opacity-weighted intensities and then interpolates between them.

A second attempt at a universal interpolation scheme uses a distance-weighted matrix method (Sheperd's method). This scheme computes the linear or logarithmic distance between intensities in each radiation bin, d, and returns a weight for the output of each tabulated radiation field that scales with d^{-m}, with the total weight normalized to unity. Here, m can be varied to restrict or expand the weighting function: typically, we use $m = 3$. As illustrated in sections 3.4.3 and 4.1, these "universal" interpolation schemes can provide reasonable results. We have also investigated interpolation forcused on photoionized plasmas, including the particularly challenging cases described in [121, 122], where radiation fields contribute to the ionization of a material through an open shell and where the radiation fields have both thermal and non-thermal components. So far, we have not found a general interpolation method that works as well as for the cases described above: we find that the k_P^0-weighted interpolation is quite good for thermal radiation fields, but the matrix interpolation better captures non-thermal effects (e.g. of M-shell Au radiation in a hohlraum). However, neither is optimal and better approaches will be explored in future work: in particular, we will investigate whether separating the interpolation on the radiation bins can provide robust performance for non-thermal sources and whether the table strategy should be adjusted to limit step-sizes of radiation field intensities for critical energy bins.

3.4. Non-LTE implementation in GORGON

Multi-dimensional radiation-MHD calculations applied to high energy density (HED) problems of interest can quickly become slow and cumbersome to run, and run-time issues are compounded when non-LTE is required in the radiation physics (as is typically the case). The dependence of emissivities and opacities on the background radiation environment in non-LTE plasmas typically requires a simplified atomic physics model to be run in-line with the calculation, and the costs of

even simplified non-LTE atomic models often dominate the run-time. An alternative non-LTE scheme that references pre-tabulated data is attractive because of its potential to both significantly reduce simulation run-time and to increase accuracy over simple inline models.

Since tabulated data is already used routinely in simulations for referencing material models, a single-point tabulation scheme for non-LTE conditions also offers the potential benefit increased consistency: the broader material properties (e.g. pressures, ionization, conductivities and opacities) are typically derived from different sources, which introduces inconsistencies even before non-LTE effects are taken into account. For example, with different assumptions and dependencies, the electrical conductivity model may assume a different ionization state than the atomic physics model being used for EOS, and both might be different from the ionization of the radiation model. In large, multi-physics systems, the effects of such inconsistencies can be difficult to quantify – not least because the interplay between different physics processes can be difficult to replicate in anything short of a complete target simulation. Furthermore, reference simulations that do not employ differing assumptions are not generally available.

In HED physics problems, the accuracy of material models is often a key factor in the accuracy of a simulation's predictions for a given experiment. That is, few-% differences between different numerical treatments of the hydrodynamics will be easily dwarfed by 10% differences in EOS data or factor-of-two differences in the radiative properties. This has long been asserted in the material science program at Sandia, where accurate models of the conductivity and equation of state are considered essential. So, too, is consistency between those models. For example, ensuring that the density and temperature of a melt transition is consistent between an equation of state model and an electrical conductivity model has been shown to be essential in accurately predicting magnetic field diffusion through an accelerating plate [27]. Studying the effects of model consistency when radiation physics dominates is in its early stages since it first requires multi-physics simulation tools capable of undertaking such a study as well as material models and/or data tables that strictly enforce consistency.

There are consequently two goals in pursuing a tabulated non-LTE radiation treatment:

1. Minimize the computational cost of non-LTE radiation transport
2. Run calculations with a self-consistent and radiation-aware set of material and transport parameters

3.4.1. Background description of existing methods

We first outline the simple radiation transport approach used by Sandia's version of the radiation-magneto-hydrodynamics (R-MHD) code Gorgon prior to this LDRD, detailing its assumptions and highlighting areas where inconsistencies existed among the support models used throughout the calculation. This will provide a baseline description of a code whose structure is representative of the approaches often taken in HED simulations. It will also provide context for the choices made in the subsequent implementation of the self-consistent tabulated non-LTE model. The baseline code approach we describe is a R-MHD research code maintained at Sandia that implements the Gorgon system of MHD equations [128], a variation of the automatic flux

limiting ZEUS-2D approach for radiation transport [129], and various interfaces to tabulated equation-of-state, conductivity and material property data.

One of the simplest radiation transport approximations that can be employed is to simultaneously solve two evolution equations for the radiation energy density E and radiative flux F:

$$\frac{\partial E}{\partial t} = -\nabla \cdot F + \eta - c\kappa_P E \tag{25}$$

$$\frac{1}{c^2}\frac{\partial F}{\partial t} = -\nabla \cdot P - \frac{1}{c}\kappa_R E \tag{26}$$

with κ_P and κ_R the Planck- and Rosseland- mean opacities, η the emissivity, and P the radiation pressure tensor. We additionally invoke the Eddington approximation to assume an isotropic radiation field and express the radiation pressure tensor P as simply $\frac{1}{3}E$. In this limit, it is common to neglect the time evolution of the second radiative flux equation and assume the steady-state limit of $F = \frac{1}{3\kappa}\nabla E$ (the traditional diffusion approximation). That is not the approach taken here, where we instead opt to explicitly integrate both equations using a standard leap-frog integration technique. To ensure that the radiative flux asymptotes to reasonable limits, this update over a simulation timestep dt is performed analytically:

$$F^{n+1} = F^n \mathrm{e}^{-c\kappa\, dt} - (1 - \mathrm{e}^{-c\kappa\, dt})\frac{c}{3\kappa}\nabla E \tag{27}$$

This approach allows for a seamless transition between the diffusion equation in an optically thick plasma and a wave equation propagating through transparent regions. However, the use of the Eddington approximation results in solutions that are essentially no better than a traditional diffusion approximation. The advantage of this technique (a variation on "automatic flux limiting" [129]) is that it naturally limits propagation speeds to about the speed of light, avoiding the need for flux limiters and providing a system of equations that can be integrated explicitly on a timestep set by about the speed of light. Specifically, these equations limit propagation speeds to $c/\sqrt{3}$ (a consequence of assuming isotropic radiation fields). A modification to correct this, known as the $P1/3$ approximation [130], introduces an additional factor into the flux update (b in equation 28):

$$F^{n+1} = F^n \mathrm{e}^{-b\, c\kappa\, dt} - (1 - \mathrm{e}^{-b\, c\kappa\, dt})\frac{c}{3\kappa}\nabla E \tag{28}$$

When $b = 3$, the free-space propagation speed will limit to the speed of light, but the correct diffusion limit is still retained. While this approximation seemingly corrects an issue with free-space propagation speeds, its broader utility is in highlighting how wave speed can be varied without affecting the diffusion rate in more opaque plasmas. Since we opt to explicitly integrate these equations, timesteps are set by speed of light crossing times over a computational zone. This can be excessively restrictive since our HED problems of interest typically evolve on much slower timescales. This modification thus provides a parameter to artificially reduce the propagation speed (allowing for larger timesteps), while retaining the correct diffusion limit. This

provides some additional flexibility to reduce simulation run-time while using explicit integration techniques (although care must be taken to avoid nonphysical results). Explicit integration is attractive for several reasons: First, it forgoes the need to use simulation-wide implicit integration that typically relies on large, sparse matrix inversion techniques, which makes it much simpler to efficiently distribute over massively parallel simulations (note that a guiding consideration in this tabulated non-LTE approach is allowing for efficient implementation in massively parallel simulations). Furthermore, since the timesteps used in simulations of magnetically driven laboratory HED systems are typically dictated by the MHD (high Alfven speeds from high magnetic fields in low density plasmas), radiation transport routines are often already forced to operate on small timesteps anyway, so the burden of explicit integration is often not high. Finally, small-timestep explicit integration can also simplify matter-radiation coupling by reducing changes in temperatures and energy densities between updates of material properties, which can reduce the need for non-linear iterative techniques to establish consistency between emission and absorption terms.

Within this radiation transport method, coupling to a tabulated non-LTE model primarily requires replacing opacities and emissivities with parameters that now vary in response to the changing radiation field, and duplicating the above equations for enough frequency groups to broadly characterize that radiation field. However, to understand how other material properties drawn consistently from the same non-LTE model can be incorporated, and to appreciate some of the present inconsistencies between models, we here describe the structure of the main timestep loop of the underlying finite-volume Eulerian MHD code and its interface with existing LTE tables. While the approach we describe may not reflect the approach taken in all HED or MHD codes, it is representative of some of the issues frequently encountered.

Within the main timestep loop, the hydrodynamic timestep is first calculated using the minimum computational zone size, the ion sound speed, and the Alfven speed. An additionally safety factor of 0.5 is added to ensure stability. The ion sound speed calculation assumes an ideal gas and an electron number density n_e calculated from the mas density ρ and the tabulated average ionization state Z^* included with the tabulated electrical and thermal conductivities (commonly Lee-More-Desjarlais, as described in section 2.3). Where such tables are unavailable, a Thomas-Fermi model is used for Z^*. This ionization state was also evaluated at the end of the previous timestep. Since it derives from the conductivity model, this sound speed is not guaranteed to be consistent with $c_s = (\partial P/\partial \rho)^{1/2}$ evaluated from the equation of state. While the ideal-gas ion sound speed evaluation is generally more robust than evaluating derivatives from the equation of state table, it can result in conservatively small timesteps that can directly impact the computational run time: if timesteps are factors of two too small, the simulation will take twice as long to run as needed). Still, conservative timestep choices are typically preferable to having to restart crashed simulations.

Next, transport coefficients are evaluated (electrical and thermal conductivities). These are preferably taken from trusted tables (stored as functions of density and temperature). When a 2-temperature model ($T_e \neq T_i$) is needed, the tabulated thermal diffusion coefficients are partitioned between electrons and ions assuming a Braginskii form of thermal diffusion equations. Subsequent magnetic field correction factors are either taken from Braginskii [131], or from Epperlein and Haines [132]. These correction factors require electron and ion collision

times and their associated coulomb logarithms, which we typically take from from Braginskii. In some instances, to preserve at least partial consistency, the electron-ion collision time is reverse-engineered from either the electrical or thermal LMD conductivities (again assuming a Braginskii form of the equations). Opacities and emissivities are also drawn from pre-prepared tables using the same material temperatures and densities as these transport coefficients. These radiation parameters are typically generated from PROPACEOS [133], with emissivities evaluated in either the LTE ($T_r = T_e$) or the optically thin ($T_r = 0$) limits.

Ideal MHD advection of the magnetic field is next performed on the hydrodynamic timestep. After this, material pressures are evaluated, and velocities are updated from a combination of pressure gradients and magnetic field accelerations. Here, the pressure is evaluated from the material density and temperature using a trusted tabulatd equation of state (typically SESAME). If separate electron and ion pressures are required, these are calculated by partitioning the SESAME total pressure assuming an ideal gas, using the ionization state taken from the tabulated LMD conductivity model. In addition to material pressure, an artificial viscous pressure is calculated to ensure shocks are captured in this Eulerian simulation. A von-Neumann form of artificial viscosity is used, which requires the ion sound speed (calculated in the same manner as for the timestep).

A magnetic field diffusion update is then performed utilizing the tabulated electrical conductivities. This is followed by calculation of heating terms (including ohmic, PdV and viscous heating) immediately followed by a thermal diffusion update and the radiation transport update with its associated energy exchange with the material. Note that magnetic field diffusion, thermal diffusion, and radiation transport are sub-cycled on a smaller timestep than the baseline hydrodynamic timestep. Following these energy equation updates, the material advection is performed (operator split along the coordinate directions).

The final step is to take the updated densities and energy densities and calculate the material temperatures. For a single material, this can take the form of a reverse lookup on the SESAME equation of state table. These simulations allow for multiple materials tracked by different material mass densities, while sharing a single total energy density, but for the multi-material approach an iteration must be performed where co-located materials are assumed to have the same temperature: The total energy density is calculated by summing the constituent energy densities from their respective mass densities and equations of state, then a search is performed to find the temperature that results in the code's calculated total energy density. Once a temperature is determined, the ionization state is referenced from the conductivity tables, and this Z^* is used to update the electron number densities.

While this approach is not universal, it gives some indication of the way HED simulations are often forced to piece together material properties and transport coefficients from a variety of sources to conduct viable design calculations. The effect of any inconsistencies between these models is largely unknown. More crucially, many parameters may be expected to vary with the radiation field present (for example as ionization states change in response to non-equilibrium radiation fields). This dependency is typically not captured. The need for a more unified approach is here self-evident.

3.4.2. Radiation transport techniques coupled to non-LTE tables

Time-dependent radiation transport can be solved with many different levels of approximation. In constructing a fast tabulated non-LTE MHD approach it is tempting to pair the non-LTE tables with a simple radiation transport scheme to minimize the overall computational cost. This was the approach taken above to work through MHD code implementation issues. While the simple radiation transport methods provide workable testbeds to develop the tabular non-LTE methods and have some applicability to problems of interest, they also reveal limitations that will ultimately require a higher fidelity radiation transport scheme. To understand these limitations, we couple the tabulated non-LTE approach into two time-dependent radiation transport schemes applied to an idealized radiating cylinder test problem [7].

The test problem consists of a 2 mm diameter cylinder of aluminum plasma at an electron temperature of 500 eV, with an ion number density of 10^20/cc. We assume it to be infinitely long, and hold its temperature and density fixed, allowing the radiation field within it to reach a steady state. One of the radiation transport schemes we will compare is the automatic flux-limiting radiation diffusion approximation described above. The other is a higher fidelity solution of the time-dependent radiative transfer equation.

The solution to the time dependent transfer equations follows the method of Jiang et al. [134], with the evolution of the specific intensity described by:

$$\frac{\partial I}{\partial t} = -c\frac{\partial}{\partial x}(\mu_x I) - c\frac{\partial}{\partial y}(\mu_y I) - c\frac{\partial}{\partial z}(\mu_z I) \tag{29}$$

$$\frac{\partial I}{\partial t} = \frac{c\eta}{4\pi} - c\kappa I \tag{30}$$

$$E = \frac{1}{c}\int I d\Omega \tag{31}$$

Separate updates are performed for the transport of intensity (Eq. (29)) and absorption/emission processes (Eq. (30)). Taking angular moments of the intensity to reconstruct the radiation energy density (Eq. (31)) is then required for referencing the non-LTE tabulated data. Here, the radiation intensity I is a function of time, spatial position and angle, with the angles discretized into a specified number of directions. Each direction is uniquely defined by its direction cosines with respect to the coordinate axis (μ_x, μ_y, and μ_z). For example, if 48 ray directions span a unit sphere, there will be 48 equations for the different intensities associated with each of those directions. For later examples, the transport equation is spatially discretized over a uniform 2D x-y grid, 10-mm square, with 200 equally spaced computational cells in each direction. The test case places a 2-mm diameter cylinder of aluminum plasma at the center of this grid. Angular discretization uses 48 directions, uniformly spaced around the azimuth in the plane of the simulation grid. Multiple photon energy groups are assumed (that is, a separate set of all these equations is solved for each photon energy group).

In this implementation, for each timestep advance, opacities and emissivities are first evaluated as a function of material temperature, density, and the local radiation field. Intensities are then advanced in time by performing a locally implicit update from the emission and absorption terms in Eq. (30). The intensity is then transported via a set of advection equations (Eq. (29)). Finally, the radiation energy density is evaluated (Eq. (31)), for use in referencing opacities and emissivities at the start of the next timestep.

The locally implicit update for emission and absorption terms is performed by analytically advancing Eq. (30) over a timestep:

$$I^{n+1} = I^n \mathrm{e}^{-\,c\kappa\,dt} - \frac{\eta}{4\pi\kappa}(1 - \mathrm{e}^{-\,c\kappa\,dt}) \tag{32}$$

In this update, the exponential terms are expanded as a Taylor series, retaining the first 5 terms, and the result is limited to always be positive. This provides a fast evaluation and compiler independence, and ensures the correct limit as κ becomes small.

The transport equation (Eq. (29)) is advanced as a series of finite volume advection equations, with fluxes of intensity calculated at cell faces using a simple first order donor cell upwind scheme. For example, the x-direction update proceeds as:

$$I_x^{n+1} = I_x^n - \Delta t\ c\mu_x \frac{I_x^n - I_{x-1}^n}{\Delta x}\ ;\ \text{for } \mu_x > 0 \tag{33}$$

$$I_x^{n+1} = I_x^n - \Delta t\ c\mu_x \frac{I_{x+1}^n - I_x^n}{\Delta x}\ ;\ \text{for } \mu_x < 0 \tag{34}$$

This scheme is more diffusive than the approach taken in [134], but is conservative and fast to execute – an advantage, given the large number of equations being updated and the small timesteps required (stability of the intensity advection requires $\Delta t < \Delta x/c$). Directional splitting is used, where the intensity associated with a given set of direction cosines is first updated by advection in the x-direction, followed by advection in y.

Finally, the radiation energy density for each photon energy group is evaluated by taking the angular moment of the intensity for that group. For the uniform azimuthal angle discretization used in this 2D example, this amounts to simply averaging the intensities from all different directions at each point in space (and multiplying by $4\pi/c$). These energy densities are required to reference the tabulated non-LTE data. The plasma temperature and density are held fixed in this test problem, with the radiation field rising from zero to assume a steady state. Opacities and emissivities vary in response to the changing radiation field to converge on their steady state values.

The non-LTE tables are referenced and interpolated following the procedures given in sections 3.2 and 3.3. Material properties are tabulated as functions of ion density, electron temperature, and radiation field for a modest number of frequency groups. As an example, a simple way to estimate the emissivity of one of the frequency groups for a plasma at a given temperature and density would be to first locate the temperature and density in the table and then return material properties

at the tabulated radiation field that most closely approximates the input radiation environment in the plasma. Given the coarse descriptions of the tabulated radiation fields, however, such simple lookups are inadequate. Instead, a sophisticated interpolation scheme is required to return accurate and smoothly varying quantities. As described in section 3.3, optimization of the interpolation schemes is a work in progress, and so all of the following results should be taken with the limitations of the given interpolation scheme in mind: that is, a better interpolation scheme is likely to improve the (already fairly good) results.

The metric we use here to compare tabulated and simulated radiation fields is a simple opacity weighting. For each photon energy group, a weighting function is defined which is the Planckian opacity multiplied by the mean photon energy of that frequency group. This is normalized to unity when summed over the frequency groups. The Planckian opacity used is that returned in the zero-radiation field limit. This provides a weighting value for each photon energy group as a function of material density and temperature. For each of the different tabulated radiation fields, we then calculate the sum of this weighting function and the energy density in that frequency group, providing a single number to characterizes the radiation field (referred to here as the radiation reference). Over the course of a simulation, we can then calculate an equivalent reference number as the sum over frequency groups of the weighting number multiplied by the simulated radiation energy density in that frequency group. For a given temperature and density, the simulation parameters needed can then be interpolated between the two closest adjacent tabulated radiation fields based on these radiation reference numbers. It should be noted that, in general, a simulation temperature and density point will not fall directly on tabulated values, so this process is repeated for the nearest neighbor points to provide results that interpolate in temperature density space as well.

Finally, since this approach uses a fairly low number (2-10) of coarsely binned frequency groups to both characterize the radiation field and transport energy, details of the emergent spectra need to be assessed in a post-processing step. Here, we use the complementary non-LTE tables of spectrally resolved emissivities and opacities that are produced at the same time as the main reference tables on the same temperature, density, and characteristic radiation field points. In Gorgon, the emergent spectra are reconstructed by ray tracing through the simulation grid parallel to the line-of-sight (x) axis for every point in y, and then summed over y. For each frequency point ν in the spectrum, each ray integrates the time-independent transfer equation $I_\nu^x = I_\nu^{(x-1)} e^{-k_\nu^x \Delta x} + (j_\nu^x / k_\nu^x)(1 - e^{k_\nu^x \Delta x})$ as it crosses the uniform-Δx grid, using frequency-dependent absorption opacities $k_\nu = \kappa_\nu / \rho$ and emissivities j_ν interpolated from the spectrally resolved data tables. Here, the interpolation for the frequency-dependent quantities is performed in the same manner as for the bulk material properties, using the same weighting technique described above.

3.4.3. Application to a radiating cylinder

The transport and non-LTE table reference method described above is applied to a static aluminum cylinder with a density of 10^{20} ions/cc and T_e =500 eV, where the density and temperature are held fixed and the radiation field is converged to its steady-state value. Two photon energy groups are assumed, spanning 100-707eV (encompassing L-shell transitions) and

707-5000 eV (encompassing K-shell transitions). The atomic model used to generate the tables is the same highly simplified non-LTE model described in [7], with a high ion temperature of 20 keV to account for the motional Doppler broadening typically seen in imploding Z-pinch plasmas. The cylinder is placed in the center of a square grid in the $x-y$ plane spanning -5 mm to 5 mm, evenly discretized into 200 computational cells in each direction. The cylinder axis of the reference case is 1 cm along the z direction, but for this 2-D example the cylinder is assumed to be infinitely long. The free-space mean free path is essentially infinite (assumed to be 5000 m).

Initially, the radiation energy densities in the problem are zero. With advancing timesteps, the self-emission from ions at the fixed plasma temperature and density drives a spatially dependent radiations field (larger at the center of the plasma than at its boundaries) and the system evolves in time to reach a steady state. At these conditions, steady state in the R-MHD code is reached in $t_{eq} \approx 10^{-11}$ seconds (a shorter timescale than the tabulated optically thin collisional equilibration time $t_{ceq} \approx 2 \times 10^{-10}$ s and longer than the radiative equilibration time $t_{req} \approx 3 \times 10^{-12}$ s for an LTE plasma with $T_r = T_e$). Since the angular discretization of this transport method tends to prefer certain directions (most notably the infinite z direction), the angular resolution used (i.e the number of equations solved) is adjusted to converge on a reasonable result for a cylinder with a high aspect ratio ($z \gg r$).

Figure 3-5a shows the converged radiation energy density for the K-shell photon energy group at three different angular resolutions (12, 24, and 48 directions spaced evenly around the azimuth). Ray effects from finite angular resolution are pronounced in the free-space region surrounding the plasma. Obvious errors may be incurred if radiation from this cylinder were heating material surrounding it, which is potentially a concern since we are introducing an explicit coupling between the radiation energy density and various material parameters. For the purposes of this example, 3-5b shows lineouts from the 12 and 48 angle cases taken between ray directions, with an additional lineout aligned with a ray direction for the 12-angle case. Black dashed vertical lines denote the edge of the cylinder. The convergence of the radiation energy density within the plasma region itself is very good (3% at the cylinder boundary), with transport differences largely isolated to free space outside the source.

Our reconstruction of an emergent spectrum from the 48-angle calculation is shown in fig. 3-6a, focusing on the He_α and Ly_α aluminum lines. Finite-length and Lambertian (surface integration) corrections are not included at this stage, so we are not attempting a direct quantitative comparison with NRL benchmark results [7], but we can examine relative changes from different non-LTE radiative coupling assumptions. The red lines show spectra from a calculation where emissivities and opacities are generated in the zero-radiation field limit, illustrating the profound effect of self-photopumping on the line intensities. The associated changes in the radially dependent K-shell-group radiative energy density are shown in 3-6b, and the radially dependent Plankian opacity absorption coefficients are shown in 3-6c. For problems of this type, these

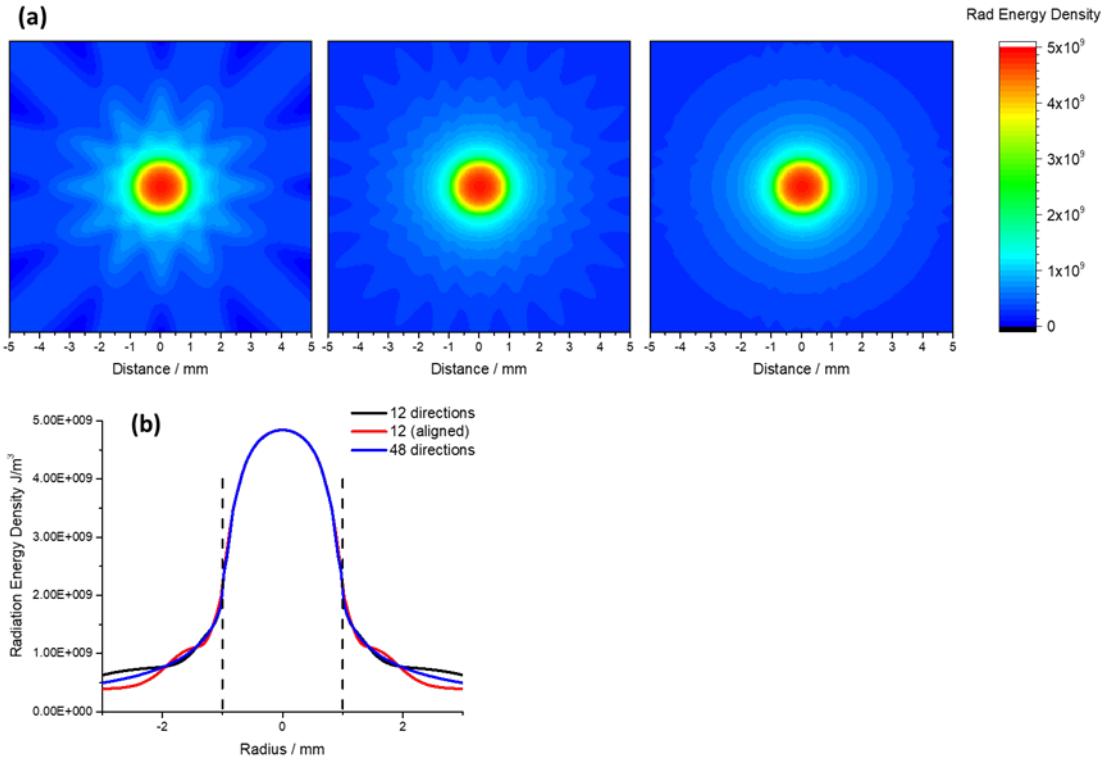

Figure 3-5 (a) steady-state K-shell group radiation energy density for a uniform plasma cylinder of aluminum with $n_i = 10^{20}$ ions/cc and $T_e = 500$ eV [7] using 12, 24, and 48 rays for radiation transport. (b) lineouts of radiation energy density from the 12-angle case aligned (red) and between (black) rays, and from the 48-angle cases between rays (blue); black dashed lines denote the edges of the plasma cylinder.

results illustrate the large differences in material parameters that can result from neglecting feedback between the plasma and radiation field, and the correspondingly large differences that can then result in the established steady-state radiation fields.

With respect to the transport method, we have shown that convergence of the free-space radiation energy density distribution is achievable with high angular resolution. However, this comes at the cost of dramatically increasing the number of equations being solved, and thus increasing the computational expense of the simulations. Ideally, the tabular reference steps of this method could be applied independently of the radiation transport scheme being used. In such a scenario, the biggest gains to improving the feasibility of large scale non-LTE radiation transport calculations would result from pairing the tabular approach with the simplest possible transport scheme. In practice, this can be problematic. To illustrate the issues, we can contrast the approach just described with the automatic flux-limiting diffusion solution previously discussed.

Neglecting for the moment the non-LTE feedback between plasma and radiation field, we can examine a radiating cylinder in the limits of it being optically thin, or optically thick, and compare the results from the two different transport methods. Here, we use only a single radiation group

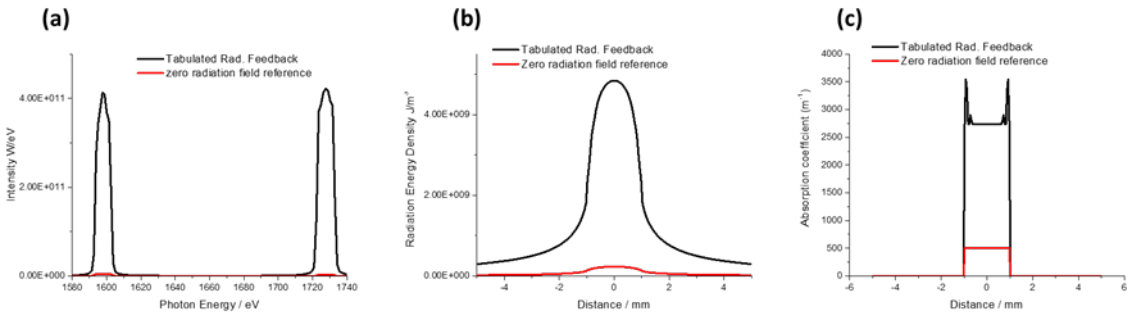

Figure 3-6 (a) Emergent He_α and Ly_α emission lines from the converged 48-ray case described in fig. 3-5 (black) compared to a calculation that transports the optically thin ($T_r = 0$) emission through the same cylinder (red). (b) Radial dependence of the K-shell radiation energy density in the converged 48-ray and optically thin cases. (c) Radial dependence of the K-shell Planckian absorption coefficients for the two cases.

but stay with the same 2 mm-diameter radiating cylinder on a square, 10 mm, 200-cell simulation grid. We again initialize the radiation energy density at zero, holding the material temperature and density fixed so that the radiation field can evolve to a steady state. In the optically thick case, we define a plasma electron temperature of 100 eV and a mean free path within the plasma of 10 μm (less than the 50 μm simulation grid cell size). Here, we assume an opaque plasma in LTE at $T_e = T_r = 100$ eV, deriving the emissivity from the opacity and the Planckian blackbody function B: $j(\nu)/k(\nu) = B(\nu)$. For the diffusion solution, the surrounding "free space" is assigned a mean free path of 1 cm, while for the high-fidelity transfer equation solution, the free-space mean free path is again essentially infinite (5000 m). Figure 3-7 shows the magnitude of the radiative flux between the two cases alongside lineouts along the x-axis through the center of the grid. These lineouts are compared to the analytic solution to the flux expected as a function of radius from a 100 eV surface emitter.

Switching to an optically thin radiation source of the same dimensions and temperature, we set a uniform plasma emissivity such that our 2 mm-diameter cylinder is volumetrically emitting 1 TW/cm. The mean free path is set everywhere to 1 cm in the diffusion case and 5000 m in the radiative transfer case. Figure 3-7 again shows comparison plots of the magnitude of the radiative flux and lineouts compared to the analytic expectation.

In each of these limiting examples, both the transfer equation solution and the diffusion solution produce equivalent results for the flux of radiative energy away from a cylindrical source. Both methods are explicitly integrating equations on speed-of-light timescales, but where the transfer

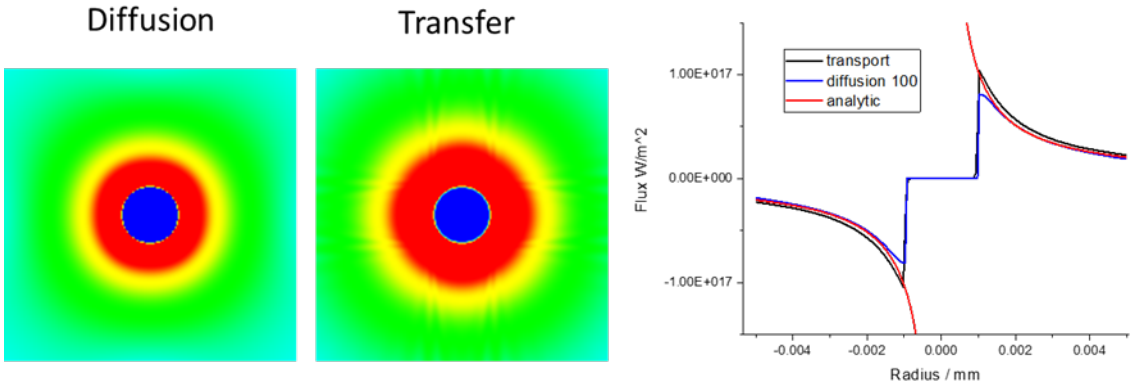

Figure 3-7 Left: Radiation fields from the diffusion and full radiative transfer solutions for an opaque (LTE) plasma. Right: lineouts of the radiation fields along the x axis from the two radiation transport approaches, compared with the analytic solution (red).

equation solves 48 equations, the diffusion solution solves 2. This represents more than an order of magnitude difference in computational cost (significantly more in 3-D) making the diffusion solution very attractive for this type of problem. Furthermore, the equivalence of the radiative fluxes demonstrates how simple diffusion approximations can accurately transport energy in situations where details of the directionality of the radiation are less important. However, if we now scrutinize the equilibrium radiation energy densities reached in these two cases, significant discrepancies do exist, as shown in fig. 3-9.

For the opaque cylinder, both solutions obtain the correct LTE radiation energy density within the plasma as shown in 3-9a, but the drop-off in the surrounding free space differs. This effect is more insidious in the transparent radiating cylinder shown in shown in 3-9b, where we contrast the transfer equation solution with two diffusion solutions assuming different free-space mean free paths (1/300 m and 1/200 m). In the transfer solution, the steady-state radiation field in free space is such that the radiative flux is directed away from the source, given by $F = cE$. This simply states that the flux is propagating the radiative energy at the speed of light, as expected. However, for the steady-state diffusion solution, the radiative flux corresponds to $F = -(c/3\kappa)\nabla E$, so the gradient of the energy density that supports the flux is dictated by the mean free path assigned to free space. The outermost boundary condition, combined with this required free-space gradient, then dictates the energy density at the plasma surface, which in turn dictates the energy density within the plasma. Said another way: in a diffusion approximation, the correct transport of energy specifies what the gradient of the radiation energy density must be, so its magnitude is not well constrained. Instead, it is set by a combination of the boundary condition and the free-space opacity.

Some of this ambiguity can be removed by using an extrapolated length or extrapolated end-point boundary condition (as used here). In this approach, which is commonly used to model moderator

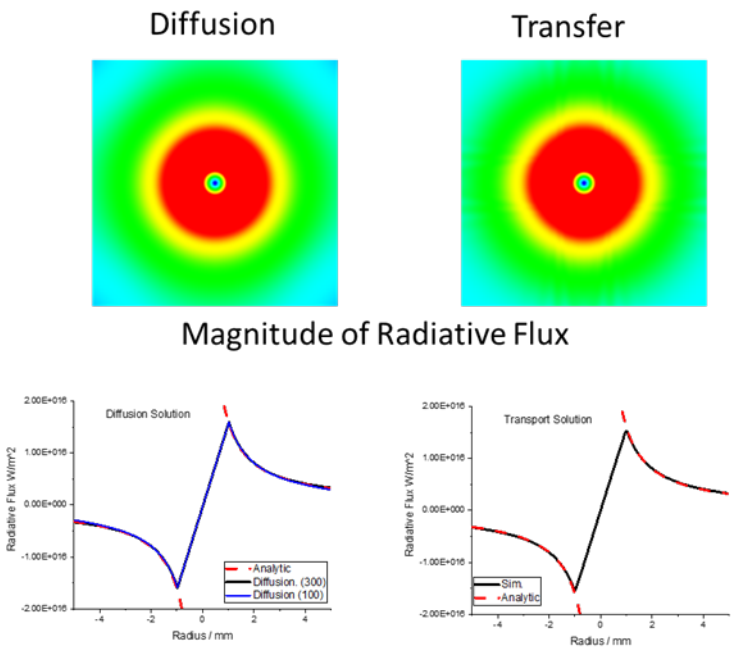

Figure 3-8 Top: Radiation fields from the diffusion and full radiative transfer solutions for an optically thin plasma. Bottom: lineouts of the radiation fields along the x axis from the two radiation transport approaches, compared with the analytic solution (red).

boundaries in neutron diffusion problems, the diffusive flux is assumed to extrapolate to zero at a distance from the boundary set to be 0.7104 times the mean free path. This makes the boundary value of the radiation energy density an unambiguous function of the free-space opacity. However, it does not resolve the problem that the value chosen for the free-space opacity now dictates the radiation energy density within the transparent plasma. The fact that a diffusion approximation can be problematic for optically thin plasmas radiating into free space is hardly surprising, since the assumption of an isotropic radiation field that underpins the diffusion approximation clearly breaks down in this situation. It is, however, critical that if we primarily care about the transport of energy through a distribution of plasma and out into free space, the radiative flux is accurately recovered. As such, there are many situations where a diffusion approximation can provide very reasonable results at low computational cost.

In traditional calculations, where plasma parameters are functions of only density and temperature, a diffusion approximation can accurately transport energy that heats or cools a material. Unfortunately, for our non-LTE radiation transport application, calculating the non-LTE emissivity and opacity coefficients requires knowledge of the absolute magnitude of the radiation field using low-fidelity transport methods like the diffusion approximation may incur errors. For transparent plasmas, these errors could be significant – however in that case, the coupling between the radiation field and plasma may be less important. For plasmas of moderate optical

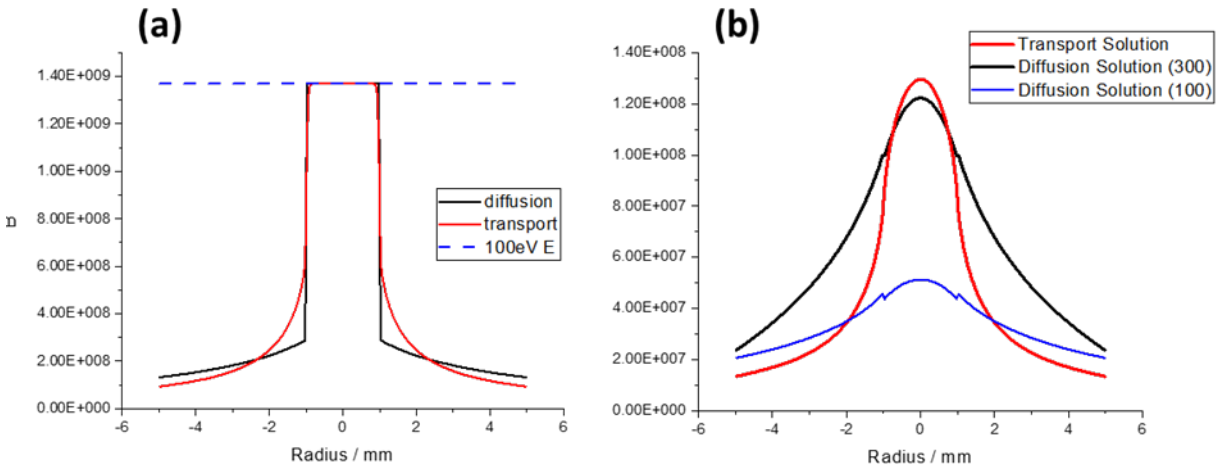

Figure 3-9 (a) Radial dependence of the radiation energy density in an opaque (LTE) cylinder using the diffusion approximation (black) and full radiation transport (red) (b) Same, but for the optically thin case with two different assumptions for the free-space mean free paths in the diffusion approximation.

depth, the errors are less pronounced. To emphasize this point, we return to the aluminum cylinder transport test case, coupling the diffusion transport method to the non-LTE tables. Figure 3-10a shows the equilibrium K-shell radiation energy density from the transfer equation solution compared to the diffusion solution, again using two different free-space mean free paths (as for the transparent plasma case). Also shown are the K-shell plasma absorption coefficients. Since this plasma has a moderate optical depth (mean free path of ≈ 0.4 mm and peak line-center optical depth of $\tau \approx 100$), the radiation energy density is maintained by the plasma instead of just the diffusion-limited rate at which radiation can be transported. As such, discrepancies between the transfer equation solution and diffusion solution are smaller (<10% on axis). The corresponding differences in the non-LTE equilibrium opacities and emissivities are then negligible, as illustrated in fig.3-10b.

The comparisons shown emphasize that accurately capturing non-LTE physics is intertwined with the accuracy of the radiation transport method – that is, the accuracy with which the radiation energy densities are calculated. This is dependent on the type of underlying radiation transport scheme as well as the angular resolution of a given scheme. It is tempting to regard parameters derived from atomic physics or material models as values that a simulation can simply utilize: data that is agnostic to the algorithm into which it is dropped. However, when plasma parameters become a function of the radiation field, an additional burden is placed on accurately calculating that radiation field. Simple diffusive transport methods may be sufficient for opaque plasmas, or plasmas of moderate optical depth. However, as a radiating plasma becomes more transparent, the diffusion approximation can incur significant errors. When coupled to tabulate non-LTE data, these errors may have an outsized effect as they feed back into other plasma parameters. The two transport schemes developed here, both coupled to the non-LTE tables developed for this LDRD, provide a toolset that can be used to further explore the limits of simpler transport algorithms in

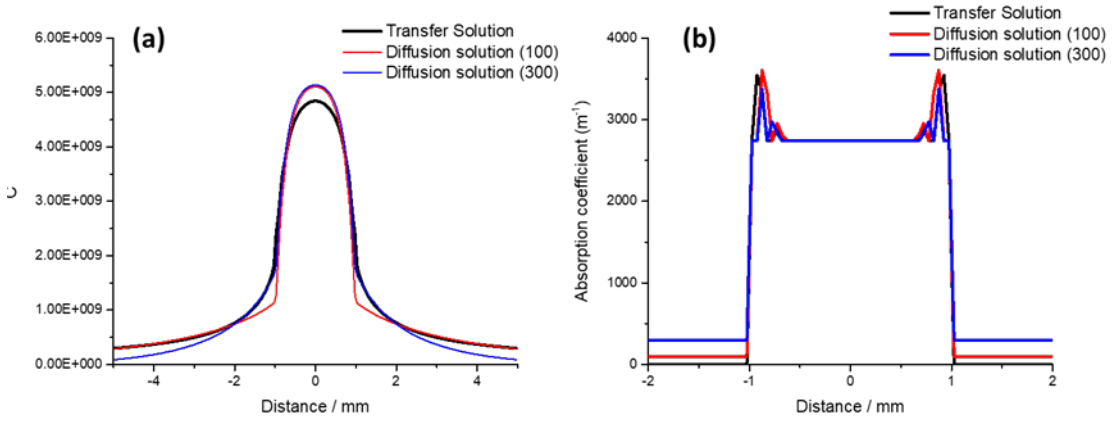

Figure 3-10 Returning to the uniform aluminum cylinder test case: (a) Radial dependence of the radiation energy density using the full radiation transfer solution (black) compared with the diffusion approximation with two different assumptions for the free-space mean free paths. (b) A comparison of the radially dependent absorption coefficients from the same calculations.

modeling non-LTE plasmas.

3.4.4. MHD applications, consistency, mixtures, and stability

Despite some shortcomings of the radiation-group diffusion approximation for capturing non-LTE processes, it is robust and fast to run. When prudent choices are made for boundary conditions and/or free space mean free paths , the resulting radiation fields used for interpolation on non-LTE tables can be quite reasonable. An informed radiation-group diffusion approach is thus sufficient to test and develop techniques for incorporating tabular non-LTE physics into broader resistive-MHD calculations. And the lessons learned here can later be transferred to simulations using higher fidelity (and more expensive) transport algorithms.

Once we have relatively reliable estimates of the radiation fields, we can reference the full extent of tabulated non-LTE data described in Chapters 2 and 3 within a more complete R-MHD code. Here, a pre-processing step on the non-LTE tables was found to be helpful in referencing and checking tabulated data: pior to starting a simulation, the table is broken up into a selection of sub-tables loosely organized by the physics module they will be used in: EOS, transport, and radiation physics. The radiation field weighting numbers used in the table lookup are also pre-computed and stored in their own table. While the ultimate intention is to unify all of the support models to use the self-consistent non-LTE data produced by the atomic-scale codes described in this LDRD, we find that the SCRAM- and SCFS-based tables used to develop our tabular strategy are often not sufficiently accurate (see the light gray lines in figs. 2-2 and 2-3 as exemplars). Thus, for many applications it is desirable to swap in existing tabulated data. For example, some applications rely on specific EOS or conductivity models. Subdividing the

SCRAM/SCFS tables makes it easier to be selective on which tables to include, whilst reducing redundant memory storage and constructing smaller arrays that are faster to search through.

Extending the use of the non-LTE tables to incorporate fully consistent EOS and transport data will become more feasible with tables generated from the DFT-AA code described in Chapter 2, especially when those data are adjusted to match reference data and selected DFT-MD or TDDFT calculations (as the current trusted tables have been). The the various points within a calculation where material or transport parameter references are made are described above. At its simplest, these reference calls can be made directly to the non-LTE tables. Most of the material and transport parameter references are made at the start of the simulation timestep loop, so can simply be made using the radiation field present at the end of the previous timestep.

The notable exception to this involves assessing the plasma temperature: The primary variables tracked within a calculation are density and material energy density. Assessing the plasma temperature then requires working out which temperature results in an energy density consistent with that present in a simulation. The tables list quantities of interest as a function of temperature and density, but for a given temperature and density, the energy density returned now depends on the radiation field. As described previously, an iterative procedure is used to search through temperature space to find the consistent energy density. This search now must be modified as the weighting numbers used to evaluate a radiation reference number are themselves a function of density and temperature. As we go through successive temperatures in the search routine, the radiation field weighting numbers are changing. Thus the radiation reference needs to be continually re-evaluated to perform the table lookup. This is straightforward – and when implemented can be robust – but it does increase the complexity and time taken by the EOS reconciliation step. This partly drove the need to break up the main non-LTE table into a set of targeted sub-tables for faster/simpler reference. Newton-Raphson style iterations are appealing to speed up this lookup process, but the extra degree of freedom introduced by the radiation field make these methods less reliable in converging on the consistent temperature. A brute force table search on a diminishing change in temperature is found to be more robust (but more costly). Here, robustness is preferable, as temperature is used in referencing many subsequent parameters and errors in temperature can quickly terminate a simulation.

An additional modification to the non-LTE table lookup accounts for the presence of multiple materials (mixtures) within a simulation. For a given simulation, the SCRAM/SCFS tables for different materials presently need to be generated with the same photon energy group structure on the same temperature and density grid. Care must be taken when multiple materials are used because the total number of radiation reference fields that SCRAM computes may differ between materials. This sets the order of interpolation. At a given location in a simulation, the photon energy group weights are first referenced separately for each material. These are then combined into a single set of group weights by weighting each individual material value with its mass fraction at that location. A radiation reference number is then computed using these weights and the radiation energy densities present in the simulation. This reference number is then used to interpolate parameters of interest based on the radiation reference field for each material separately. This is repeated for each of the 4 temperature/density points surrounding the target density and temperature. Interpolation in density/temperature space is then performed for each separate material before the resulting quantities are combined into a single value. For simplicity, a

mass fraction weighting is presently used to combine different material values, although this needs to be revisited.

Finally, we remark on the stability of the implementation of non-LTE material and radiation models. A desirable aspect of a self-consistent non-LTE implementation is incorporating the feedback between the material equation of state, material conductivity, and the evolving radiation field. Pulsed power-driven experiments can, however, create unique conditions that complicate how this feedback is implemented. We are often interested in cylindrical systems that are accelerated towards their axis of symmetry by a $j \times B$ force resulting from an applied current. Taking for example an argon gas puff radiation source, the current first begins to flow in low-density material on the outermost surface of a cylinder of argon gas; the resulting magnetic force is directed radially inwards to compresses material; and that material begins to radiate as it is accelerated to high velocity. Ultimately, the material stagnates on its axis of symmetry, thermalizing its accumulated kinetic energy to produce a high-temperature, high-density, strongly radiating column. The current driving these implosions is mainly carried in a layer on the outermost surface that is subject to the rapid development of magneto-Rayleigh-Taylor instabilities. This unstable current carrying plasma surface is surrounded by a region of current free "vacuum," and MHD modeling therefore requires modeling the plasma at a vacuum-plasma interface where material is transitioning to a very low density. This presents a problem for most MHD algorithms. The typical approach is to define a density threshold, or "florr" (normally about 10^{-5} g/cc), below which heating and acceleration terms within a plasma are turned off. Electrical resistivities are also pushed high enough to prevent material carrying a meaningful amount of current. Choices in exactly how this is done vary between codes and can substantially affect the predictions of a given code.

A non-LTE treatment adds an additional complication, since low-density material can now respond directly to non-locally driven variations in the radiation field. Radiation passing through does not need to be directly absorbed by a low-density plasma for changes in material pressures and ionization states to result. These changes can then directly alter plasma dynamics, heating rates, and electrical conductivities in the vacuum-plasma transition region where MHD codes already struggle. Simulation results then become prone to non-physical oscillations in temperature and pressure that couple through the radiation field. In many HED systems, this would amount to some undesirable noise in low-density material that is inconsequential to the plasma dynamics being studied – that is, to fluctuations that lack the energy to meaningfully impact denser plasma. However, in an MHD simulation, oscillations driven at the vacuum-plasma interface can influence the distribution of current and quickly feed back into the broader MHD solution.

In many respects, capturing the feedback between the plasma and radiation field is the purpose of including a self-consistent NLTE model. However, our implementation has so far assumed this feedback is instantaneous for all plasma densities. In reality, a tenuous, low-density plasma will take a finite time to respond to changes in a radiation field. To capture this, an additional radiation equilibration time,τ_{req} is tabulated as part of the non-LTE data output that can be referenced in the same way as other variables. To utilize this finite equilibration time in a simulation, an additional set of radiation energy densities are defined. Referred to as the material radiation energy densities, these are calculated as:

$$E_{mat} = E_{mat}\mathrm{e}-dt/\tau_{req} + E(1 - texte-dt/\tau_{req}) \quad (35)$$

Where E_{mat} is the material radiation energy density and E is the primary radiation energy density that the simulation already solves for. This equation is repeated for each of the photon energy groups used in a calculation. The material field now asymptotes to the primary radiation field over a characteristic timescale set by the equilibration time. The update of equation 35 is performed immediately after the primary radiation fields are updated at each simulation timestep. When radiation is advected by opaque media, both of the energy densities are advected in the same way. When equilibration times are short, the material radiation field becomes a copy of the primary radiation field. Otherwise, a lag is introduced before changes to the primary radiation fields can affect the material fields. For the purposes of all material references from tabulated data, this new material radiation energy density is now used. For transport, absorption and emission processes the primary fields are still solved for as before. This approach effectively decouples the material reference steps from rapid changes in the radiation field. Feedback between radiation and material is no longer instantaneous but occurs on a physically motivated timescale that captures that rate at which a plasma can realistically respond. This approach has been found to successfully stabilize the low-density vacuum-plasma transition issues highlighted above and is key to implementing this non-LTE tabulated radiation treatment in multi-physics R-MHD calculations. Further testing of this scheme and detailed comparisons with existing non-LTE radiation treatments in simulations of pulsed power-driven experiments is the subject of ongoing work.

4. POST-PROCESSING

Spectroscopic analysis is an important tool for REHEDS plasma diagnostics that relies on accurate atomic-scale models to predict detailed and reliable emission and absorption spectra. Traditionally, spectroscopic analysis in an inverse problem: we measure an emission, absorption, scattering, or fluoresence spectrum and ask what it can tell us about the source plasma that produced it. For example, observing He-like Kr emission from a MagLIF target whose D_2 fuel was doped with Kr tells us something definitive about the temperature of the fuel conditions at stagnation, since ionizing Kr to He-like configurations requires exceeding a certain temperature. Measuring He-like Fe emission from the same target tells us that there is some amount of mixing between the cold confining Be liner (with known Fe impurity fractions) and the hot fuel [135]. And measuring fluorescence emission from near-neutral Fe in the same target tells us something about the conditions of the bulk/unmixed liner at the time of stagnation [100]. Together – and with additional data from neutron and time-resolved x-ray power diagnostics – these observations can significantly constrain our understanding of the MagLIF plasma at stagnation. Similarly, combining analysis of L- and K-shell emission spectra with power and imaging diagnostics from an imploding wire array can tell us a lot about implosion velocities and temperature gradients around the time of peak emission [120]. We can use these spectroscopic inferences about plasma conditions to help assess the predictive power of our R-MHD simulations by comparing the inferred plasma properties to timing, temperatures, densities, and mix parameters extracted from the simulations. However, there are often questions about both 1) the uniqueness of the inferred

parameters from experimental data and 2) the suitability of the extraction methods from simulations to provide equivalent parameters (e.g. emissivity weighting functions).

In principle, we can avoid the questions associated with both model inversion and data extraction by directly comparing experimental data to synthetic observables produced by post-processing our simulations. This requires not only accurate and detailed atomic-scale model predictions of observables at local conditions and flexible tabulation schemes that capture a wide range of local conditions, but also the ability to generate integrated synthetic data that incorporate target-scale phenomena including the effects of non-local radiation transport, significant spatial and temporal gradients, and even the instrumental responses of the various detectors.

Thus, our ability to perform integrated forward calculations that produce detailed synthetic data is a key component of assessing predictive capability for REHEDS simulations. This chapter describes two efforts performed under the LDRD to leverage the significant advances described above in 1) the accuracy and internal consistency of atomic-scale models and 2) the development and implementation of a generalized scheme for tabular non-LTE to help advance our third research focus: 3) to produce useful tools that generate synthetic data suitable for direct comparison with experimental measurements.

First, we describe a 1-D cylindrical radiative transport and post-processing tool that uses the tables described in section 3.2 to generate self-consistent radiation fields and synthetic source output spectra. This tool (which goes beyond the original scope of the LDRD) captures non-local radiation effects and gradients from simplified representations of Z-pinch plasmas, enables us to test interpolation and radiative transport schemes, and independently generates self-consistent non-LTE spectra suitable for comparison to processed experimental data. Next, we describe a new approach to comprehensive 3-D modeling that can link directly to R-MHD output, generate source spectra with (for now) simple line-of-sight transport on the non-LTE lookup tables, and produce synthetic detector data for power, imaging, and spectroscopic diagnostic using rigorous ray-tracing and instrument response models. Together with the internal post-processing capabilities of Gorgon (described in section 3.4, these tools provide several powerful options for practical testing and utilization of the LDRD's fundamental achievements in atomic-scale modeling and non-LTE tabulation.

4.1. Cylindrical plasma model with self-consistent radiation transport

In this section, we describe a 1-D code developed under the LDRD that reads in non-LTE tables and simplified plasma conditions, performs interpolation and self-consistent radiative transport calculations, and generates synthetic emission spectra suitable for direct comparison with processed experimental data. Since the natural geometry of most Z-pinch REHEDS target plasmas is cylindrical, we restrict the code to cylinders, distilling the often complex spatial gradients of a Z plasma to azimuthally and axially averaged values. Our work here is modeled after the tabular non-LTE capabilities described in [120], but is much more efficient and slightly more general, as it can model photoionized and fluorescing plasmas as well as optically thick line radiation sources (although it so far excludes the Doppler velocity shifts considered in [120]).

The input file specifies a cylinder height h, radius r, the plasma material (non-LTE table name), and the electron temperature and electron (or ion) density gradients as a function of the radius. For now, the code is restricted to single material tables, though its extension to internally calculated mixtures should be straightforward (see section 3.4). The input file also specifies a number of radial divisions, n_r that, along with the radius, determine the spatial resolution (cell size) of the imposed cubic Cartesian volume elements. Finally, it specifies choices for a (very) limited number of interpolation and non-local radiation transfer options.

The code then reads in both the coarse-radiation-bin main tables for the given material and the accompanying tables of high-resolution emission and absorption spectra, and stores those data in flexible allocatable arrays. It sets up volume elements (cells) along the radius of the plasma, assigns temperatures and densities to each cell, and interpolates the $T_r = 0$ points of the non-LTE tables on T_e and ρ (or n_e) to estimate the emission and absorption properties of each cell. This gives an initial estimate for the radiative properties of the cylindrical plasma.

If the self-consistent radiation field loop is not invoked, the code can now generate radially resolved and/or spatially integrated synthetic source spectra by transporting $T_r = 0$ interpolations of the detailed (frequency-resolved) emissivities j_ν and absorption coefficients k_ν along detector lines of sight in the x-direction (perpendicular to the axial z-direction) accumulating intensities I_ν from the back ($i = -n_r$) to the front (detector side, $i = n_r$) of the cylinder:

$$I_\nu^i = I_\nu^{i-1} e^{-k_\nu^i \Delta x} + (j_\nu^i / k_\nu^i)(1 - e^{k_\nu^i \Delta x}). \tag{36}$$

For optically thick plasmas, however, this simple approach can be catastrophically wrong, since it accounts only for the absorption of photons and ignores the photopumping excitation that necessarily accompanies each absorption event (see fig. 3-6). Thus, we must move away from the $T_r = 0$ assumption and perform self-consistent radiation transport calculations that account for the effects of the incident radiation fields on each cell from all other cells in the plasma.

As described in section 3.4, the angular resolution of the radiation transport algorithm is a key determinant of a transport calculation's accuracy, especially at the edges of the plasma and just outside the plasma boundaries. In this simplified post-processing code, however, we consider incident radiation from only the 6 angles aligned with rays perpendicular to the face of each cubic spatial cell. In the directions perpendicular to the z-axis, we compute the accumulated incident radiation on each cell inward from the plasma boundary, using the radiative transfer expression for I_ν given above with $\Delta x = \Delta y$. We also include self-photopumping within each cell, using $\Delta x_{self} = \frac{1}{2}\Delta x$. To mitigate the overweighting of the $\pm z$-directions for long cylinders with high aspect ratios ($h >> r$), we average the mean chord of the plasma sky at each radius to obtain a Δz that is $h/2$ only in the limit of a squat cylinder ("pillbox") and approaches $\sqrt{2}r$ for the cell at the center of a long cylinder ("pencil"). This is a simplified "long characteristics" treatment of radiation transport. [16] Here, the transport is performed on the coarse radiation bins using the

[16] We have also attempted a "short characteristics" treatment of radiation transport, similar in spirit to the diffusion approximation described in section 3.4, where the input radiation to each cell is calculated only from itself and the immediately adjacent cells. However, we found a a strong (and unsurprising) dependence of that method on the cell size and have not yet implemented the characteristic mean free paths described in section 3.4, so we do not report those results here.

opacity factors f_k described in section 3.2 to help capture line-dominated radiation transport.

Given these rough but reasonable representations of the radially dependent incident radiation fields, we can recompute the coarse-binned emissivities and absorption coefficients by interpolating the non-LTE tables on the radiation field (as well as temperature and density). This gives us new emissivities and absorption coefficients that, in turn, affect the calculation of the incident radiation field on each cell. To reach the self-consistent steady-state solution, we iterate the procedure until the coarse-binned radiation fields converge to a constant value. When convergence is achieved, we can proceed with the line-of-sight transport described above, interpolating the high-resolution emissivities and absorption coefficients on temperature, density, and the converged radiation field to obtain both radially resolved and surface-integrated source emission spectra that are suitable for direct comparisons with experiment. These spectra will include the effects of non-local radiation transport as well as line-of-sight absorption and even fluorescence through radial temperature and density gradients.

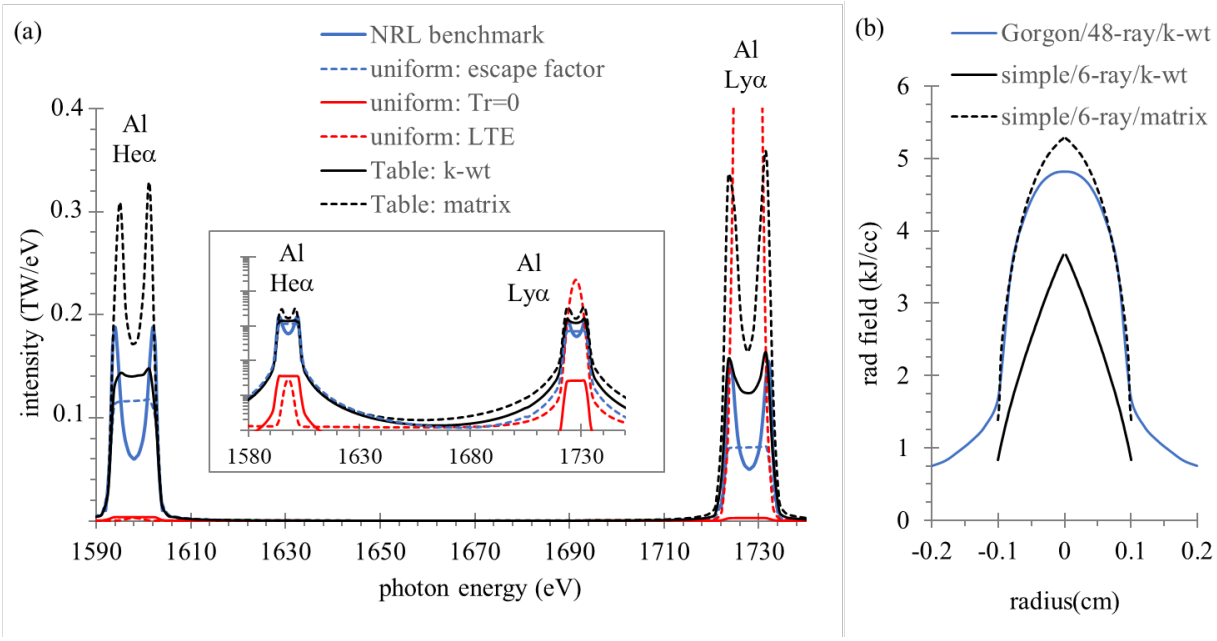

Figure 4-1 (a) emergent K-shell emission spectra from our simple cylindrical radiation transport tool using non-LTE tables and two different interpolation methods (black and black dashed) compared with a benchmark calculation [7] (solid blue) of a uniform plasma cylinder of aluminum with $n_i = 10^{20}$ ions/cc and $T_e = 500$ eV. Also shown are the uniform-plasma $T_r = 0$ and LTE limits (red and red dashed) and the escape-factor method (blue dashed) (b) The radial dependence of the K-shell group radiation energy density from the cylindrical tool for the same case, with the two interpolation methods, compared to calculations from Gorgon.

We use this simple 1-D cylindrical radiation transfer model to test both the table interpolation and radiation transfer schemes. As in section 3.4, our test case is the benchmark K-shell aluminum cylinder described in Apruzese et al. [7]. Here, a uniform cylinder of aluminum with $h = 1$ cm, $r = 1$ mm, $n_i = 10^{20}$/cc, $T_i = 20$ keV (to mock up Doppler broadening from an imploding plasma), and $T_e = 500$ eV is radiating with its converged (steady-state) radiation field. In the benchmark calculations, a very simple non-LTE atomic model with only about 10 electronic states is fully coupled to a high-resolution multi-frequency and multi-angle radiation transport algorithm. That is, for each cell in the plasma, the detailed spectrum of incident radiation is calculated and used to drive the full (if simple) collisional-radiative atomic kinetics calculation. In the benchmark calculation, the plasma is divided into logarithmically spaced regions of the peak-line optical depth, τ, so that both high-opacity and low-opacity regions are well modeled. Despite the simple atomic kinetics, the sophisticated radiation transport makes the benchmark model a non-trivial effort. It predicts high radiation fields in the center of the plasma that drive photoexitation of He- and H-like ions as well as photoionization processes, increasing both the excited-state populations and the the H-like population relative to their optically thin values. In the low-opacity regions at the plasma edges, the radiation field has much less impact. This radial intensity gradient leads to profound line-center absorption (self-reversal) signatures in both the He- and H-like lines.

The benchmark calculation serves as an excellent test case for both our tabular non-LTE approach and our radiation transfer algorithms, because we can build non-LTE tables that use the same simplified atomic physics as were used in the benchmark calculations. Figure 4-1a shows the emergent K-shell spectrum from the benchmark calculation along with the predictions of three uniform-plasma approximations and our simple cylindrical model with $n_r = 50$ and the two interpolation schemes described in section 3.3. While the $T_r = 0$ uniform-plasma approximation (solid red lines) (*c.f.* fig. 3-6) and the LTE approximation (dashed red lines) predict line intensities that are orders of magnitude away from the benchmark result in critical regions (as shown in the log-intensity inset), the escape-factor method accounts reasonably well for photoexcitation and photoionization. It gives integrated line intensities within a factor of two of the benchmark calculation, but without self-reversal in the detailed spectra. The cylindrical model with tabular data and radiation transport recovers line-center absorption and, more importantly for REHEDS applications, gives integrated line intensities within a factor of two of the benchmark and reasonable H-like/He-like line ratios using either of the two integration schemes described in section 3.3.It is important to emphasize that the linear radial (and τ) grid of the simple model has much less fidelity than the logarithmic τ grid of the benchmark calculation, that the 6-angle approximation of the simple model's radiation transport is about 10 times coarser than the benchmark model's angular resolution, and that the coarse-binned frequency structure of our tabulation scheme is *thousands* of times coarser than the high-frequency radiation transfer method of the benchmark calculation, so the reasonable agreement here is encouraging.

Figure 4-1b compares the K-shell-group radiation field intensity predicted from the simple converged cylindrical radiation transport model to the steady-state results from Gorgon's test of the same benchmark case. Here, Gorgon used similar non-LTE tables, a slightly finer radial grid structure, a much finer angular resolution, and a similar k-weighted interpolation scheme. Several things are notable: First, given our relaxed factor-of-two metrics for what counts as adequate for fast non-LTE calculations, both interpolation schemes give reasonable agreement with the Gorgon result. This implies that the Gorgon predictions for the spectrum shown in fig. 3-6 would be as

reasonable as those of the simple transport model shown in fig. 4-1a – certainly they have the same relatively even H-like/He-like ratios. Surprisingly, however, the implementation of the k-weighted interpolation in the simple model gives worse agreement with the k-weighted result from Gorgon, while the matrix interpolation method matches the radial radiation fields from Gorgon quite well. Since Gorgon showed little sensitivity to the number of angles at the plasma center, this is not likely due to the angular resolution. Nor do the results of the simple model change much with an increase in radial resolution. We will investigate this further in future work.

For now, these and other calculations with our non-LTE tables and the simple cylindrical radiation transport model have shown us that the non-LTE tables can provide much better accuracy that either the $T_r = 0$ or LTE approximations for optically thick plasmas, but that the results are fairly sensitive to the radiation transfer scheme, the precise tabular structure, and – critically – to the accuracy of the interpolation method.

4.2. X-ray instrument modeling for direct post-processing

A fast, accurate, and consistent post-processor that can generate synthetic data suitable for direct comparison with experimental data is essential for accurate interpretation of experiments and is a critical piece of the experimental design cycle. In HED experiments, we produce dynamic 3-D plasmas; however, unfortunately, we cannot diagnose these experimental 3-D plasmas directly. Instead, we field various x-ray diagnostics (e.g., imagers, spectrometers, and power diagnostics), measure x-rays emitted from these 3-D objects where the information is partially integrated (spatially, spectrally, and temporally), and try to understand the experimental plasmas indirectly through various x-ray diagnostics. Recently, multi-objective data analyses through Bayesian or chi-square analyses are becoming popular because one can constrain 3-D plasma more rigorously and consistently than by analyzing each one of them separately [136]. However, this is possible only when we have access to a fast, accurate, and consistent post-processor. The accuracy of the post-processor determines the accuracy of our Bayesian or chi-square analysis. Fast calculations are needed since such analyses perform so many forward x-ray-data calculations. Model consistency between various x-ray diagnostics is essential because inconsistency would introduce biases into the analysis and prevent us from providing reliable analysis uncertainty.

Post-processors that provide synthetic data are also a critical part of the experimental design cycle, fundamentally improving experimental design and optimizing data collection. A contemporaneous SNL LDRD led by Patrick Knapp, “Developing and Applying Quantifiable Metrics for Diagnostic and Experiment Design on Z” (project: 222431) aims to develop a capability for optimizing diagnostic configurations using Bayesian optimization. If successful, this technique can significantly reduce experimental trials and errors and come up with optimal experimental configurations prior to the first experiments. However, their approach employs multi-objective Bayesian analyses, and thus speed, accuracy, and consistency of any post-processing component are of paramount importance.

Developing a fast, accurate, and consistent post-processor is challenging for multiple reasons. First, x-rays emerging from a 3-D plasma are a result of radiation transport along the diagnostic

lines of sight. How photons are emitted (emissivity) and absorbed (opacity) at each point in a non-LTE source plasma depends on the photon frequency and local temperature, density and radiation field. Second, x-ray data have to be modeled in consistent ways. Actual X-ray diagnostics consist of multiple components such as apertures, crystal, detector, filters, etc, and a consistent and accurate treatment of these components can be challenging. Currently, x-ray-diagnostic models are understood on a case-by-case basis, lacking consistency across various x-ray diagnostics. Third, we must make the tool user-friendly and flexible so that the tool will be actually used by scientists who may not be experts in radiation transport or diagnostic design. For example, the post-processor has to be flexible in the plasma geometry (i.e., temperature, density, plasma composition and their spatial variations), types of input (i.e., HYDRA, GORGON, simplified plasma models, etc), diagnostic lines of sight, and types of x-ray diagnostics. Fourth, these calculations become even more complex when the local radiation field are informed by non-local radiation transport; this requires either input from a rad-hydro code that performs full radiation transport or a self-consistent calculation of the local radiation fields as described in Section 4.1 for a simple cylindrical geometry.

In this LDRD, we developed a versatile post-processor by extending a C++ general x-ray transport model, RADIATOR, developed by T. Nagayama for his Ph.D. work [137], wrapping it into Python, and co-developing each x-ray diagnostic model with the Knapp LDRD. The first challenge, to track line-of-sight emission and absorption for plasmas in LTE, is overcome using the quick table-lookup on temperature and density for local emissivity and opacity developed in RADIATOR. The second challenge, incorporating the elements of actual diagnostics, was addressed by hosting a series of meetings to discuss x-ray data modeling and, resulting in the derivation of a general formula that can model various x-ray data in absolute units [13]. The third challenge, to design a widely usable tool, is addressed by wrapping RADIATOR into python, adding flexibility to read in various hydrodynamic simulation outputs with Polymorphism. The speed of C++ codes and user-friendliness of Python made the tool efficient, flexible, and very easy to use. The tool was modified and incorporated into the Knapp LDRD python tool for Bayesian analyses. The fourth challenge, to incorporate self-consistent non-local radiation transport for non-LTE plasmas, is underway: we have developed and tested key capabilities that will allow us to extend our model to full non-LTE.

Here, we highlight key achievements: (i) efficient and user-friendly architecture, (ii) flexible plasma input formats, (iii) derivation of a general formula for consistent x-ray data modeling, and (iv) designing non-invasive extensions towards developing a fully non-LTE post-processor. One of the main achievements is (iii) derivation of a general formula for x-ray diagnostic instrument response for data modeling, which has been submitted to the Review of Scientific Instruments; see [13] for full detail.

i) Efficient and user-friendly architecture

Efficiency and user-friendliness are essential for our tool to have a long-lasting impact on future research at SNL. This is achieved by wrapping C++ objects (efficiency) into Python (user-friendliness). C++ provides compiled objects, which run 10-100x faster than scripting language like Python. C++ is so-called object-oriented programming. Complex programs are organized into well-defined objects with distinct roles. On the other hand, Python is famous for its user-friendliness and rich and easy-to-maintain libraries. The Knapp LDRD has also developed

general tools in Python, so that wrapping RADIATOR in Python makes our tools accessible to a broad base of potential users and ensures compatibility with other tools.

ii) Flexible plasma input format

Our input tool is made compatible with various radiation hydrodynamic simulation output such as Gorgon 2D, Gorgon 3D, Hydra 2D, Hydra 3D, and a few other custom temperature, density, and composition formats. This is performed by a feature of object-oriented programming called Polymorphism. The main part of the program uses a class called volume to get temperature, density, and composition at (x,y,z) using a function get-condition(x,y,z). This class is an abstract class, meaning that its behavior is not defined in this class. It only defines the function names; their actual behaviors (or implementations) are defined in its child classes. Thus, we create its child classes called Gorgon2D, Gorgon3D, etc and define geometry-dependent get-condition(x,y,z) functions inside these child classes. We also developed a generic 2D cylindrical and 3-D Cartesian classes by working closely with Michael Glinsky, who had already developed python tools to read in HYDRA 2-D and 3-D simulation output. Thus, we can read in HYDRA outputs through his tool and these generic 2-D and 3-D volume child classes. The main program can use get-condition(x,y,z) function without even knowing what the geometry is. We can isolate hydrodynamic-simulation output-format issues to the child classes of volume and separate it from the rest of the coding. With this Polymorphism, we can easily make our post-processor compatible with other hydrodynamic simulation models.

iii) Derivation of a general formula for various x-ray data modeling

One challenge we face in developing a fast, accurate, and consistent post-processor is that, as far as we know, there is no universal recipe that works to predict the output signals of x-ray data collected by the wide range of diagnostic instruments used on a facility like Z. Thus, we don't know how consistent the assumptions and limitations are between two or more x-ray diagnostics. This lack of general understanding of x-ray diagnostics can hinder people from developing good insight into x-ray diagnostics, and the lack of consistent treatment across x-ray diagnostics introduces unknown uncertainty into multi-objective data analysis [136]. We convened a series of meetings with x-ray diagnostic specialists at SNL and successfully derived a general formula that can model various x-ray diagnostics in absolute units. The resulting model would work as x-ray data modeling (forward) or x-ray data processing (inverse). It clarifies implicit assumptions in standard approaches and revealed some inaccuracies in common approaches. Here, we briefly summarize these findings; more details are given in [13].

There are two different types of challenges in developing a general model of instrumental response for X-ray data: (i) geometrical effects and (ii) efficiencies or responses of each component. Photons exiting the source plasma, I_s (photons/s/sr/cm^2/eV), go through the diagnostic and produce detector irradiance, I_d (photons/cm^2 or something similar). This conversion happens due to partial integration of I_s with the influence of three geometrical effects: geometrical dilution of the flux, limited view through the apertures, and the impact of an optic and its geometry. Once we understand these geometrical effects correctly, we face another challenge: the accuracy of various efficiencies and responses such as filter transmission, crystal reflectivity, and detector response. In other words, correct treatment of geometrical effects is necessary but

not sufficient for developing a valid model; the model further requires accurate inputs (i.e., efficiencies and responses) for the computed x-ray data to be quantitatively accurate.

While both aspects are challenging, developing correct understanding of geometrical effects is more fundamental and of paramount importance for three reasons. First, accurate input would be useless without a correct model. Second, good insights into x-ray diagnostics are essential for diagnostic optimization and correct data interpretation; this can be developed only through correct understanding of the geometrical effects. Third, general understanding of the geometrical effects can provide a consistent approach over multi-objective data analysis.

After series of discussions with x-ray diagnostic specialists (M. A. Schaeuble, J. R. Fein, G. P. Loisel, M. Wu, P. F. Knapp, T. J. Webb, W. Lewis, J. Schwarz, R. A. Vesey, and E. Harding), we were able to derive that many x-ray diagnostics including x-ray imagers (TIPC, MLM, etc), spectrometers (TIXTL, TREX, CRITR, etc), and power diagnostics (PCD, SiD, etc) can be modeled in absolute units based on the following formula (see [13] for more detail):

$$I_d(x'',y'') = G_{x''} \int\int \int_{A_{x'',y''}} I_s(E,x',y') R_{\phi x''}(E) F_{x''}(E) dx' dy' dE$$

where $G_{x''}$ [sr/cm$_d^2$] is a detector-position-(x'')-dependent geometrical dilution, $I_s(E,x',y')$ is emergent source spectral radiance [photons/s/sr/cms^2/eV, $R_{\phi x''}(E)$ is spectral-weighting curve due to crystal reflectivity, and $F_{x''}(E)$ is detector-position-dependent efficiencies such as filter transmission, detector response, etc. The integration range $A_{x'',y''}$ is the partial source area seen from detector position (x'',y'') through apertures. After the integrations, this expression returns the detector irradiance in photons/cm$_d^2$.

The derivation reveals a general picture about conversion from source spectral radiance (photons/s/sr/cm$_s^2$/eV) to detector irradiance (photons/cm$_d^2$ or something similar). 1/sr/cm$_s^2$ in the source radiance is converted to 1/cm$_d^2$ in the detector irradiance through the geometrical dilution of the photon flux, G (sr/cm$_d^2$), and the integration over the source area seen through the apertures (cm$_s^2$). The conversion works for pinhole imagers, power diagnostics, and various 1-D slit-resolved spectrometers (e.g., convex/elliptical and reflective/transmissive crystals). Our model naturally accounts for crystal spectral broadening and removes the 1/eV units from the source through integration of E. The derivation suggests that the commonly used crystal reflectivity and spectral broadening widths defined in radians may not be the most rigorous or insightful representation of reflectivity. The common approach could also underestimate the reflectivity and width by a factor of two near the reflectivity edges. We also find that a commonly used, simple method for processing spectral data can introduce inaccuracy not only in the absolute signal level but also in the relative spectral shapes, as illustrated for TIXTL spectrometers in Fig. 4-2. The inaccuracy is introduced by the neglect of space-dependent geometrical dilution and incorrect use of crystal reflectivity.

While quantitative accuracy still requires accurate inputs (e.g., filters transmissions, crystal reflectivity, and detector response), the general recipe described here helps develop a good insight into x-ray diagnostics. This rigorous understanding of x-ray diagnostics is essential even for correctly interpreting calibration measurements such as crystal reflectivity and detector responses. The new model reveals implicit assumptions in common approaches. It is useful for developing

efficient and accurate data modeling ($I_s \rightarrow I_d$) and/or processing ($I_d \rightarrow I_s$) for new x-ray diagnostics. The systematic treatment will also help multi-objective data analyses to return reliable analysis uncertainties.

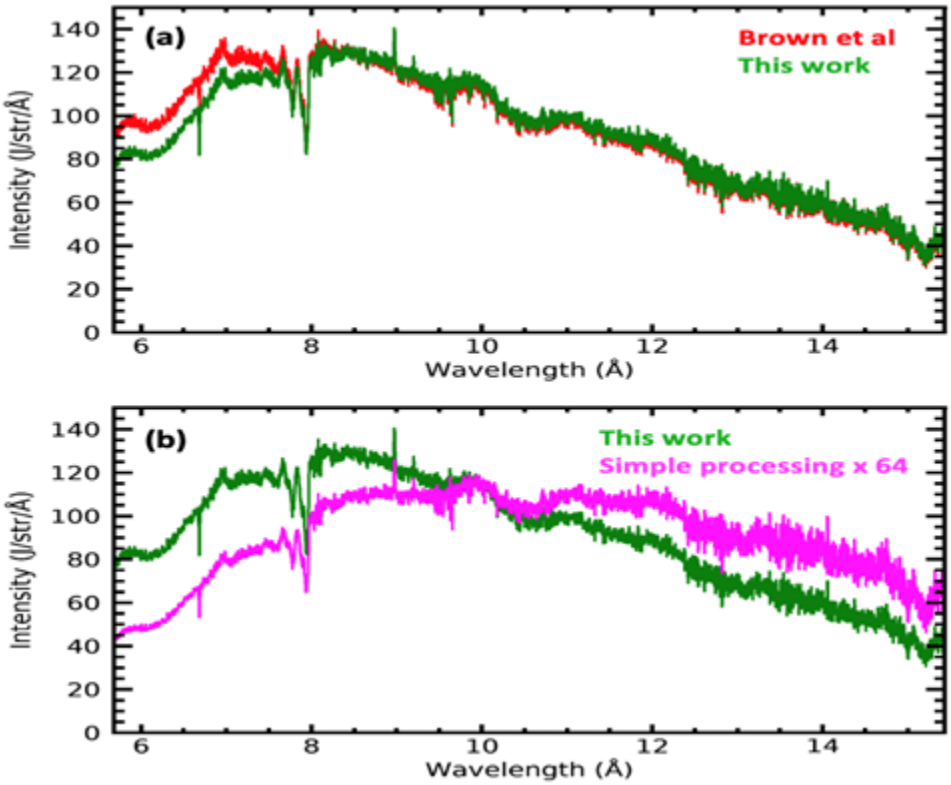

Figure 4-2 (a) The red and green are the SNL Z-pinch spectra processed with Brown's model [Brown et al] and this work. They show excellent agreement both in spectral shape and magnitude. We are still investigating the source of 10-15% disagreement at > 8 Å. (b) Magenta is source spectral radiance with the simple processing method often used at SNL. The resulting spectrum is incorrect not only in magnitude roughly by a factor of 64 but also in spectral shape.

iv) Extensions towards full non-LTE

Finally, we have developed four key functions that are necessary for a fully non-LTE post-processor: (i) read in non-LTE emissivity and opacity tables, (ii) perform radiation transport along multiple lines of sight to compute local radiation field, (iii) perform non-linear interpolation to lookup non-LTE emissivity and opacity based on a given local temperature, density, and radiation field, and (iv) iterate to determine local radiation spatial distributions and non-LTE emissivity and opacity spatial distributions for emergent intensity calculations. These functions were developed and tested to reproduce the proof-of-principle calculations described in Section

4.1. While some of these need to be extended for arbitrary geometry, testing the fundamental algorithms in the simpler geometry allows us to focus on issues purely related to geometry and efficiency for extending the general post-processor to have the non-LTE option. This work will continue under the Knapp LDRD.

5. CONCLUSION

This LDRD successfully advanced and augmented several critical existing modeling capabilities (DFT-AA and TDDFT), developed and implemented two new modeling capabilities (tabular non-LTE and post-processing), and investigated promising new first-principles methods for collisions (see Appendix). These capabilities have already been used in several REHEDS applications both internally and externally, which is partially reflected in the project's publication record of collaborative efforts: (Kraus et al. [18], Strehlow et al. [19], Hu et al. [20], Beier et al. [21], Jiang et al. [22], Kononov et al. [23], Ramakrishna et al. [24, 25]). There are well defined follow-on research directions and follow-on funding to begin executing on them.

Promising future directions for our first research focus area, internally consistent atomic-scale modeling, involve exploring more accurate extensions of or alternatives to TDDFT for calculating equilibrium and non-equilibrium properties, as well as continuing to benchmark and refine our DFT-AA methods against more sophisticated models on a broader space of conditions, including comparisons to new observables and finding novel points of contact with higher levels of theory. In particular, properties related to equilibration processes deserve deeper exploration. We know that collision rates are crucial in determining both equilibrium observables (e.g., conductivities and stopping powers) as well as mechanistic details relevant to establishing equilibrium from a non-equilibrium state. Using this observation to establish a point of contact between DFT-AA and TDDFT may give us more direct methods for improving both. This line of research has already led to multiple publications: Gomez et al. [8, 9, 10], Callow et al. [11], and several more are submitted or close to submission: Baczewski et al. [12], Kononov et al. [14], Hentschel et al. [15], Kononov and Baczewski [16]. In addition to these significant new approaches to dynamic collision and scattering from the DFT-AA model, we plan to publish on our significant advances in self-consistent multiconfguration emission and opacity spectra and our new approach to ion-Stark line broadening.

Our second research direction, developing schemes for tabular non-LTE, has also made significant progress. We have devised a tabular approach for external radiation fields that encapsulates a very wide range of physically plausible radiation fields, including optically thick, fluorescence, and photoionized plasmas. For each of these, we have developed tailored interpolation methods and are working towards improvements of our trial "universal" interpolation schemes. We have also extended our tabular non-LTE capabilities to provide reasonable estimates for detailed fluorescence emission spectra driven by non-thermal ("hot") electrons, a capability that we hope will contribute to Nichelle Bennett's new LDRD on hybrid-PIC-MHD and non-thermal radiation sources. We have implemented these tables in one radiation-magnetohydrodynamics code, Gorgon, where we have addressed several fundamental issues attending non-LTE radiation transport including a novel approach to the stability of the radiation-material energy coupling. We are actively engaged in collaborations with other code developers at Sandia and with scientists at other NNSA laboratories to test and refine our tabular non-LTE approach, and anticipate additional publications on several of these topics.

Finally, we have developed two independent post-processing tools: one that provides self-consistent non-LTE source radiation for Z-relevant plasmas with simple cylindrical geometries, and one that rigorously models the instrument response functions of many actual

diagnostics on Z Nagayama et al. [13]. Both of these tools are already in active use by REHEDS scientists outside of this LDRD, with especially significant applications to radiation effects sciences and deep connections to the data science LDRD led by Patrick Knapp. We expect that this aspect of our work will have increasing programmatic impact as we continue to advance the technical readiness levels of the DFT-AA model and our non-LTE tables.

This project has also strengthened working collaborations within 1600 (1680 and 1640), within Sandia (1600 and 1400), within the DOE/NNSA laboratories (SNL, LLNL, LANL, and LLE), with several universities (Cornell, UNM, UIUC, UT Austin), and with the broader international high-energy density community (including AWE, CEA, and CASUS). We are grateful for and delighted by the opportunities afforded by this funding and look forward to continuing the development and application of the capabilities described in this report.

REFERENCES

[1] H. Scott and S. Hansen. Advances in nlte modeling for integrated simulations. *High Energy Density Physics*, 6(1):39–47, 2010. ISSN 1574-1818. doi: https://doi.org/10.1016/j.hedp.2009.07.003. URL https://www.sciencedirect.com/science/article/pii/S1574181809000834.

[2] H. M. Milchberg, R. R. Freeman, S. C. Davey, and R. M. More. Resistivity of a simple metal from room temperature to 10^6 k. *Phys. Rev. Lett.*, 61:2364–2367, Nov 1988. doi: 10.1103/PhysRevLett.61.2364. URL https://link.aps.org/doi/10.1103/PhysRevLett.61.2364.

[3] A. W. DeSilva and A. D. Rakhel. Progress in measurements of the electrical conductivity of metal plasmas. *Contributions to Plasma Physics*, 45(3-4):236–242, 2005. doi: https://doi.org/10.1002/ctpp.200510026. URL https://onlinelibrary.wiley.com/doi/abs/10.1002/ctpp.200510026.

[4] C. E. Starrett, R. Perriot, N. R. Shaffer, T. Nelson, L. A. Collins, and C. Ticknor. Tabular electrical conductivity for aluminium. *Contributions to Plasma Physics*, 60(3): e201900123, 2020. doi: https://doi.org/10.1002/ctpp.201900123. URL https://onlinelibrary.wiley.com/doi/abs/10.1002/ctpp.201900123.

[5] R. Thiele, T. Bornath, C. Fortmann, A. Höll, R. Redmer, H. Reinholz, G. Röpke, A. Wierling, S. H. Glenzer, and G. Gregori. Plasmon resonance in warm dense matter. *Phys. Rev. E*, 78:026411, Aug 2008. doi: 10.1103/PhysRevE.78.026411. URL https://link.aps.org/doi/10.1103/PhysRevE.78.026411.

[6] S. Hansen, J. Bauche, C. Bauche-Arnoult, and M. Gu. Hybrid atomic models for spectroscopic plasma diagnostics. *High Energy Density Physics*, 3(1):109–114, 2007. ISSN 1574-1818. doi: https://doi.org/10.1016/j.hedp.2007.02.032. URL https://www.sciencedirect.com/science/article/pii/S1574181807000171. Radiative Properties of Hot Dense Matter.

[7] J. Apruzese, J. Giuliani, and S. Hansen. Benchmarking multilevel, 2-d cylindrical radiation transport in a high energy density plasma environment. *High Energy Density Physics*, 8: 231–237, 09 2012. doi: 10.1016/j.hedp.2012.03.005.

[8] T. A. Gomez, T. Nagayama, P. B. Cho, D. P. Kilcrease, C. J. Fontes, and M. C. Zammit. Introduction to spectral line shape theory. *Journal of Physics B Atomic Molecular Physics*, 55(3):034002, February 2022. doi: 10.1088/1361-6455/ac4f31. SAND2022-1224 J.

[9] T. A. Gomez, T. Nagayama, C. J. Fontes, D. P. Kilcrease, S. B. Hansen, M. C. Zammit, D. V. Fursa, A. S. Kadyrov, and I. Bray. Effect of Electron Capture on Spectral Line Broadening in Hot Dense Plasmas. *Phys. Rev. Lett.*, 124(5):055003, February 2020. doi: 10.1103/PhysRevLett.124.055003. SAND2020-0489 J.

[10] T. A. Gomez, T. Nagayama, P. B. Cho, M. C. Zammit, C. J. Fontes, D. P. Kilcrease, I. Bray, I. Hubeny, B. H. Dunlap, M. H. Montgomery, and D. E. Winget. All-Order Full-Coulomb Quantum Spectral Line-Shape Calculations. *Phys. Rev. Lett.*, 127(23):235001, December 2021. doi: 10.1103/PhysRevLett.127.235001. SAND2021-14371 J.

[11] T. J. Callow, S. B. Hansen, E. Kraisler, and A. Cangi. First-principles derivation and properties of density-functional average-atom models. *Phys. Rev. Research*, 4:023055, Apr 2022. doi: 10.1103/PhysRevResearch.4.023055. URL `https://link.aps.org/doi/10.1103/PhysRevResearch.4.023055`.

[12] A. D. Baczewski, T. Hentschel, A. Kononov, and S. B. Hansen. Predictions of bound-bound transition signatures in x-ray thomson scattering, 2021. URL `https://arxiv.org/abs/2109.09576`.

[13] T. Nagayama, M. Schaeuble, J. Fein, G. Loisel, M. Wu, S. Hansen, P. Knapp, T. Webb, W. Lewis, J. Schwarz, and R. Vesey. A generalized approach to x-ray data modeling for high-energy-density plasma experiments. *Rev. Sci. Instr.*, SNL tracking No. 1494189, 2022 (submitted).

[14] A. Kononov, A. Olmstead, T. W. Hentschel, S. B. Hansen, and A. D. Baczewski. Trajectory sampling and pseudization in first-principles calculations of electronic stopping in warm dense matter. *in preparation*.

[15] T. W. Hentschel, A. Kononov, A. Olmstead, A. D. Baczewski, A. Cangi, and S. B. Hansen. Effects of strong collisions on dynamic structure factors and stopping powers in warm dense matter. *in preparation*.

[16] A. Kononov and A. D. Baczewski. Indicators of atomic order in the dynamic structure factor of warm dense matter. *in preparation*.

[17] K. Adler, T. Gomez, C. Starrett, N. Shaffer, and S. B. Hansen. A self-consistent approach to ion-stark broadening using an average-atom model. *planned*.

[18] B. F. Kraus, L. Gao, K. W. Hill, M. Bitter, P. C. Efthimion, T. A. Gomez, A. Moreau, R. Hollinger, S. Wang, H. Song, J. J. Rocca, and R. C. Mancini. Solid-Density Ion Temperature from Redshifted and Double-Peaked Stark Line Shapes. *Phys. Rev. Lett.*, 127

(20):205001, November 2021. doi: 10.1103/PhysRevLett.127.205001. SAND2021-13780 J.

[19] J. Strehlow, J. Kim, M. Bailly-Grandvaux, S. Bolatos, H. Smith, A. Haid, E. L. Alfonso, C. Aniculaesei, H. Chen, T. Ditmire, M. E. Donovan, S. B. Hansen, B. M. Hegelich, H. S. McLean, H. J. Quevedo, M. M. Spinks, and F. N. Beg. A laser parameter study on enhancing proton generation from microtube foil targets. *Scientific Reports*, 12, 2022. doi: 10.1038/s41598-022-14881-9. URL https://doi.org/10.1038/s41598-022-14881-9.

[20] S. X. Hu, D. T. Bishel, D. A. Chin, P. M. Nilson, v. v. Karasiev, I. E. Golovkin, M. Gu, S. Hansen, D. I. Mihaylov, N. R. Shaffer, S. Zhang, and T. Walton. Probing extreme atomic physics at ultra-high pressure. *Nature Communications*, under review.

[21] N. F. Beier, H. Allison, P. Efthimion, K. A. Flippo, L. Gao, S. B. Hansen, K. Hill, B. R. Hollinger, M. Logantha, Y. Musthafa, R. Nedbailo, V. Senthilkumaran, R. Shepherd, V. N. Shlyaptsev, H. Song, S. Wang, F. Dollar, J. J. Rocca, and A. E. Hussein. Homogeneous, micron-scale high energy density matter generated by relativistic laser-solid interactions. *Physical Review Letters*, 2002.

[22] S. Jiang, O. L. Landen, H. D. Whitley, S. Hamel, R. London, D. S. Clark, P. Sterne, S. B. Hansen, S. X. Hu, G. W. Collins, and Y. Ping. Thermal transport study of warm dense ch and be by refraction-enhanced x-ray radiography with a deep neural network analysis. *Nature Communications (under review)*.

[23] A. Kononov, C.-W. Lee, T. P. dos Santos, B. Robinson, Y. Yao, Y. Yao, X. Andrade, A. D. Baczewski, E. Constantinescu, A. A. Correa, Y. Kanai, N. Modine, and A. Schleife. Electron dynamics in extended systems within real-time time-dependent density-functional theory. *MRS Communications*, 2022. doi: 10.1557/s43579-022-00273-7.

[24] K. Ramakrishna, A. Cangi, T. Dornheim, A. Baczewski, and J. Vorberger. First-principles modeling of plasmons in aluminum under ambient and extreme conditions. *Physical Review B*, 103(12):125118, 2021.

[25] K. Ramakrishna, M. Lokamani, A. Baczewski, J. Vorberger, and A. Cangi. Electrical conductivity of iron in earth's core from microscopic ohm's law. *arXiv preprint arXiv:2203.06025*, 2022.

[26] K. R. Cochrane, R. W. Lemke, Z. Riford, and J. H. Carpenter. Magnetically launched flyer plate technique for probing electrical conductivity of compressed copper. *Journal of Applied Physics*, 119(10):105902, 2016. doi: 10.1063/1.4943417. URL https://doi.org/10.1063/1.4943417.

[27] A. Porwitzky, K. R. Cochrane, and B. Stoltzfus. Determining the electrical conductivity of metals using the 2 ma thor pulsed power driver. *Review of Scientific Instruments*, 92(5): 053551, 2021. doi: 10.1063/5.0037870. URL https://doi.org/10.1063/5.0037870.

[28] J. C. Slater. The self consistent field and the structure of atoms. *Physical Review*, 32(3): 339, 1928.

[29] P. Hohenberg and W. Kohn. Inhomogeneous electron gas. *Physical review*, 136(3B):B864, 1964.

[30] W. Kohn and L. J. Sham. Self-consistent equations including exchange and correlation effects. *Phys. Rev.*, 140:A1133–A1138, Nov 1965. doi: 10.1103/PhysRev.140.A1133. URL https://link.aps.org/doi/10.1103/PhysRev.140.A1133.

[31] L. H. Thomas. The calculation of atomic fields. *Mathematical Proceedings of the Cambridge Philosophical Society*, 23(5):542–548, 1927. doi: 10.1017/S0305004100011683.

[32] E. Fermi. Eine statistische methode zur bestimmung einiger eigenschaften des atoms und ihre anwendung auf die theorie des periodischen systems der elemente. *Zeitschrift fur Physik*, 48:73–79, 1928. doi: https://doi.org/10.1007/BF01351576.

[33] D. A. Liberman. Self-consistent field model for condensed matter. *Phys. Rev. B*, 20: 4981–4989, Dec 1979. doi: 10.1103/PhysRevB.20.4981. URL https://link.aps.org/doi/10.1103/PhysRevB.20.4981.

[34] B. Wilson, V. Sonnad, P. Sterne, and W. Isaacs. Purgatorio: a new implementation of the inferno algorithm. *Journal of Quantitative Spectroscopy and Radiative Transfer*, 99(1): 658–679, 2006. ISSN 0022-4073. doi: https://doi.org/10.1016/j.jqsrt.2005.05.053. URL https://www.sciencedirect.com/science/article/pii/S0022407305001846. Radiative Properties of Hot Dense Matter.

[35] M. W. C. Dharma-wardana and F. m. c. Perrot. Density-functional theory of hydrogen plasmas. *Phys. Rev. A*, 26:2096–2104, Oct 1982. doi: 10.1103/PhysRevA.26.2096. URL https://link.aps.org/doi/10.1103/PhysRevA.26.2096.

[36] C. Starrett and D. Saumon. Fully variational average atom model with ion-ion correlations. *Physical Review E*, 85(2):026403, 2012. doi: 10.1103/PhysRevE.85.026403.

[37] C. Starrett and D. Saumon. A simple method for determining the ionic structure of warm dense matter. *High Energy Density Physics*, 10:35, 2014. doi: 10.1016/j.hedp.2013.12.001.

[38] W. Johnson, J. Nilsen, K. Cheng, et al. Thomson scattering in the average-atom approximation. *Physical Review E*, 86(3):036410, 2012. doi: 10.1103/PhysRevE.86.036410.

[39] G. Kresse and J. Furthmüller. Efficient iterative schemes for ab initio total-energy calculations using a plane-wave basis set. *Physical review B*, 54(16):11169, 1996.

[40] G. Kresse and J. Furthmüller. Efficiency of ab-initio total energy calculations for metals and semiconductors using a plane-wave basis set. *Computational materials science*, 6(1): 15–50, 1996.

[41] G. Kresse and D. Joubert. From ultrasoft pseudopotentials to the projector augmented-wave method. *Physical review b*, 59(3):1758, 1999.

[42] L. Hedin and B. I. Lundqvist. Explicit local exchange-correlation potentials. *Journal of Physics C: Solid State Physics*, 4(14):2064–2083, oct 1971. doi: 10.1088/0022-3719/4/14/022. URL https://doi.org/10.1088/0022-3719/4/14/022.

[43] M. S. Murillo, J. Weisheit, S. B. Hansen, and M. Dharma-Wardana. Partial ionization in dense plasmas: Comparisons among average-atom density functional models. *Physical Review E*, 87(6):063113, 2013. doi: 10.1103/PhysRevE.87.063113.

[44] Pressure in the average-atom model. *unpublished*, 2002. URL https://www3.nd.edu/~johnson/.

[45] R. Piron and T. Blenski. Variational-average-atom-in-quantum-plasmas (vaaqp) code and virial theorem: Equation-of-state and shock-hugoniot calculations for warm dense al, fe, cu, and pb. *Phys. Rev. E*, 83:026403, Feb 2011. doi: 10.1103/PhysRevE.83.026403. URL https://link.aps.org/doi/10.1103/PhysRevE.83.026403.

[46] J. Gaffney, S. Hu, P. Arnault, A. Becker, L. Benedict, T. Boehly, P. Celliers, D. Ceperley, O. ÄŒertÃk, J. ClÃ©rouin, G. Collins, L. Collins, J.-F. Danel, N. Desbiens, M. Dharma-wardana, Y. Ding, A. Fernandez-PaÃ±ella, M. Gregor, P. Grabowski, S. Hamel, S. Hansen, L. Harbour, X. He, D. Johnson, W. Kang, V. Karasiev, L. Kazandjian, M. Knudson, T. Ogitsu, C. Pierleoni, R. Piron, R. Redmer, G. Robert, D. Saumon, A. Shamp, T. Sjostrom, A. Smirnov, C. Starrett, P. Sterne, A. Wardlow, H. Whitley, B. Wilson, P. Zhang, and E. Zurek. A review of equation-of-state models for inertial confinement fusion materials. *High Energy Density Physics*, 28:7–24, 2018. ISSN 1574-1818. doi: https://doi.org/10.1016/j.hedp.2018.08.001. URL https://www.sciencedirect.com/science/article/pii/S1574181818300508.

[47] D. Saumon. The ion-ion bridge function in the variational modified hypernetted-chain formalism. 2014.

[48] F. Lucco Castello and P. Tolias. On the advanced integral equation theory description of dense yukawa one-component plasma liquids. *Contributions to Plasma Physics*, 61, 01 2021. doi: 10.1002/ctpp.202000105.

[49] M. Schörner, B. B. L. Witte, A. D. Baczewski, A. Cangi, and R. Redmer. Ab initio study of shock-compressed copper. *Phys. Rev. B*, 106:054304, Aug 2022. doi: 10.1103/PhysRevB.106.054304. URL https://link.aps.org/doi/10.1103/PhysRevB.106.054304.

[50] M. Desjarlais. Practical improvements to the lee-more conductivity near the metal-insulator transition. *Contributions to Plasma Physics*, 41(2-3):267–270, 2001. doi: https://doi.org/10.1002/1521-3986(200103)41:2/3<267::AID-CTPP267>3.0.CO;2-P.

[51] Y. T. Lee and R. M. More. An electron conductivity model for dense plasmas. *The Physics of Fluids*, 27(5):1273–1286, 1984. doi: 10.1063/1.864744. URL https://aip.scitation.org/doi/abs/10.1063/1.864744.

[52] J. M. Ziman. A theory of the electrical properties of liquid metals. i: The monovalent metals. *The Philosophical Magazine: A Journal of Theoretical Experimental and Applied Physics*, 6(68):1013–1034, 1961. doi: 10.1080/14786436108243361. URL https://doi.org/10.1080/14786436108243361.

[53] P. Sterne, S. Hansen, B. Wilson, and W. Isaacs. Equation of state, occupation probabilities and conductivities in the average atom purgatorio code. *High Energy Density Physics*, 3: 278–282, 02 2007. doi: 10.1016/j.hedp.2007.02.037.

[54] D. Burrill, D. Feinblum, M. Charest, and C. Starrett. Comparison of electron transport calculations in warm dense matter using the ziman formula. *High Energy Density Physics*, 19:1–10, 2016. ISSN 1574-1818. doi: https://doi.org/10.1016/j.hedp.2016.01.004. URL https://www.sciencedirect.com/science/article/pii/S1574181816300015.

[55] N. Wetta and J.-C. Pain. Consistent approach for electrical resistivity within ziman's theory from solid state to hot dense plasma: Application to aluminum. *Phys. Rev. E*, 102:053209, Nov 2020. doi: 10.1103/PhysRevE.102.053209. URL https://link.aps.org/doi/10.1103/PhysRevE.102.053209.

[56] G. A. Rinker. Systematic calculations of plasma transport coefficients for the periodic table. *Phys. Rev. A*, 37:1284–1297, Feb 1988. doi: 10.1103/PhysRevA.37.1284. URL https://link.aps.org/doi/10.1103/PhysRevA.37.1284.

[57] D. A. Baiko, A. D. Kaminker, A. Y. Potekhin, and D. G. Yakovlev. Ion structure factors and electron transport in dense coulomb plasmas. *Phys. Rev. Lett.*, 81:5556–5559, Dec 1998. doi: 10.1103/PhysRevLett.81.5556. URL https://link.aps.org/doi/10.1103/PhysRevLett.81.5556.

[58] D. A. Young, E. M. Corey, and H. E. DeWitt. Analytic fit to the one-component-plasma structure factor. *Phys. Rev. A*, 44:6508–6512, Nov 1991. doi: 10.1103/PhysRevA.44.6508. URL https://link.aps.org/doi/10.1103/PhysRevA.44.6508.

[59] P. Grabowski, S. Hansen, M. Murillo, L. Stanton, F. Graziani, A. Zylstra, S. Baalrud, P. Arnault, A. Baczewski, L. Benedict, C. Blancard, O. ÄŒertÃk, J. ClÃ©rouin, L. Collins, S. Copeland, A. Correa, J. Dai, J. Daligault, M. Desjarlais, M. Dharma-wardana, G. Faussurier, J. Haack, T. Haxhimali, A. Hayes-Sterbenz, Y. Hou, S. Hu, D. Jensen, G. Jungman, G. Kagan, D. Kang, J. Kress, Q. Ma, M. Marciante, E. Meyer, R. Rudd, D. Saumon, L. Shulenburger, R. Singleton, T. Sjostrom, L. Stanek, C. Starrett, C. Ticknor, S. Valaitis, J. Venzke, and A. White. Review of the first charged-particle transport coefficient comparison workshop. *High Energy Density Physics*, 37:100905, 2020. ISSN 1574-1818. doi: https://doi.org/10.1016/j.hedp.2020.100905. URL https://www.sciencedirect.com/science/article/pii/S1574181820301282.

[60] M. Marques, A. Rubio, E. K. Gross, K. Burke, F. Nogueira, and C. A. Ullrich. *Time-dependent density functional theory*, volume 706. Springer Science & Business Media, 2006.

[61] C. A. Ullrich. Time-dependent density-functional theory: concepts and applications. 2011.

[62] M. Desjarlais, J. Kress, and L. Collins. Electrical conductivity for warm, dense aluminum plasmas and liquids. *Physical Review E*, 66(2):025401, 2002.

[63] G. F. Bertsch, J.-I. Iwata, A. Rubio, and K. Yabana. Real-space, real-time method for the dielectric function. *Physical Review B*, 62(12):7998, 2000.

[64] X. Andrade, S. Hamel, and A. A. Correa. Negative differential conductivity in liquid aluminum from real-time quantum simulations. *The European Physical Journal B*, 91(10): 1–7, 2018.

[65] M. P. Desjarlais, C. R. Scullard, L. X. Benedict, H. D. Whitley, and R. Redmer. Density-functional calculations of transport properties in the nondegenerate limit and the role of electron-electron scattering. *Physical Review E*, 95(3):033203, 2017.

[66] H. Reinholz, G. Röpke, S. Rosmej, and R. Redmer. Conductivity of warm dense matter including electron-electron collisions. *Phys. Rev. E*, 91:043105, Apr 2015. doi: 10.1103/PhysRevE.91.043105. URL https://link.aps.org/doi/10.1103/PhysRevE.91.043105.

[67] N. R. Shaffer and C. E. Starrett. Model of electron transport in dense plasmas spanning temperature regimes. *Phys. Rev. E*, 101:053204, May 2020. doi: 10.1103/PhysRevE.101.053204. URL https://link.aps.org/doi/10.1103/PhysRevE.101.053204.

[68] A. Y. Potekhin, D. A. Baiko, P. Haensel, and D. G. Yakovlev. Transport properties of degenerate electrons in neutron star envelopes and white dwarf cores. *Astronomy and Astrophysics*, 346:345–353, June 1999.

[69] S. D. Baalrud and J. Daligault. Effective potential theory for transport coefficients across coupling regimes. *Phys. Rev. Lett.*, 110:235001, Jun 2013. doi: 10.1103/PhysRevLett.110.235001. URL https://link.aps.org/doi/10.1103/PhysRevLett.110.235001.

[70] W. Johnson, C. Guet, and G. Bertsch. Optical properties of plasmas based on an average-atom model. *Journal of Quantitative Spectroscopy and Radiative Transfer*, 99(1): 327–340, 2006. ISSN 0022-4073. doi: https://doi.org/10.1016/j.jqsrt.2005.05.026. URL https://www.sciencedirect.com/science/article/pii/S0022407305001573. Radiative Properties of Hot Dense Matter.

[71] S. Mazevet, M. P. Desjarlais, L. A. Collins, J. D. Kress, and N. H. Magee. Simulations of the optical properties of warm dense aluminum. *Phys. Rev. E*, 71:016409, Jan 2005. doi: 10.1103/PhysRevE.71.016409. URL https://link.aps.org/doi/10.1103/PhysRevE.71.016409.

[72] H. Reinholz, R. Redmer, G. Röpke, and A. Wierling. Long-wavelength limit of the dynamical local-field factor and dynamical conductivity of a two-component plasma. *Phys. Rev. E*, 62:5648–5666, Oct 2000. doi: 10.1103/PhysRevE.62.5648. URL https://link.aps.org/doi/10.1103/PhysRevE.62.5648.

[73] G. Faussurier and C. Blancard. Electron-ion collision-frequency for x-ray thomson scattering in dense plasmas. *Physics of Plasmas*, 23(1):012703, 2016. doi: 10.1063/1.4939606.

[74] C. Starrett. Kubo-greenwood approach to conductivity in dense plasmas with average atom models. *High Energy Density Physics*, 19:58–64, 2016. ISSN 1574-1818. doi: https://doi.org/10.1016/j.hedp.2016.04.001. URL https://www.sciencedirect.com/science/article/pii/S1574181816300398.

[75] S. H. Glenzer, G. Gregori, F. J. Rogers, D. H. Froula, S. W. Pollaine, R. S. Wallace, and O. L. Landen. X-ray scattering from solid density plasmas. *Physics of Plasmas*, 10(6): 2433–2441, 2003. doi: 10.1063/1.1570420. URL https://doi.org/10.1063/1.1570420.

[76] B. B. L. Witte, L. B. Fletcher, E. Galtier, E. Gamboa, H. J. Lee, U. Zastrau, R. Redmer, S. H. Glenzer, and P. Sperling. Warm dense matter demonstrating non-drude conductivity from observations of nonlinear plasmon damping. *Phys. Rev. Lett.*, 118:225001, May 2017. doi: 10.1103/PhysRevLett.118.225001. URL https://link.aps.org/doi/10.1103/PhysRevLett.118.225001.

[77] P. Sperling, E. J. Gamboa, H. J. Lee, H. K. Chung, E. Galtier, Y. Omarbakiyeva, H. Reinholz, G. Röpke, U. Zastrau, J. Hastings, L. B. Fletcher, and S. H. Glenzer. Free-electron x-ray laser measurements of collisional-damped plasmons in isochorically heated warm dense matter. *Phys. Rev. Lett.*, 115:115001, Sep 2015. doi: 10.1103/PhysRevLett.115.115001. URL https://link.aps.org/doi/10.1103/PhysRevLett.115.115001.

[78] T. Döppner, O. Landen, H. Lee, P. Neumayer, S. Regan, and S. Glenzer. Temperature measurement through detailed balance in x-ray thomson scattering. *High Energy Density Physics*, 5(3):182–186, 2009. ISSN 1574-1818. doi: https://doi.org/10.1016/j.hedp.2009.05.012. URL https://www.sciencedirect.com/science/article/pii/S1574181809000548.

[79] O. S. Humphries, R. S. Marjoribanks, Q. Y. van den Berg, E. C. Galtier, M. F. Kasim, H. J. Lee, A. J. F. Miscampbell, B. Nagler, R. Royle, J. S. Wark, and S. M. Vinko. Probing the electronic structure of warm dense nickel via resonant inelastic x-ray scattering. *Phys. Rev. Lett.*, 125:195001, Nov 2020. doi: 10.1103/PhysRevLett.125.195001. URL https://link.aps.org/doi/10.1103/PhysRevLett.125.195001.

[80] J. Chihara. Interaction of photons with plasmas and liquid metals - photoabsorption and scattering. *Journal of Physics: Condensed Matter*, 12(3):231–247, dec 1999. doi: 10.1088/0953-8984/12/3/303. URL https://doi.org/10.1088/0953-8984/12/3/303.

[81] A. D. Baczewski, L. Shulenburger, M. Desjarlais, S. Hansen, and R. Magyar. X-ray thomson scattering in warm dense matter without the chihara decomposition. *Physical review letters*, 116(11):115004, 2016.

[82] A. N. Souza, D. J. Perkins, C. E. Starrett, D. Saumon, and S. B. Hansen. Predictions of x-ray scattering spectra for warm dense matter. *Phys. Rev. E*, 89:023108, Feb 2014. doi: 10.1103/PhysRevE.89.023108. URL https://link.aps.org/doi/10.1103/PhysRevE.89.023108.

[83] S. H. Glenzer and R. Redmer. X-ray thomson scattering in high energy density plasmas. *Rev. Mod. Phys.*, 81:1625–1663, Dec 2009. doi: 10.1103/RevModPhys.81.1625. URL https://link.aps.org/doi/10.1103/RevModPhys.81.1625.

[84] N. D. Mermin. Lindhard dielectric function in the relaxation-time approximation. *Phys. Rev. B*, 1:2362–2363, Mar 1970. doi: 10.1103/PhysRevB.1.2362. URL https://link.aps.org/doi/10.1103/PhysRevB.1.2362.

[85] A. D. Baczewski, L. Shulenburger, M. P. Desjarlais, and R. J. Magyar. Numerical implementation of time-dependent density functional theory for extended systems in extreme environments. Technical report, Sandia National Lab.(SNL-NM), Albuquerque, NM (United States), 2014.

[86] P. Wang, T. M. Mehlhorn, and J. J. MacFarlane. A unified self-consistent model for calculating ion stopping power in icf plasma. *Physics of Plasmas*, 5(8):2977–2987, 1998. doi: 10.1063/1.873022. URL https://doi.org/10.1063/1.873022.

[87] G. Faussurier, C. Blancard, P. Cossé, and P. Renaudin. Equation of state, transport coefficients, and stopping power of dense plasmas from the average-atom model self-consistent approach for astrophysical and laboratory plasmas. *Physics of Plasmas*, 17 (5):052707, 2010. doi: 10.1063/1.3420276. URL https://doi.org/10.1063/1.3420276.

[88] R. J. Magyar, L. Shulenburger, and A. Baczewski. Stopping of deuterium in warm dense deuterium from ehrenfest time-dependent density functional theory, 2016.

[89] A. Schleife, Y. Kanai, and A. A. Correa. Accurate atomistic first-principles calculations of electronic stopping. *Phys. Rev. B*, 91(1):014306, 2015. doi: 10.1103/PhysRevB.91.014306.

[90] I. Maliyov, J.-P. Crocombette, and F. Bruneval. Electronic stopping power from time-dependent density-functional theory in gaussian basis. *Eur. Phys. J. B*, 91(8):172, 2018. doi: 10.1140/epjb/e2018-90289-y.

[91] C. R. Scullard, S. Serna, L. X. Benedict, C. L. Ellison, and F. R. Graziani. Analytic expressions for electron-ion temperature equilibration rates from the lenard-balescu equation. *Phys. Rev. E*, 97:013205, Jan 2018. doi: 10.1103/PhysRevE.97.013205. URL https://link.aps.org/doi/10.1103/PhysRevE.97.013205.

[92] M. W. C. Dharma-wardana and F. m. c. Perrot. Energy relaxation and the quasiequation of state of a dense two-temperature nonequilibrium plasma. *Phys. Rev. E*, 58:3705–3718, Sep 1998. doi: 10.1103/PhysRevE.58.3705. URL https://link.aps.org/doi/10.1103/PhysRevE.58.3705.

[93] G. Faussurier. Electron-ion coupling factor for temperature relaxation in dense plasmas. *Phys. Rev. E*, 101:023206, Feb 2020. doi: 10.1103/PhysRevE.101.023206. URL https://link.aps.org/doi/10.1103/PhysRevE.101.023206.

[94] M. F. Gu. The flexible atomic code. *AIP Conference Proceedings*, 730(1):127–136, 2004. doi: 10.1063/1.1824864. URL https://aip.scitation.org/doi/abs/10.1063/1.1824864.

[95] Y. Ralchenko. *Modern Methods in Collisional-Radiative Modeling of Plasmas*. Springer, 2016.

[96] R. D. Cowan. *The Theory of Atomic Structure and Spectra*. Los Alamos Series in Basic and Applied Sciences. University of California Press, Ltd., Berkeley, 1981.

[97] G. Faussurier and C. Blancard. Density effects on electronic configurations in dense plasmas. *Phys. Rev. E*, 97:023206, Feb 2018. doi: 10.1103/PhysRevE.97.023206. URL https://link.aps.org/doi/10.1103/PhysRevE.97.023206.

[98] A. N. Cox, J. N. Stewart, and D. D. Lilers. Effects of Bound-Bound Absorption on Stellar Opacities. *The Astrophysical Journal Supplement*, 11:1, January 1965. doi: 10.1086/190107.

[99] G. Luo. The equation of state in the chemical picture: A grand canonical approach. *Astronomy and Astrophysics*, 281(2):460–464, January 1994.

[100] S. Hansen, E. Harding, P. Knapp, M. Gomez, T. Nagayama, and J. Bailey. Changes in the electronic structure of highly compressed iron revealed by x-ray fluorescence lines and absorption edges. *High Energy Density Physics*, 24:39–43, 2017. ISSN 1574-1818. doi: https://doi.org/10.1016/j.hedp.2017.07.002. URL https://www.sciencedirect.com/science/article/pii/S1574181817300642.

[101] G. Massacrier and J. Dubau. A theoretical approach to n-electron ionic structure under dense plasma conditions: I. blue and red shift. *Journal of Physics B: Atomic, Molecular and Optical Physics*, 23(13):2459S–2469S, jul 1990. doi: 10.1088/0953-4075/23/13/033. URL https://doi.org/10.1088/0953-4075/23/13/033.

[102] H. Nguyen, M. Koenig, D. Benredjem, M. Caby, and G. Coulaud. Atomic structure and polarization line shift in dense and hot plasmas. *Phys. Rev. A*, 33:1279–1290, Feb 1986. doi: 10.1103/PhysRevA.33.1279. URL https://link.aps.org/doi/10.1103/PhysRevA.33.1279.

[103] S. Jiang, A. E. Lazicki, S. B. Hansen, P. A. Sterne, P. Grabowski, R. Shepherd, H. A. Scott, R. F. Smith, J. H. Eggert, and Y. Ping. Measurements of pressure-induced $k\beta$ line shifts in ramp compressed cobalt up to 8 mbar. *Phys. Rev. E*, 101:023204, Feb 2020. doi: 10.1103/PhysRevE.101.023204. URL https://link.aps.org/doi/10.1103/PhysRevE.101.023204.

[104] P. Beiersdorfer, G. V. Brown, A. McKelvey, R. Shepherd, D. J. Hoarty, C. R. D. Brown, M. P. Hill, L. M. R. Hobbs, S. F. James, J. Morton, and L. Wilson. High-resolution measurements of cl^{15+} line shifts in hot, solid-density plasmas. *Phys. Rev. A*, 100:012511,

Jul 2019. doi: 10.1103/PhysRevA.100.012511. URL https://link.aps.org/doi/10.1103/PhysRevA.100.012511.

[105] E. Hill, G. PÃ©rez-Callejo, and S. Rose. Alice: A non-lte plasma atomic physics, kinetics and lineshape package. *High Energy Density Physics*, 26:56–67, 2018. ISSN 1574-1818. doi: https://doi.org/10.1016/j.hedp.2018.01.002. URL https://www.sciencedirect.com/science/article/pii/S1574181818300065.

[106] C. A. Iglesias. Partially resolved transition array model in intermediate coupling. *High Energy Density Physics*, 8(3):260–265, 2012. ISSN 1574-1818. doi: https://doi.org/10.1016/j.hedp.2012.03.015. URL https://www.sciencedirect.com/science/article/pii/S1574181812000729.

[107] W. A. Lokke and W. H. Grasberger. Xsnq-u: a non-lte emission and absorption coefficient subroutine. 1 1977. doi: 10.2172/7299968. URL https://www.osti.gov/biblio/7299968.

[108] G. Faussurier, C. Blancard, and P. CossÃ©. Coupling of an average-atom model with a collisional-radiative equilibrium model. *Physics of Plasmas*, 21(11):112707, 2014. doi: 10.1063/1.4902123. URL https://doi.org/10.1063/1.4902123.

[109] T. A. Gomez, T. Nagayama, D. P. Kilcrease, M. H. Montgomery, and D. E. Winget. Density-matrix correlations in the relaxation theory of electron broadening. *Physical Review A*, 98(1):012505, July 2018. doi: 10.1103/PhysRevA.98.012505.

[110] E. Stambulchik, D. V. Fisher, Y. Maron, H. R. Griem, and S. Alexiou. Correlation effects and their influence on line broadening in plasmas: Application to H $_\alpha$. *High Energy Density Physics*, 3(1-2):272–277, May 2007. doi: 10.1016/j.hedp.2007.02.021.

[111] S. Alexiou and R. W. Lee. Semiclassical calculations of line broadening in plasmas: Comparison with quantal results. *Journal of Quantitative Spectroscopy and Radiative Transfer*, 99(1-3):10–20, May 2006. doi: 10.1016/j.jqsrt.2005.05.001.

[112] H. R. Griem. *Spectral line broadening by plasmas*. 1974.

[113] S. Alexiou and Y. Ralchenko. Z scaling of the 3P-3S Li isoelectronic series transition: Quadrupole Stark broadening and resonances. *Physical Review A*, 49(4):3086–3088, April 1994. doi: 10.1103/PhysRevA.49.3086.

[114] I. Bray and A. T. Stelbovics. Convergent close-coupling calculations of electron-hydrogen scattering. *Physical Review A*, 46(11):6995–7011, December 1992. doi: 10.1103/PhysRevA.46.6995.

[115] J. E. Bailey, T. Nagayama, G. P. Loisel, G. A. Rochau, C. Blancard, J. Colgan, P. Cosse, G. Faussurier, C. Fontes, F. Gilleron, et al. A higher-than-predicted measurement of iron opacity at solar interior temperatures. *Nature*, 517(7532):56–59, 2015. doi: 10.1038/nature14048.

[116] T. A. Gomez, J. White, C. J. Fontes, and Kilcrease. Examination of Sum Rule Constraints on Opacities and Redistribution of Opacity in Dense Plasmas. In Prep (2022), Sandia Tracking Number: 1617893, 2022.

[117] C. A. Iglesias, F. J. Rogers, R. Shepherd, A. Bar-Shalom, M. S. Murillo, D. P. Kilcrease, A. Calisti, and R. W. Lee. Fast electric microfield distribution calculations in extreme matter conditions. *Journal of Quantitative Spectroscopy and Radiative Transfer*, 65(1-3): 303–315, April 2000. doi: 10.1016/S0022-4073(99)00076-X.

[118] S. Hansen, H.-K. Chung, C. Fontes, Y. Ralchenko, H. Scott, and E. Stambulchik. Review of the 10th non-lte code comparison workshop. *High Energy Density Physics*, 35:100693, 2020. ISSN 1574-1818. doi: https://doi.org/10.1016/j.hedp.2019.06.001. URL https://www.sciencedirect.com/science/article/pii/S1574181819300357.

[119] J. W. Thornhill, J. P. Apruzese, J. Davis, R. W. Clark, A. L. Velikovich, J. L. Giuliani, Y. K. Chong, K. G. Whitney, C. Deeney, C. A. Coverdale, and F. L. Cochran. An efficient tabulated collisional radiative equilibrium radiation transport model suitable for multidimensional hydrodynamics calculations. *Physics of Plasmas*, 8(7):3480–3489, 2001. doi: 10.1063/1.1373415. URL https://doi.org/10.1063/1.1373415.

[120] S. Hansen, B. Jones, J. Giuliani, J. Apruzese, J. Thornhill, H. Scott, D. Ampleford, C. Jennings, C. Coverdale, M. Cuneo, G. Rochau, J. Bailey, A. Dasgupta, R. Clark, and J. Davis. Doppler effects on 3-d non-lte radiation transport and emission spectra. *High Energy Density Physics*, 7(4):303–311, 2011. ISSN 1574-1818. doi: https://doi.org/10.1016/j.hedp.2011.06.002. URL https://www.sciencedirect.com/science/article/pii/S1574181811000735.

[121] H. A. Scott, J. A. Harte, M. E. Foord, and D. T. Woods. Using tabulated nlte data for hohlraum simulations. *Physics of Plasmas*, 29(8):082703, 2022. doi: 10.1063/5.0102624.

[122] Y. Frank and H. A. Scott. The bands method for tabulating nlte material properties. *High Energy Density Physics*, 43:100998, 2022. ISSN 1574-1818. doi: https://doi.org/10.1016/j.hedp.2022.100998. URL https://www.sciencedirect.com/science/article/pii/S1574181822000222.

[123] S. P. Regan, R. Epstein, B. A. Hammel, L. J. Suter, J. Ralph, H. Scott, M. A. Barrios, D. K. Bradley, D. A. Callahan, C. Cerjan, G. W. Collins, S. N. Dixit, T. Doeppner, M. J. Edwards, D. R. Farley, S. Glenn, S. H. Glenzer, I. E. Golovkin, S. W. Haan, A. Hamza, D. G. Hicks, N. Izumi, J. D. Kilkenny, J. L. Kline, G. A. Kyrala, O. L. Landen, T. Ma, J. J. MacFarlane, R. C. Mancini, R. L. McCrory, N. B. Meezan, D. D. Meyerhofer, A. Nikroo, K. J. Peterson, T. C. Sangster, P. Springer, and R. P. J. Town. Hot-spot mix in ignition-scale implosions on the nif. *Physics of Plasmas*, 19(5):056307, 2012. doi: 10.1063/1.3694057. URL https://doi.org/10.1063/1.3694057.

[124] D. Ampleford, S. B. Hansen, C. A. Jennings, T. J. Webb, V. Harper-Slaboszewicz, G. P. Loisel, T. M. Flanagan, K. S. Bell, B. M. Jones, G. A. Rochau, J. P. Chittenden, M. Sherlock, B. Appelbe, J. Giuliani, N. Ouart, J. Seely, and L. A. McPherson. Non-thermal x-ray emission from wire array z-pinches. *SAND2015-10453*.

[125] G. A. Rochau, J. E. Bailey, R. E. Falcon, G. P. Loisel, T. Nagayama, R. C. Mancini, I. Hall, D. E. Winget, M. H. Montgomery, and D. A. Liedahl. Zapp: The z astrophysical plasma properties collaboration. *Physics of Plasmas*, 21(5):056308, 2014. doi: 10.1063/1.4875330. URL https://doi.org/10.1063/1.4875330.

[126] G. P. Loisel, J. E. Bailey, D. A. Liedahl, C. J. Fontes, T. R. Kallman, T. Nagayama, S. B. Hansen, G. A. Rochau, R. C. Mancini, and R. W. Lee. Benchmark experiment for photoionized plasma emission from accretion-powered x-ray sources. *Phys. Rev. Lett.*, 119:075001, Aug 2017. doi: 10.1103/PhysRevLett.119.075001. URL https://link.aps.org/doi/10.1103/PhysRevLett.119.075001.

[127] S. B. Hansen and A. S. Shlyaptseva. Effects of the electron energy distribution function on modeled x-ray spectra. *Phys. Rev. E*, 70:036402, Sep 2004. doi: 10.1103/PhysRevE.70.036402. URL https://link.aps.org/doi/10.1103/PhysRevE.70.036402.

[128] A. Ciardi, S. V. Lebedev, A. Frank, E. G. Blackman, J. P. Chittenden, C. J. Jennings, D. J. Ampleford, S. N. Bland, S. C. Bott, J. Rapley, G. N. Hall, F. A. Suzuki-Vidal, A. Marocchino, T. Lery, and C. Stehle. The evolution of magnetic tower jets in the laboratory. *Physics of Plasmas*, 14(5):056501, may 2007. doi: 10.1063/1.2436479. URL https://doi.org/10.1063%2F1.2436479.

[129] J. M. Stone, D. Mihalas, and M. L. Norman. ZEUS-2D: A Radiation Magnetohydrodynamics Code for Astrophysical Flows in Two Space Dimensions. III. The Radiation Hydrodynamic Algorithms and Tests. *The Astrophysical Journal Supplement*, 80:819, June 1992. doi: 10.1086/191682.

[130] G. Olson, L. Auer, and M. Hall. Diffusion, p1, and other approximate forms of radiation transport. *Journal of Quantitative Spectroscopy and Radiative Transfer*, 64:619–634, 03 2000. doi: 10.1016/S0022-4073(99)00150-8.

[131] S. I. Braginskii. Transport Processes in a Plasma. *Reviews of Plasma Physics*, 1:205, January 1965.

[132] E. M. Epperlein and M. G. Haines. Plasma transport coefficients in a magnetic field by direct numerical solution of the fokkerâ€“planck equation. *The Physics of Fluids*, 29(4): 1029–1041, 1986. doi: 10.1063/1.865901. URL https://aip.scitation.org/doi/abs/10.1063/1.865901.

[133] J. J. Macfarlane, I. E. Golovkin, and P. R. Woodruff. HELIOS-CR A 1-D radiation-magnetohydrodynamics code with inline atomic kinetics modeling. *Journal of Quantitative Spectroscopy and Radiative Transfer*, 99(1-3):381–397, May 2006. doi: 10.1016/j.jqsrt.2005.05.031.

[134] Y.-F. Jiang, J. M. Stone, and S. W. Davis. An Algorithm for Radiation Magnetohydrodynamics Based on Solving the Time-dependent Transfer Equation. *The Astrophysical Journal Supplement*, 213(1):7, July 2014. doi: 10.1088/0067-0049/213/1/7.

[135] S. B. Hansen, M. R. Gomez, A. B. Sefkow, S. A. Slutz, D. B. Sinars, K. D. Hahn, E. C. Harding, P. F. Knapp, P. F. Schmit, T. J. Awe, R. D. McBride, C. A. Jennings, M. Geissel, A. J. Harvey-Thompson, K. J. Peterson, D. C. Rovang, G. A. Chandler, G. W. Cooper, M. E. Cuneo, M. C. Herrmann, M. H. Hess, O. Johns, D. C. Lamppa, M. R. Martin, J. L. Porter, G. K. Robertson, G. A. Rochau, C. L. Ruiz, M. E. Savage, I. C. Smith, W. A. Stygar, R. A. Vesey, B. E. Blue, D. Ryutov, D. G. Schroen, and K. Tomlinson. Diagnosing

magnetized liner inertial fusion experiments on z. *Physics of Plasmas*, 22(5):056313, 2015. doi: 10.1063/1.4921217. URL https://aip.scitation.org/doi/abs/10.1063/1.4921217.

[136] P. F. Knapp, M. E. Glinsky, M. A. Schaeuble, C. A. Jennings, M. Evans, J. Gunning, T. J. Awe, G. A. Chandler, M. Geissel, M. R. Gomez, K. D. Hahn, S. B. Hansen, E. C. Harding, A. J. Harvey-Thompson, S. Humane, B. T. Klein, M. Mangan, T. Nagayama, A. J. Porwitzky, D. E. Ruiz, P. F. Schmit, S. A. Slutz, I. C. Smith, M. R. Weis, D. A. Yager-Elorriaga, D. J. Ampleford, K. Beckwith, T. R. Mattsson, K. J. Peterson, and D. B. Sinars. Estimation of stagnation performance metrics in magnetized liner inertial fusion experiments using bayesian data assimilation. *Physics of Plasmas*, 29(5):052711, 2022. doi: 10.1063/5.0087115.

[137] T. Nagayama, R. C. Mancini, R. Florido, D. Mayes, R. Tommasini, J. A. Koch, J. A. Delettrez, S. P. Regan, and V. A. Smalyuk. Investigation of a polychromatic tomography method for the extraction of the three-dimensional spatial structure of implosion core plasmas. *Physics of Plasmas*, 19(8):082705, 2012. doi: 10.1063/1.4743017.

[138] L. H. Thomas. The calculation of atomic fields. In *Mathematical Proceedings of the Cambridge Philosophical Society*, volume 23, pages 542–548. Cambridge University Press, 1927.

[139] E. Fermi. Un metodo statistico per la determinazione di alcune priorieta dell'atome. *Rend. Accad. Naz. Lincei*, 6(602-607):32, 1927.

[140] D. Hartree. The Wave Mechanics of an Atom with a Non-Coulomb Central Field. Part I. Theory and Methods. In *Mathematical Proceedings of the Cambridge Philosophical Society*, volume 24, pages 89–110. Cambridge University Press, 1928.

[141] P. A. M. Dirac. Quantum mechanics of many-electron systems. *Proceedings of the Royal Society of London. Series A, Containing Papers of a Mathematical and Physical Character*, 123(792):714–733, 1929.

[142] V. Fock. Näherungsmethode zur Lösung des quantenmechanischen Mehrkörperproblems. *Zeitschrift für Physik*, 61(1-2):126–148, 1930.

[143] J. P. Perdew and A. Zunger. Self-interaction correction to density-functional approximations for many-electron systems. *Physical Review B*, 23(10):5048, 1981.

[144] J. P. Perdew, K. Burke, and M. Ernzerhof. Generalized gradient approximation made simple. *Physical review letters*, 77(18):3865, 1996.

[145] J. Vorberger, Z. Donko, I. M. Tkachenko, and D. O. Gericke. Dynamic ion structure factor of warm dense matter. *Phys. Rev. Lett.*, 109:225001, Nov 2012. doi: 10.1103/PhysRevLett.109.225001. URL https://link.aps.org/doi/10.1103/PhysRevLett.109.225001.

[146] B. B. Witte, L. Fletcher, E. Galtier, E. Gamboa, H. Lee, U. Zastrau, R. Redmer, S. Glenzer, and P. Sperling. Warm dense matter demonstrating non-drude conductivity from observations of nonlinear plasmon damping. *Physical review letters*, 118(22):225001, 2017. doi: 10.1103/PhysRevLett.118.225001.

[147] J. C. Slater. A simplification of the hartree-fock method. *Phys. Rev.*, 81:385–390, Feb 1951. doi: 10.1103/PhysRev.81.385. URL https://link.aps.org/doi/10.1103/PhysRev.81.385.

[148] M. W. C. Dharma-wardana, D. D. Klug, and R. C. Remsing. Liquid-liquid phase transitions in silicon. *Phys. Rev. Lett.*, 125:075702, Aug 2020. doi: 10.1103/PhysRevLett.125.075702. URL https://link.aps.org/doi/10.1103/PhysRevLett.125.075702.

[149] M. Gajdoš, K. Hummer, G. Kresse, J. Furthmüller, and F. Bechstedt. Linear optical properties in the projector-augmented wave methodology. *Physical Review B*, 73(4): 045112, 2006.

[150] J. P. Perdew, K. Burke, and M. Ernzerhof. Generalized gradient approximation made simple. *Physical review letters*, 77(18):3865, 1996.

[151] A. Jain, S. P. Ong, G. Hautier, W. Chen, W. D. Richards, S. Dacek, S. Cholia, D. Gunter, D. Skinner, G. Ceder, et al. Commentary: The materials project: A materials genome approach to accelerating materials innovation. *APL materials*, 1(1):011002, 2013.

[152] J. Hafner. Ab-initio simulations of materials using vasp: Density-functional theory and beyond. *Journal of computational chemistry*, 29(13):2044–2078, 2008.

[153] P. E. Blöchl. Projector augmented-wave method. *Physical review B*, 50(24):17953, 1994.

[154] F. D. Murnaghan. The compressibility of media under extreme pressures. *Proceedings of the National Academy of Sciences*, 30(9):244–247, 1944.

[155] P. Drude. Zur elektronentheorie der metalle. *Annalen der Physik*, 1,3:556,369, 1900.

[156] J. I. Mustafa, M. Bernardi, J. B. Neaton, and S. G. Louie. Ab initio electronic relaxation times and transport in noble metals. *Physical Review B*, 94(15):155105, 2016.

[157] F. Ladstädter, U. Hohenester, P. Puschnig, and C. Ambrosch-Draxl. First-principles calculation of hot-electron scattering in metals. *Phys. Rev. B*, 70(23):235125, 2004. ISSN 1098-0121. doi: 10.1103/physrevb.70.235125.

[158] P. Kratzer and M. Zahedifar. Relaxation of electrons in quantum-confined states in pb/si(111) thin films from master equation with first-principles-derived rates. *New J. Phys.*, 21:123023, 2019. doi: 10.1088/1367-2630/ab5c76.

[159] H. Kramers. Some remarks on the theory of absorption and refraction of x-rays. *Nature*, 117(2952):774–775, 1926. doi: 10.1038/117774a0.

[160] R. d. L. Kronig. On the theory of dispersion of x-rays. *J. Opt. Soc. Am.*, 12(6):547–557, 1926. doi: 10.1364/JOSA.12.000547.

[161] P. Giannozzi, S. Baroni, N. Bonini, M. Calandra, R. Car, C. Cavazzoni, D. Ceresoli, G. L. Chiarotti, M. Cococcioni, I. Dabo, et al. Quantum espresso: a modular and open-source software project for quantum simulations of materials. *Journal of physics: Condensed matter*, 21(39):395502, 2009.

[162] P. Giannozzi, O. Andreussi, T. Brumme, O. Bunau, M. B. Nardelli, M. Calandra, R. Car, C. Cavazzoni, D. Ceresoli, M. Cococcioni, et al. Advanced capabilities for materials modelling with quantum espresso. *Journal of physics: Condensed matter*, 29(46):465901, 2017.

[163] A. A. Mostofi, J. R. Yates, G. Pizzi, Y.-S. Lee, I. Souza, D. Vanderbilt, and N. Marzari. An updated version of wannier90: A tool for obtaining maximally-localised wannier functions. *Computer Physics Communications*, 185(8):2309–2310, 2014.

[164] S. Baroni, S. De Gironcoli, A. Dal Corso, and P. Giannozzi. Phonons and related crystal properties from density-functional perturbation theory. *Reviews of modern Physics*, 73(2): 515, 2001.

[165] J.-J. Zhou, J. Park, I.-T. Lu, I. Maliyov, X. Tong, and M. Bernardi. Perturbo: A software package for ab initio electron–phonon interactions, charge transport and ultrafast dynamics. *Computer Physics Communications*, 264:107970, 2021.

APPENDIX A. EXPLORATIONS OF NEW METHODS FOR CALCULATING COLLISION RATES

This Appendix describes investigations of new first-principles methods for analyzing electron-electron and electron-phonon collisions. This was performed under a mid-year SAA contract placed under this LDRD.

A.1. Overview

In what follows, we study the ground state electronic structure, temperature-dependent optical response, and electronic relaxation mechanisms of beryllium. These studies are conducted with a variety of tools from first principles multi-atom electronic structure theory. Our interest in beryllium is motivated by both its use in experiments at the Sandia Z facility as well as its low Z ($Z_{nuc} = 4$). This allows us to efficiently study a system that has both a relatively shallow K-shell and nearly-free electrons near the chemical potential at solid densities, while minimizing concerns about errors due to pseudization of the core orbitals. Thus it is of practical interest and a useful starting point for explorations of new computational methods.

A.2. Convergence analysis for the ground state electronic structure

In our study of crystalline beryllium (Be), we perform first-principles density functional theory (DFT) [29, 30] using the *Vienna Ab-Initio Simulation Package* (VASP) [39, 41, 149]. The starting point for these calculations is capturing the crystal structure of solid Be and we do so using a 2-atom primitive unit cell from Materials Project [151] and perform convergence tests to determine the density of the **k**-point grid used in representing the first Brillouin zone and energy cutoff of the plane-wave basis set [153] that suffices to accurately represent the ground state electronic structure. To assess the impact of approximations used in the modeling of the electron-electron interaction we use both the LDA [30] and PBE [150] exchange-correlation functionals. From our convergence tests, we conclude that **k**-point grids more dense than $15 \times 15 \times 15$ and energy cutoff values greater than 600 eV lead to well-converged total energies per atom of -3.77 eV/atom and -4.20 eV/atom for the PBE and LDA exchange-correlation functionals respectively. These convergence results, along with accounting for computational expense, lead us to use a $15 \times 15 \times 15$ **k**-point grid and 800 eV cutoff energy for both LDA and PBE self-consistent calculations. Using the Murnaghan equation of state [154], the a_o and c_o lattice constants for Be were found to be 2.231 and 3.525 Å respectively for the LDA exchange-correlation functional. The same method was used for the PBE functional, which leads to lattice constants of 2.264 and 3.574 Å.

The subsequent electronic structure calculations were performed using the converged charge density and calculated lattice constants found for the given exchange-correlation functional. We explore the ground state electronic structure of Be by computing the electronic band structure along high-symmetry points along with the electronic density of states as shown in fig. A-1. We

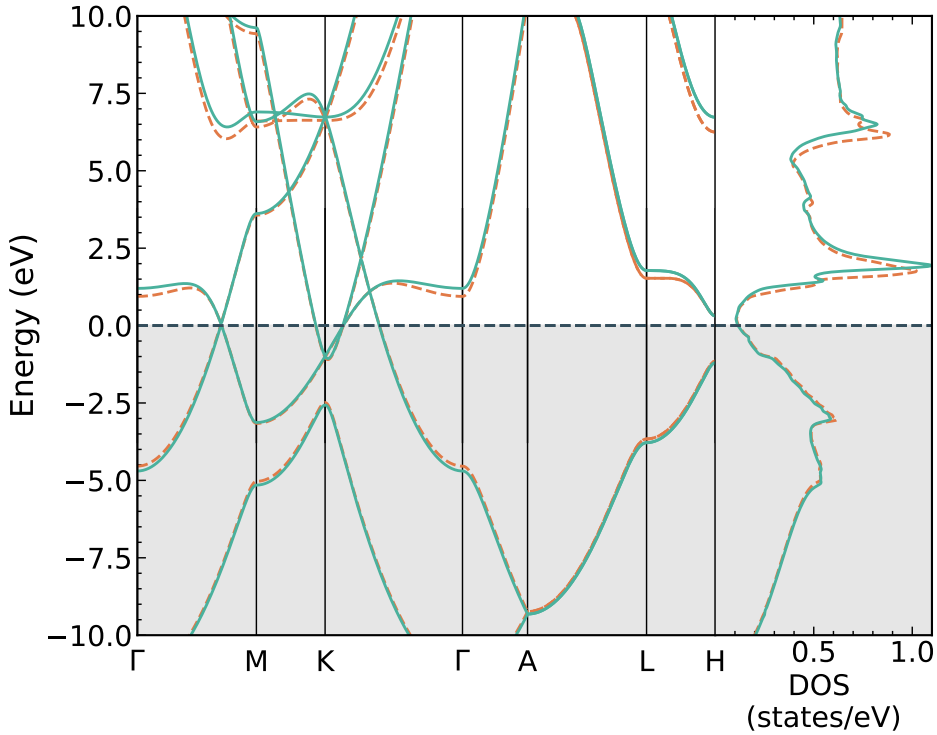

Figure A-1 Electronic band structure and DOS calculated with LDA (solid) and PBE (dashed) exchange-correlation functionals. The energy zero is set to the Fermi energy.

conclude from this figure that within the 20 eV energy range from −10 to 10 eV, the electronic structure predicted by LDA and PBE agree very well. One of our primary goals is to benchmark our results against an average atom (DFT-AA) model that uses LDA, and we will use LDA in all subsequent DFT-MD calculations.

A.3. Temperature-dependent optical response

After studying the ground state electronic structure of our system, we turned our attention to the optical properties of our model of Be and calculated the imaginary part of its macroscopic dielectric function. This is proportional to the optical absorption spectrum and is closely related to the optical conductivity, both of which can also be studied using DFT-AA techniques. Because we are ultimately interested in studying warm dense Be, we model thermalized electrons by using Fermi smearing in VASP to set electron temperatures of 0.5, 1.0, and 3.0 eV. These calculations were done with 64 total bands, 4 valence and 60 conduction, on a $43 \times 43 \times 43$ **k**-point grid with an energy cutoff of 800 eV; the charge density was taken from the converged self-consistent calculation.

Fig. A-2a shows the computed results for the temperature-dependent optical response function. In this figure we see three different photon energy ranges of interest: 0 to 6.5, 6.5 to 9.5, and 9.5 to 10.0 eV. In the lowest energy range, we observe that the strength of optical transitions is strongly

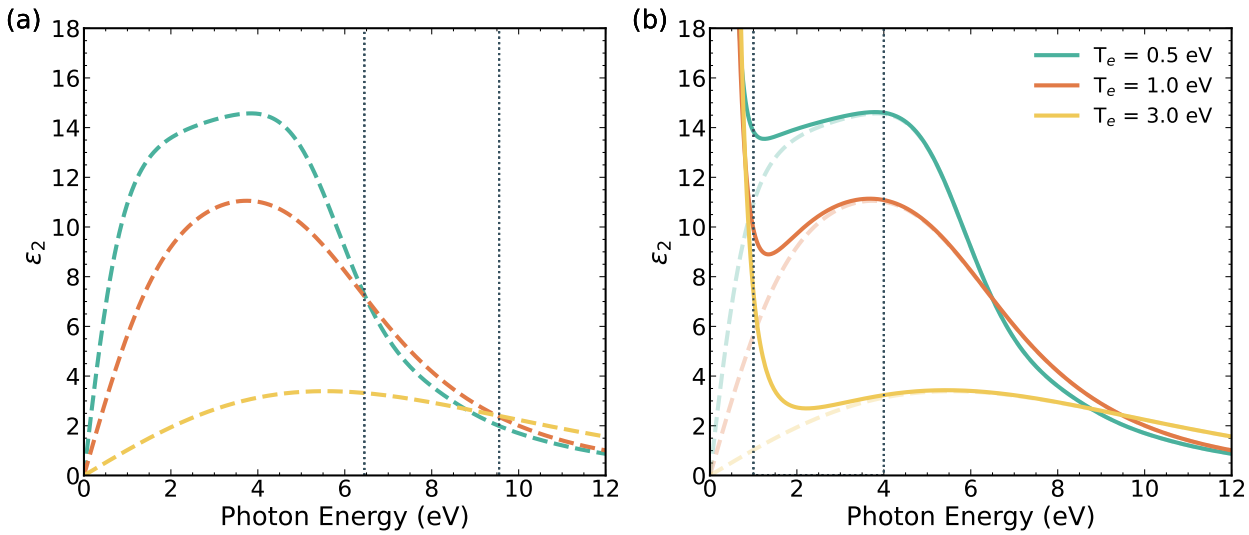

Figure A-2 (a) Imaginary part of the macroscopic dielectric function at temperatures of 0.5, 1.0, and 3.0 eV. (b) Imaginary part of the macroscopic dielectric function including the Drude term at temperatures of 0.5, 1.0, and 3.0 eV.

dependent on the temperature of the system. However, for photon energies above 6.5 eV, this is no longer the case. Between photon energies of 6.5 and 9.5 eV, the moderate-temperature (1.0 eV) optical spectrum becomes dominant, and between photon energies of 9.5 to 10.00 eV, the high temperature (3.0 eV) curve has the strongest transitions. The behavior in the first region is due to the fact that as temperature increases, there is less occupation of valence bands and more occupation of conduction bands near the Fermi level, thus leading to a lower transition probability. Transitions at higher photon energies become more likely at higher temperature since the Fermi smearing leads to more partially occupied initial states that allow the transitions at those energies. Although these optical spectra adequately describe the optical properties of warm dense Be at energies $\gtrsim 2$ eV, they do not show the full picture for lower energies. Since Be is metallic, various bands cross the Fermi energy and thus intraband transitions can occur and must be included in the optical properties of Be — this was not accounted for in the optical spectra in fig. A-2a.

We included intraband transitions by utilizing the Drude model of electrical conduction [155], where the intraband transitions depend on the electron relaxation time. We used a relaxation time of 10 fs as an input parameter in our VASP calculations. Since there was no experimentally determined relaxation time available for Be, our choice of 10 fs was based on values found from a first-principles study of metallic relaxation times within the Drude model [156]. Fig. A-2b compares the optical spectra as a function of electron temperature with and without intraband transitions included. At low photon energies, below ~ 1 eV, the intraband transitions dominate the optical response independent of temperature. This result is expected due to the large number of transitions within bands that require only a small quantity of energy. As photon energy increases from 1 to 4 eV, the curves with intraband transitions still dominate. However, there are not as many available intraband transitions in this energy range, so the Drude term has a much more modest effect on the optical spectra in this regime. Finally, when photon energies exceed 4

eV, intraband transitions become negligible and the spectra with and without these intraband transitions coincide.

As shown in Eq. (11) , the imaginary part of the dielectric function can be used to calculate optical conductivity. Fig. A-3 shows a comparison between the optical conductivity calculated using DFT-AA and DFT-MD methods for three different electron temperatures, where we see good agreement between the two methods at nonzero frequency values. The disagreement at very low frequency may be explained by the difficulty to converge the **k**-point grid in DFT-MD for low frequency dielectric function values.

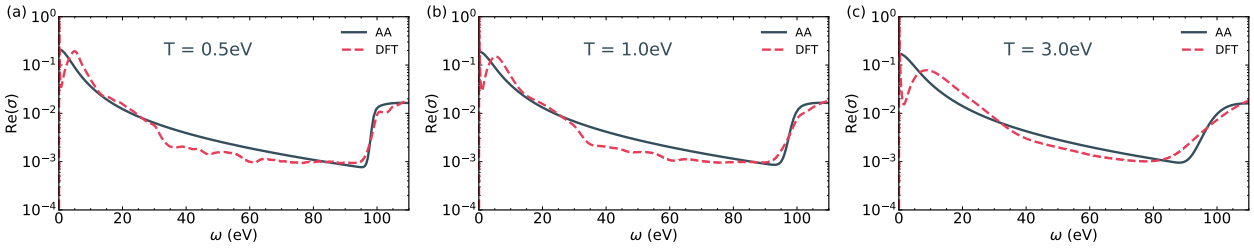

Figure A-3 A comparison of the real part of the optical conductivity between DFT-AA (solid lines) and DFT-MD (dashed lines) for different electron temperatures (a) 0.5, (b) 1.0, and (c) 3.0 eV.

Our study of the optical properties of warm crystalline Be demonstrates the temperature dependence of the optical spectra at visible and UV photon energies and the importance of properly modeling the optical transitions in metals by including the relaxation time to account for intraband transitions that occur at low photon energies. However, the Drude model of intraband transitions is a highly simplified picture relying on a single, constant relaxation time for all electrons. In reality, relaxation times will depend on excitation energy, temperature, and/or the extent to which the material is in thermodynamic equilibrium. Furthermore, the relative importance of electron-electron and electron-ion relaxation mechanisms in warm dense matter is not well understood. We investigate these questions in the following sections.

A.4. First-principles calculations of electron-electron collisions

The above study of the optical properties of warm crystalline Be gives some insight into how Be responds to photons with different energies, but it invokes a limited description of electron relaxation and it does not offer much insight into what happens to the electrons after excitation. We obtain a better understanding of how excited electrons behave by investigating electron scattering; specifically, we independently study electron-electron (e-e) and electron-phonon (e-ph) interactions. We focus on e-e interactions in this section and describe our work on e-ph interactions in section A.5.

Our first-principles approach for computing e-e scattering lifetimes follows a framework developed by Kratzer and Zahedifar [158] that we recently applied to a similar study of e-e

lifetimes in ambient aluminum [23]. The scattering rate is taken to be proportional to the imaginary part of the electronic self-energy:

$$\Gamma_{n\mathbf{k}} = -2\,\mathrm{Im}\left\{\Sigma(\varepsilon_{n\mathbf{k}})\right\}/\hbar,$$

where $\Gamma_{n\mathbf{k}}$ is the e-e scattering rate, Σ is the self-energy, and $\varepsilon_{n\mathbf{k}}$ is the quasiparticle energy for the state $n\mathbf{k}$ [158]. While $\Sigma(\varepsilon_{n\mathbf{k}})$ and corresponding $\Gamma_{n\mathbf{k}}$ can be obtained from a computationally expensive *GW* calculation [157], here we apply a more efficient method that computes $\Sigma(\varepsilon_{n\mathbf{k}})$ from a G_0W_0 calculation. The G_0W_0 calculation involves a complex shift η in the Kramers-Kronig transformation [159, 160], and we find that an unusually small value of η is needed to accurately resolve the the self-energy near the Fermi energy (see inset of fig. A-4). Fig. A-4 further demonstrates $\mathbf{k}$-point grid convergence in our G_0W_0 calculations, and we use a $7\times7\times7$ $\mathbf{k}$-point grid and the smallest value of $\eta = 0.01$ eV for the ultimate e-e lifetime extraction.

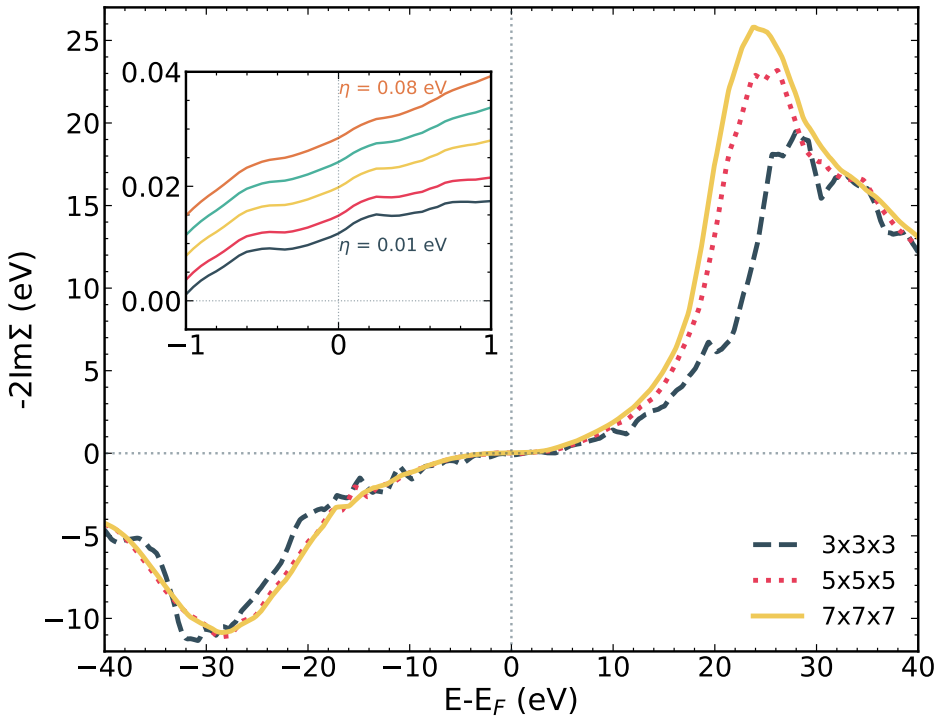

Figure A-4 The scaled imaginary part of the self-energy obtained from G_0W_0 calculations with increasingly dense k-point sampling. The inset shows the scaled imaginary self-energy near the Fermi energy for the $7\times7\times7$ k-point grid with different η values.

After obtaining adequately converged self-energies, we consider the scattering rate $-2\,\mathrm{Im}\left\{\Sigma(\varepsilon_{n\mathbf{k}})\right\}$ for the first conduction band at the Γ point over an energy range between 0 and 10 eV, and we fit this data to the form predicted by Landau's theory of the Fermi liquid: $\alpha(\varepsilon_{n\mathbf{k}} - E_F)^2$ [158]. This fit then predicts hot electron lifetimes as

$$\tau_{n\mathbf{k}} = \frac{37\text{ fs eV}^2}{(\varepsilon_{n\mathbf{k}} - E_F)^2}. \tag{37}$$

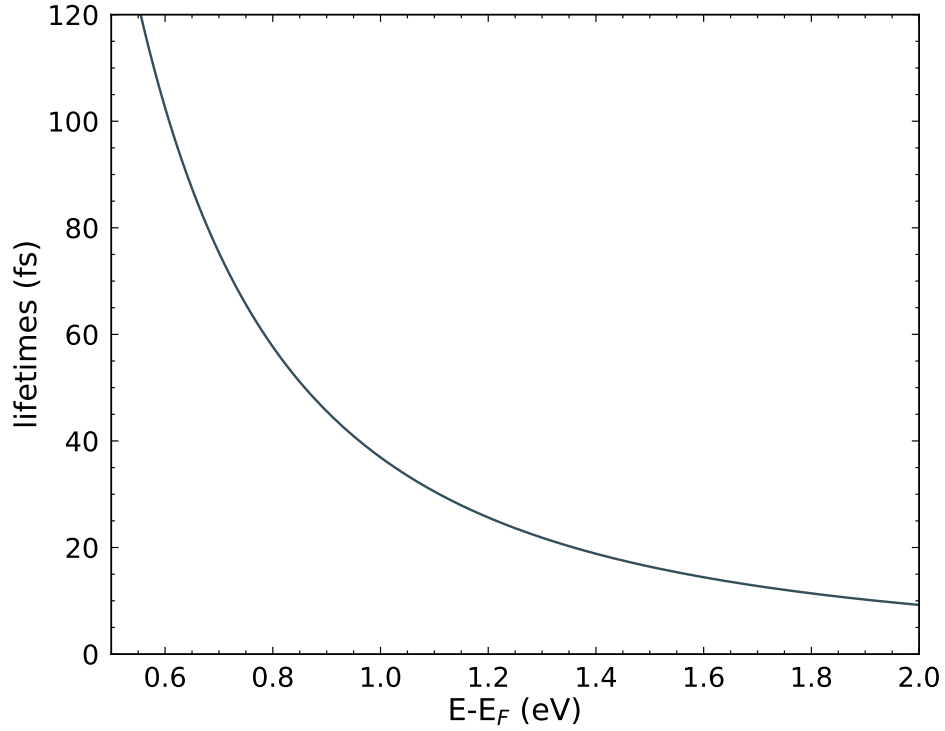

Figure A-5 The electron-electron lifetimes obtained from the fit to Landau's theory of the Fermi liquid for the first conduction band at the Γ k-point.

Fig. A-5 shows the energy-dependent behavior of the e-e lifetimes $\tau_{n\mathbf{k}}$ for crystalline Be. We see that excited electrons near the Fermi energy are long-lasting, with lifetimes on the order of a few hundred femtoseconds or more before scattering with another electron. Our calculations also predict that electrons further from the Fermi energy scatter at a much higher rates since the e-e lifetimes are on the order of a few tens of femtoseconds and diminish with increasing energy. This method for calculating e-e lifetimes is especially promising for highly excited systems because the computational cost compared to the traditional approach of performing a full *GW* calculation is greatly reduced. This increased computational efficiency will be key for studying e-e lifetimes at energies far from the Fermi energy in highly excited systems.

A.5. First-principles calculations of electron-phonon collisions

As discussed in the previous section, we explored the scattering processes from both e-e and e-ph interactions. We studied these two processes independently because as currently implemented, the methods used can only capture either e-e or e-ph scattering, not both. Our study of e-ph scattering, unlike e-e, was done by using the open-source software PERTURBO [165] to numerically solve the Boltzmann transport equation (BTE),

$$\frac{\partial f_{n\mathbf{k}}(\mathbf{r},t)}{\partial t} = -[\nabla_{\mathbf{r}} f_{n\mathbf{k}}(\mathbf{r},t)\cdot\mathbf{v}_{n\mathbf{k}} + \hbar^{-1}\nabla_{\mathbf{k}} f_{n\mathbf{k}}(\mathbf{r},t)\cdot\mathbf{F}] + I[f_{n\mathbf{k}}], \tag{38}$$

where $f_{n\mathbf{k}}$ are occupations of electronic orbitals indexed by n and $\mathbf{k}$, $\mathbf{v}_{n\mathbf{k}}$ are the band velocities, $\mathbf{F}$ is a drift term from external fields, and I is the collision integral currently containing only electron-phonon scattering processes. In PERTURBO version 1.0, simplifications are made to the BTE to reduce computational cost. First, $f_{n\mathbf{k}}$ are assumed to have no spatial dependence because the fields vary slowly and the material is homogeneous, simplifying the BTE to

$$\frac{\partial f_{n\mathbf{k}}(\mathbf{r},t)}{\partial t} = -[\hbar^{-1}\nabla_{\mathbf{k}} f_{n\mathbf{k}}(\mathbf{r},t)\cdot\mathbf{F}] + I[f_{n\mathbf{k}}]. \tag{39}$$

Also, the $\mathbf{F}$ term vanishes because it is assumed that there is no external field, further simplifying the BTE to

$$\frac{\partial f_{n\mathbf{k}}(\mathbf{r},t)}{\partial t} = I[f_{n\mathbf{k}}]. \tag{40}$$

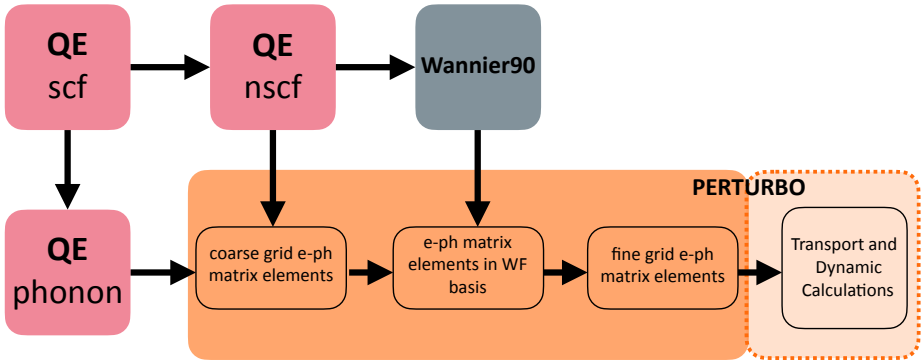

Figure A-6 A diagram of the workflow for simulating e-ph scattering using PERTURBO.

To perform e-ph carrier dynamics calculations in PERTURBO, we start from a first-principles DFT-MD calculation using Quantum Espresso [161, 162]. After $\mathbf{k}$-point and plane-wave energy cutoff converge tests, we performed a self-consistent calculation using a $20\times20\times20$ $\mathbf{k}$-point grid and an energy cutoff of 80 Ry to obtain the ground-state charge density. We then used this ground-state configuration as input for density functional perturbation theory (DFPT) [164] to perform a phonon calculation in Quantum Espresso. The same $20\times20\times20$ $\mathbf{k}$-point grid was used, while a coarser $4\times4\times4$ $\mathbf{q}$-point grid was used due to the high computational expense of DFPT calculations. The DFPT calculations provide e-ph matrix elements entering into the evaluation of $I[f_{n\mathbf{k}}]$. However, for accurate transport and dynamics calculations, PERTRUBO requires e-ph matrix elements from much denser $\mathbf{k}$ and $\mathbf{q}$-point grids which we obtain by utilizing Wannier interpolation using the Wannier90 code [163]. The outputs from our Quantum Espresso phonon calculation and the Kohn-Sham eigenvalues and wavefunctions calculated from a nonself-consistent (nscf) calculation using a $20\times20\times20$ $\mathbf{k}$-point grid were used to construct maximally localized Wannier Wavefunctions (WF). The KS wavefunctions were initially projected onto the s and p orbitals of Be, resulting in a a total of eight wannierized wavefunctions. The spread of the WFs was then minimized until the difference in WF spread from one step to the next was 1×10^{-9} or less for four consecutive iterations. Using the results from the DFT-MD and

DFPT calculations, PERTURBO calculates the e-ph matrix elements from the coarse $20 \times 20 \times 20$ **k** and $4 \times 4 \times 4$ **q**-point grids. These e-ph matrix elements and the rotation matrices from the Wannier90 calculation are then used to find the e-ph matrix elements in the real space WF basis; this is then interpolated to find the e-ph matrix elements on ultra-fine **k** and **q** grids. A diagram of this workflow is shown in fig. A-6.

PERTURBO allows the study of carrier dynamics by imposing an initial distribution for occupations of excited electron orbitals, such as a Gaussian, and then computing the relaxation dynamics by solving Eq. (41), where the right side represents the collision integral $I[f_{n\mathbf{k}}]$:

$$\frac{\partial f_{nk}(\mathbf{r},t)}{\partial t} = -\frac{2\pi}{\hbar}\frac{1}{N_{\mathbf{q}}}\sum_{m\mathbf{q}\nu}|g_{mn\nu}(\mathbf{k},\mathbf{q})|^2 \times [\delta(\varepsilon_{n\mathbf{k}} - \hbar\omega_{\nu\mathbf{q}} - \varepsilon_{m\mathbf{k}+\mathbf{q}}) \times F_{em} + \delta(\varepsilon_{n\mathbf{k}} + \hbar\omega_{\nu\mathbf{q}} - \varepsilon_{m\mathbf{k}+\mathbf{q}}) \times F_{abs}]. \tag{41}$$

Here, $N_{\mathbf{q}}$ is the number of **q**-points in the summation, $g_{mn\nu}(\mathbf{k},\mathbf{q})$ are the e-ph matrix elements, $\varepsilon_{n\mathbf{k}}$ is the electron quasiparticle energy for an electron at band n and **k**-point **k**, and $\hbar\omega_{\nu\mathbf{q}}$ is the energy of the phonon with mode ν and **q**-point **q**. F_{em} and F_{abs} describe phonon emission and absorption:

$$\begin{aligned} F_{em} &= f_{n\mathbf{k}}(1 - f_{m\mathbf{k}+\mathbf{q}})(N_{\nu\mathbf{q}} + 1) - f_{m\mathbf{k}+\mathbf{q}}(1 - f_{n\mathbf{k}})N_{\nu\mathbf{q}} \\ F_{abs} &= f_{n\mathbf{k}}(1 - f_{m\mathbf{k}+\mathbf{q}})N_{\nu\mathbf{q}} - f_{m\mathbf{k}+\mathbf{q}}(1 - f_{n\mathbf{k}})(N_{\nu\mathbf{q}} + 1), \end{aligned} \tag{42}$$

where f and $N_{\nu\mathbf{q}}$ are the electron and phonon occupations, respectively, and the phonon occupations are kept fixed throughout the simulation.

The dynamics simulations in PERTURBO were originally intended to be performed on cold semiconductors where the calculation for the electrons in the conduction bands and holes in the valence bands are performed separately. For electron dynamics simulations in semiconductors, the conduction bands included in the simulation are unoccupied besides the relaxing electrons from the excitation. These excited electrons then relax to the conduction band minimum since there are no empty states below that, and a similar principle applies to valence bands in hole dynamics simulations. An electron dynamics simulation for Be in PERTURBO would treat all the conduction bands included in the calculation as completely empty, which is incorrect, since as a metal Be has conduction bands crossing the Fermi energy with nonzero electron occupancy which would not be included in the PERTURBO simulation.

We address this problem by modifying the PERTURBO source code to include a new initial distribution option which we call the *Gaussian plus Fermi* distribution where we add a Fermi-Dirac distribution to the Gaussian excitation. The Fermi-Dirac distribution is constrained by setting the electron temperature of interest to determine the width of the Fermi function and the Fermi energy of the system, which can be found from the DFT-MD calculation done prior to the dynamics simulation. The addition of the Fermi-Dirac distribution to the Gaussian distribution for the initial occupations allows PERTURBO to solve the BTE and relax the excited electrons in a physically meaningful way. Since there is now a barrier that models where the conduction bands included in the calculation are already occupied, at zero temperature, electrons are no longer able to relax into states below the Fermi energy, thus properly modeling a metallic system.

We studied the electron dynamics from e-ph scattering in Be after we excited the system with a Gaussian pulse centered at 9.6 eV, about 0.5 eV above the Fermi energy, and a smearing

parameter of 40 meV, which is both the electron temperature and the Gaussian width. The energy range of our simulation was 8.6 to 10.2 eV and the two bands within this energy range were included in our calculation. The phonon and electron temperatures were set to 25.25 and 40 meV, respectively. We solved Eq. (41) numerically using the Euler method with a time step of 1 fs. We ran simulations using these input parameters with five different **k**-point grids: from $50 \times 50 \times 50$ up to $90 \times 90 \times 90$ to test **k**-point convergence. The calculated electron distributions as a function of energy and time shown in fig. A-7 do not show obvious differences among the **k**-point grids.

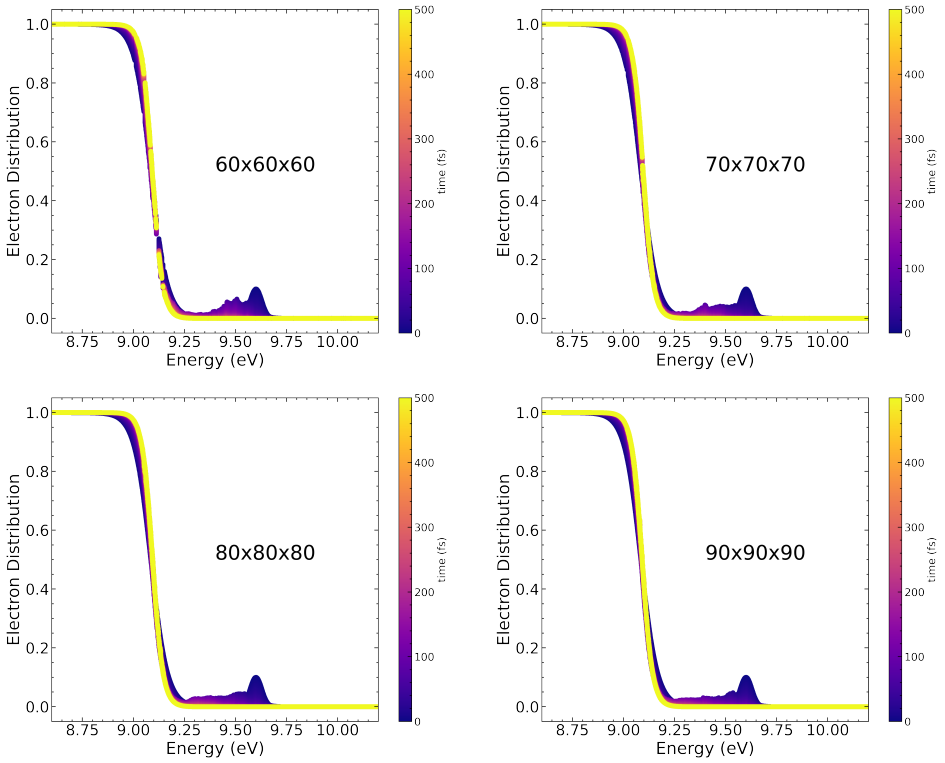

Figure A-7 The electron distribution as a function of time after an initial Gaussian excitation centered at 9.6 eV for different k-point grids as indicated.

To get more quantitative information about the **k**-point convergence of our simulations, we compared the results of each calculation to that of our calculation with the most dense grid. Since the energies sampled depend on the **k**-point grid, all of the electron distribution data was linearly interpolated so that the two sets of data can be compared as a function of energy and time. Fig. A-8 shows the relative difference between the linearly interpolated coarse *k*-point grid electron distribution and the $90 \times 90 \times 90$ interpolated electron distribution. We see that as the **k**-point grids become more dense, the relative differences approach zero. Although our $90 \times 90 \times 90$ calculation is not completely converged, we are satisfied with this grid due to the trade-off between simulation accuracy and the computational cost of denser **k**-point grids.

The selection of **k**-point grid, along with the time-evolution algorithm and time step, impacts the stability of the simulation over time. Ideally, the carrier concentration remains constant throughout the PERTURBO simulation. We can compute the carrier concentration by integrating

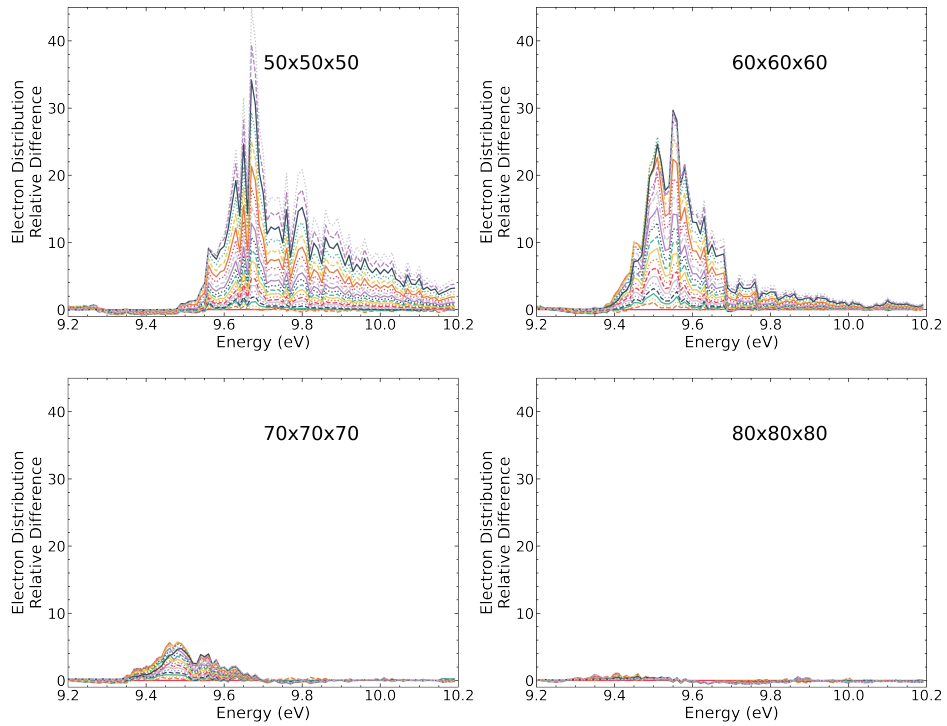

Figure A-8 The relative difference between four coarser k-point grids and the most dense 90×90×90 k-point grid. The relative difference was calculated for every 25 fs time step.

the carrier population,

$$\bar{f}(E,t) = \sum_{n\mathbf{k}} f_{n\mathbf{k}}(t)\delta(\varepsilon_{n\mathbf{k}} - E), \tag{43}$$

over energy. From our results reported in Table A-1, where we report the ratio between the smallest and largest carrier concentrations found during the 500 fs simulation, we find that our choice of integrator and time step results in a stable simulation since the values are near one. We also see that as the **k**-point grid becomes more dense, the carrier concentration gets closer to becoming a constant.

Table A-1 The ratio between the smallest and largest carrier concentrations found over the 500 fs simulation time for different k-point grids.

k-point grid	ratio
50×50×50	0.99947
60×60×60	0.99971
70×70×70	0.99985
80×80×80	0.99992
90×90×90	0.99995

Our **k**-point grid selection of $90 \times 90 \times 90$ has shown convergence and that it produces a stable simulation. Our goal is to use the data from these electron dynamics calculations to determine

values of interest such as the relaxation time after an excitation, and ongoing work continues in this direction.

A.6. Summary

We have presented a variety of first-principles calculations representative of capabilities that were being pursued under this LDRD. We first considered conventional electronic structure and optical response calculations, which are necessary precursors to the later calculations, but not new capabilities for our group. We then showed preliminary work establishing a capability within our group for explicitly capturing both electron-electron and electron-phonon relaxation mechanisms at a multi-atom first-principles level of theory. Our results are encouraging and we will continue to integrate PERTURBO calculations in work beyond this LDRD.

DISTRIBUTION

Hardcopy—Internal

Number of Copies	Name	Org.	Mailstop
1	Person	01xxx	xxxx

Email—Internal (encrypt for OUO)

Name	Org.	Sandia Email Address
Technical Library	01177	libref@sandia.gov

Sandia National Laboratories

Sandia National Laboratories is a multimission laboratory managed and operated by National Technology & Engineering Solutions of Sandia LLC, a wholly owned subsidiary of Honeywell International Inc., for the U.S. Department of Energy's National Nuclear Security Administration under contract DE-NA0003525.